University of Southampton

FACULTY OF ENGINEERING, SCIENCE AND MATHEMATICS

INSTITUTE OF SOUND AND VIBRATION RESEARCH

PERIODIC ORBIT ANALYSIS OF THE HELMHOLTZ EQUATION IN TWO-DIMENSIONAL ENCLOSURES

by

Christopher Ham

A thesis submitted in partial fulfillment for the

degree of Doctor of Philosophy

September 2008

UNIVERSITY OF SOUTHAMPTON

ABSTRACT

FACULTY OF ENGINEERING, SCIENCE AND MATHEMATICS

INSTITUTE OF SOUND AND VIBRATION RESEARCH

Doctor of Philosophy

PERIODIC ORBIT ANALYSIS OF THE HELMHOLTZ EQUATION IN TWO-DIMENSIONAL ENCLOSURES

by Christopher John Ham

This thesis examines how periodic orbits may be used in acoustics to understand solutions of the Helmholtz equation.

A review of the links between ray and wave mechanics is given including WKBJ (Wentzel, Kramers, Brillouin and Jeffreys) and EBK (Einstein, Brillouin, Keller) methods. It is also noted that some mode shapes in chaotic enclosures are scarred by the short periodic orbits. This motivates the proposal of the Mode Scar Hypothesis and the Mode Resonance Function Hypothesis.

The trace formula, which is a sum over periodic orbits, approximates the level density for an acoustic enclosure. The trace formula in the concentric annulus domain is derived using a formulation for enclosures with continuous symmetry by Creagh and Littlejohn [1]. Results for the variance of the difference between the true and average mode counts are obtained.

A technique called short periodic orbit theory (SPOT) for the approximation of mode shapes devised by Babič and Buldyrev [2] and Vergini [3] is given. SPOT is extended to impedance boundary conditions. SPOT is implemented in the quarter stadium, quadrupole, circle and eccentric annulus enclosures with Dirichlet, Neumann and impedance boundary conditions. Concave enclosures with Dirichlet or Neumann boundary conditions were best approximated using SPOT.

A design loop for enclosures is proposed using the periodic orbit ideas given. A model problem is used to provide insight into the effectiveness of these methods. It was found that it was not possible to breakdown all mode shapes in the eccentric annulus into contributions from short periodic orbits.

Contents

List of Figures

Declaration of authorship

I, Christopher Ham, declare that this thesis entitled “Periodic orbit analysis of the Helmholtz equation in two-dimensional enclosures” and the work presented in thesis are both my own, and have been generated by me as the result of my own research. I confirm that:

- this work was done wholly or mainly while in candidature for a research degree at this University; where any part of this thesis has been previously submitted for a degree or any other qualification at this University or any other institution, this has been clearly stated;
- where I have consulted the published work of others, this is always clearly attributed;
- where I have quoted from the work of others, the source is always given. With the exception of such quotations, this thesis is entirely my own work;
- I have acknowledged all main sources of help;
- where the thesis is based on myself jointly with others, I have made clear what was done by others and what I have done myself;
- parts of this work have been published as: M C M Wright and C J Ham “Periodic orbit theory in acoustics: spectral fluctuations in circular and annular wave guides” *Journal of the Acoustical Society of America* 121 (4) 2007

Signed: Date:

Acknowledgements

I would like to thank my supervisor, Dr Wright, for his help throughout this project and for giving me the opportunity in the first place. I would also like to thank my second supervisor, Prof Mace, for his support and useful comments. I would like to thank Dr Howls for his help and interest as part of my review panel. I would also like to acknowledge Dr Vergini for many useful conversations and insights into this area. I would also like to thank him and his wife for their kind hospitality in Buenos Aires.

I would like to thank my parents for their support, understanding and forbearance over the last years. This would not have been possible without you. I would also like to thank Richard, my brother, Liz, his wife and Marcus and James, my nephews. They have been very supportive and helped me keep things in perspective.

I would like to acknowledge the support of a Rayleigh scholarship from the ISVR.

Finally, I would like to thank everyone at Southampton who made my time here so enjoyable. I have shared an office with many people and I like to thank them all. We have had many good conversations, some about work, while having a cup of tea and a slice of cake. I would also like to thank the Southampton University Concert Band for providing me with a life beyond my thesis.

Chapter 1

Introduction

1.1 General aims

The aim of this thesis is to show that ray dynamics, and in particular periodic orbits, can provide an insight into mode shapes and mode wavenumbers in acoustic enclosures.

Periodic orbits in an enclosure are ray paths that return to their starting position with the same direction of motion. Periodic orbits have been used as a tool in the analysis of dynamical systems since Poincaré (1892) [4]. Poincaré was interested in celestial mechanics, where periodic orbits are the planetary orbits. Periodic orbits are still an important part of the analysis of nonlinear systems [5]. However, in more recent times, periodic orbits have been used for the analysis of billiard problems in quantum chaology and it is this which is of interest here. It should be noted that periodic orbits are of current relevance in physics, some very recent publications include [6–9].

The definition of an enclosure and the relevance to acoustics will be given in section 1.2. Periodic orbits have been used extensively to study similar problems in quantum mechanics. In section 1.3 the fundamental equations of quantum mechanics are given and the link to acoustics is made. The rest of this chapter gives a brief

review of the main ways in which periodic orbits have been applied in quantum mechanics. In section 1.8 the Mode Resonance Function and Mode Scar Hypotheses are proposed. An overview of the rest of the work in the thesis is given in section 1.9 and finally, a summary of original contributions is set out in section 1.10.

1.2 Helmholtz equation and enclosures

In linear acoustics many problems can be reduced to finding the modes of the Helmholtz equation

$$(\nabla^2 + k_n^2)\Psi_n(\mathbf{x}) = 0, \tag{1.1}$$

where k_n is the wavenumber of the mode and $\Psi_n(\mathbf{x})$ is the mode shape function in a closed domain $\mathscr{D}$. The boundary conditions may be for example Dirichlet, $\Psi_n(\mathbf{x})|_{\partial\mathscr{D}} = 0$ or Neumann, $\partial\Psi_n(\mathbf{x})/\partial n|_{\partial\mathscr{D}} = 0$, where n denotes the normal to the boundary $\partial\mathscr{D}$.

The solutions of the above problem form a spectrum of mode wavenumbers so that $k_0 \leq k_1 \leq k_2 \ldots$. Each mode has a well defined mode shape $\Psi_n(\mathbf{x})$. There may be finitely many degeneracies at a given mode wavenumber.

The domain $\mathscr{D}$ will be called the enclosure, which could be a drum or a duct cross-section in acoustics. In other areas of physics such as optics the enclosure could be an optical fibre cross-section for example.

Analytic solutions to the Helmholtz equation exist for a relatively small family of domains; normally where there is a coordinate system available which allows separation of variables. Otherwise, the system must be solved using a numerical technique such as the finite element method (FEM), or the boundary element method (BEM). Unfortunately, as frequency increases the size of the numerical problem increases very quickly and so high frequency problems can be very numerically expensive to solve. There are numerical methods that are more suited to high frequency problems such as Vergini and Saraceno [10] and Barnett [11], but these methods are limited by

the shape of domain and the boundary conditions for which they can used.

1.3 Quantum chaology

Quantum chaology [4, 12, 13] is the study of how chaos in classical mechanics arises in the limit of quantum mechanics, which is essentially a linear wave theory. A model often used to explore quantum chaology is the quantum billiard. This is a notional frictionless billiard table with no pockets on which a single billiard ball is allowed to bounce without losing energy. Classically this situation is understood: the billiard ball moves in a straight line until it bounces off a cushion where the angle of incidence equals the angle of reflection.

In quantum mechanics this problem is formulated differently. The billiard ball must stay on the billiard table, so it is treated as being confined in an infinite potential well. The billiard ball does not have a definite position but it has a probability distribution. The time-dependent Schrödinger equation is required to solve this problem [4]

$$\mathrm{i}\bar{h}\frac{\partial\Psi(\mathbf{x},t)}{\partial t} = \frac{-\bar{h}^2}{2m}\nabla^2\Psi(\mathbf{x},t) + V(\mathbf{x},t)\Psi(\mathbf{x},t), \tag{1.2}$$

where $\Psi(\mathbf{x},t)$ is the wave function, $\bar{h}$ is the reduced Planck constant, m is the mass of the billiard ball and $V(\mathbf{x},t)$ is the potential confining the billiard ball. The probability of the billiard ball being found in a region Ω at time t is $\int_\Omega |\Psi(\mathbf{x},t)|^2 \mathrm{d}\mathbf{x}$.

The potential $V(\mathbf{x})$ is constant in time if a billiard table is being considered. This means that the time variable can be separated out so $\Psi(\mathbf{x},t) = \psi(\mathbf{x})\mathrm{e}^{-\mathrm{i}\omega t}$. This gives the time-independent Schrödinger equation [4]

$$\frac{-\bar{h}^2}{2m}\nabla^2\psi(\mathbf{x}) + V(\mathbf{x})\psi(\mathbf{x}) = E\,\psi(\mathbf{x}), \tag{1.3}$$

where E is the energy of the billiard ball. The potential function $V(\mathbf{x})$ is zero in the billiard domain and infinite outside the billiard domain. Inside the billiard domain

the time-independent Schrödinger equation reduces to

$$\nabla^2\psi(\mathbf{x}) = \frac{-2mE}{\hbar^2}\psi(\mathbf{x}), \tag{1.4}$$

which is the Helmholtz equation, where $k = \sqrt{2mE}/\hbar$. Techniques developed in quantum mechanics to understand quantum billiards can therefore also be used in acoustics to understand modes in enclosures.

1.4 Semiclassical limit

The quantum mechanical limit $\hbar/S \to 0$ is called the semiclassical limit, where S is the typical action of the system. In quantum chaology understanding the semiclassical limit has been of particular interest. Often this limit is written as $\hbar \to 0$, despite $\hbar$ being a physical constant. In acoustics, the semiclassical limit corresponds to the high frequency limit such that $\lambda/L \to 0$, where λ is the typical wavelength of sound and L is the typical length scale of the enclosure. The semiclassical limit is of particular interest because it is a singular limit. This means that most semiclassical expansions are singular perturbations.

An area of interest in quantum chaology is understanding how quantum mechanics can be approximated using only information from the classical description. In acoustics this corresponds to understanding the modes in terms of the ray dynamics in the enclosure. In turn this may provide a link between the geometry of the enclosure and the mode shapes in that enclosure.

1.5 WKBJ and EBK approximations

The use of high frequency approximations for the Helmholtz equation is not new. The wave function in the Wentzel, Kramers, Brillouin and Jeffreys (WKBJ) approx-

imation is given by [14]

$$\psi(\mathbf{x}) = A(\mathbf{x};k)\exp(\mathrm{i}ku(\mathbf{x})). \tag{1.5}$$

It can be used as the mathematical basis for the ray approximation of waves at high frequency. The WKBJ was used by Keller [15, 16] as part as basis of the Einstein, Brillouin, Keller method (EBK) method for the quantization of integrable domains. This method was used very effectively for approximating the mode wavenumbers for the circular enclosure [15].

1.6 Semiclassical trace formulae

There are a number of areas where mode shapes or the statistics of the mode wavenumbers have been connected to the periodic orbits. The first of these to be investigated were the semiclassical trace formulae.

The periodic orbits can be explicitly used to approximate some of the statistics of the mode wavenumbers. These statistics should be defined first. The level density is defined as [17]

$$\rho(k) = \sum_n \delta(k-k_n) = \overline{\rho}(k) + \rho_{\mathrm{osc}}(k), \tag{1.6}$$

where $\delta(x)$ is the Dirac delta function and k_n are the mode wavenumbers. The level density can be expressed as the sum of a smoothly increasing part $\overline{\rho}(k)$ and an oscillating part $\rho_{\mathrm{osc}}(k)$ [17]. The smooth part of the level density for a two-dimensional enclosure with smooth boundaries is given by the Weyl formula [17]

$$\overline{\rho}(k) \approx \frac{S}{2\pi}k \mp \frac{\partial S}{4\pi}, \tag{1.7}$$

where S is the area of the enclosure and ∂S is the length of its boundary. The minus sign is for Dirichlet boundary conditions and the plus sign for Neumann boundary

conditions. The symbol $\approx$ has been used here and later to indicate that a properly derived expansion has been given for the quantity, but it has been truncated so that it is accurate up to the order of the neglected term. Further terms of order k^{-1} and beyond can be added to equation (1.7) for enclosures with corners.

The mode count is defined as [18]

$$N(k) = \sum_n \Theta(k - k_n) = \int_0^k \rho(k')\,\mathrm{d}k' = \overline{N}(k) + N_{\mathrm{osc}}(k), \tag{1.8}$$

where $\Theta(x)$ is the Heaviside function. Again, the mode count can be expressed as the sum of a smoothly increasing part $\overline{N}(k)$ and an oscillating part $N_{\mathrm{osc}}(k)$ [18]. The average number of modes below a given wavenumber k can thus be easily calculated. It should be noted that the mean and oscillating parts of spectral functions such as $\overline{N}(k)$, $N_{\mathrm{osc}}(k)$, $\overline{\rho}(k)$ and $\rho_{\mathrm{osc}}(k)$ are not generally exact, terminating or converging.

Trace formulae use a formal sum over periodic orbits to give a semiclassical approximation to the level density. A trace formula for chaotic systems was derived by Gutzwiller [4] using the semiclassical propagator which arises naturally in quantum mechanics. Unfortunately, this trace formula is little practical use because it requires a very large number of periodic orbits to produce a useful approximation. The periodic orbits in a chaotic domain are difficult to catalogue. In fact, the number of periodic orbits required increases exponentially with the accuracy required.

Balian and Bloch [19] and Berry and Tabor [20] derived the trace formulae for integrable systems. Berry and Tabor [20] proved that it is always possible to derive a trace formula for an integrable enclosure of the form

$$\rho(k) \approx \overline{\rho}(k) + \sum_{po} \mathscr{A}_{po}(k) \cos(L_{po}k - \sigma_{po}\pi/2), \tag{1.9}$$

where $\mathscr{A}_{po}$ is an amplitude term for each periodic orbit, L_{po} is the length of the periodic orbit and σ_{po} is the Maslov phase, which counts reflections against the boundaries.

It is feasible to calculate the trace formula for integrable systems because all of the periodic orbits can be catalogued and analytic expressions for the lengths of the orbits can be found. This allows the formula to be written in a way that allows it to be computed.

Fundamentally, trace formulae are limited even if all the relevant orbits can be found because they generally diverge and even the most commonly used versions are only accurate to $O(\bar{h}) = O(1/k)$.

1.7 Mode shapes and scars

The periodic orbits have also been linked to the mode shapes, $\Psi_n(\mathbf{x})$. Periodic orbits could provide a connection between the mode shapes and the geometry of the enclosure. As previously stated the mode shapes in integrable domains can be found analytically, but if the domain is not integrable the problem requires numerical techniques. Numerical techniques such as the finite element method (FEM) allow mode shapes to be calculated in many circumstances. However, at high frequency the numerical techniques become expensive. This problem can be solved to some degree by using more powerful computers or writing more efficient algorithms but fundamentally the problem persists.

Importantly, numerical techniques give no understanding of why a mode shape looks the way it does. While this fundamental understanding is worthwhile in itself, it could also help explain how quantum mechanics is related to classical mechanics or how to design acoustic enclosures.

Shnirelman [21] and Berry [22, 23] considered the appearance of modes shapes in enclosures with chaotic ray dynamics. It was argued that since the rays in a chaotic enclosure travel in a seemingly random pattern the high frequency mode shapes should be well approximated by a superposition of plane waves travelling in random directions with random phase, but the same wavenumber. Plane waves

of the form $a_n \cos(\mathbf{k}_n.\mathbf{r} + \xi_n)$ are used, where each wave has a random direction $\mathbf{k}_n$, a random phase ξ_n and the amplitude a_n which can be random or held constant. Figure 1.1a shows the superposition of 100 random plane waves with constant wavenumber, $k = 50$, uniformly probable direction and phase, but constant amplitude. Figure 1.1a is one unit wide by one unit high.

Figure 1.1a does not look completely random. Clear ridges can be seen which are called "scarlets" by Heller and others [24]. If the wavenumber is allowed to be random too this structure breaks down. Figure 1.1b shows the superposition of 100 random plane waves with random wavenumber (the mean wavenumber is $\overline{k} = 50$ taken from a uniform distribution; minimum 10, maximum 90), random direction and phase but constant amplitude. This is a random speckled pattern and there are no scarlets. Figure 1.1b is also one unit wide by one unit high.

There appears to be more structure in mode shapes than just scarlets. Scars of periodic orbits have been observed in enclosures with completely chaotic ray dynamics, such as the stadium billiard by McDonald and Kaufman [25] and Heller [26]. They calculated high frequency mode shapes in the stadium billiard and found that some mode shapes were scarred by short periodic orbits. Figure 1.2 shows two modes scarred by periodic orbits. A mode which is scarred by a periodic orbit has higher amplitude in the region around a periodic orbit. The evidence seems to be indicating that many modes are scarred by periodic orbits. Heller says [3]

> "Since these scarred states are so ubiquitous (about half the states have one or more recognizable scars), it seems unlikely that *any* eigenstate of the stadium is ergodic."

Periodic orbits can either be stable, unstable or marginally stable. A periodic orbit is stable if a ray in the neighbourhood of the periodic orbit remains close to that periodic orbit as it evolves. An orbit is unstable if a ray in the neighbourhood of the periodic orbit diverges from the periodic orbit as it evolves. A periodic orbit is

(a) Superposition of 100 plane waves with constant wavenumber, $k = 50$, random phase and direction.

(b) Superposition of 100 plane waves with random wavenumber, $\bar{k} = 50$, random phase and direction.

Figure 1.1: Patterns of 100 superimposed plane waves.

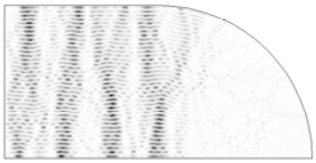

(a) Scarred mode of the quarter stadium, $k = 119.94$.

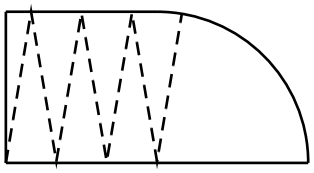

(b) Periodic orbit scarred.

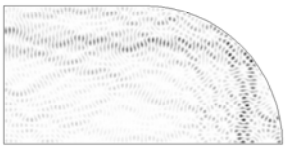

(c) Scarred mode of the quarter stadium, $k = 119.17$.

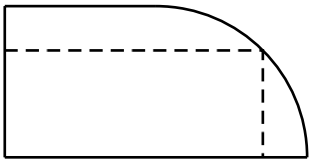

(d) Periodic orbit scarred.

Figure 1.2: Scarred modes of the quarter stadium.

marginally stable if a ray in the neighbourhood of the periodic orbit neither converges or diverges.

Recent work by Vergini [3, 27] (2000) has shown that mode shapes in a stadium-shaped enclosure can be approximated just using functions constructed using unstable short periodic orbits. These functions are called resonance functions and their derivation will be given in chapter 4. The Vergini theory will be called short periodic orbit theory (SPOT) here. The theory for unstable orbits was extended from theory for stable periodic orbits published in a book by Babič and Buldyrev [2] (1991). The original work was completed by Babič [28] (1968) and by Babič and Lazutkin [29] (1968).

1.8 Mode shape hypotheses

The central theme of this thesis will be to explore whether modes of a given enclosure can predominantly be explained in terms of periodic orbits. Two hypotheses are proposed here, the evidence for them will be investigated in the rest of the thesis. The first, the Mode Resonance Function Hypothesis, is a strong hypothesis.

Mode Resonance Function Hypothesis:
Every mode shape in a given enclosure is formed of resonance functions constructed on periodic orbits, and dominated by the short periodic orbits, in the semiclassical limit.

This hypothesis means that mode shapes are very strongly linked with the periodic orbits. A weaker hypothesis, the Mode Scar Hypothesis, is proposed as well.

Mode Scar Hypothesis:
Every mode shape in a given enclosure of sufficiently high frequency contains the scar of at least one short periodic orbit.

As stated these hypotheses are not really very testable. They will be restated later where they will be investigated with some examples.

These hypotheses will be assessed using the evidence that will be generated in this thesis. The level quality of evidence for these hypotheses will be discussed later. The results will be compared in the conclusion sections of the other chapters.

1.9 Thesis overview

The work in this thesis is based upon ray mechanics and so a brief review of the relevant topics will be given in chapter 2.

In chapter 3 the trace formula for the concentric annulus will be derived using work by Creagh and Littlejohn [1]. Mode count and the variance of the difference between the exact mode count and the mode count approximation will be calculated using the trace formula. The results will be compared to numerical approximations. Analysis of the behaviour of the mode count will be made using the insight provided by the trace formula.

Short Periodic Orbit Theory (SPOT) is derived in chapter 4. The stable orbit theory as developed by Babič and Buldyrev [2] and used by Tureci *et al* [30] is given first and then the work by Vergini [3] on unstable periodic orbits. The theory is extended to include impedance boundary conditions and the error of the constructions assessed. Examples are given for the quarter stadium, quadrupole, circle and eccentric annulus enclosures in chapter 5.

In chapter 6 the application of the short periodic orbit theory (SPOT) to the design of enclosures is explored. The eccentric annulus is used as the enclosure for the model problem. The connections between changes to the eccentricity and the resulting changes to the mode shapes are explored with reference to periodic orbits.

Chapter 7 gives the conclusions of the thesis, while chapter 8 gives possible avenues for future work. This includes extending the theory to flexural waves in

thin plates and to enclosures where the ray paths are curved rather than straight.

1.10 Summary of original work

The original contributions of this thesis are as follows:

- Derivation of the concentric annulus trace formula using the trace formula for continuous symmetries by Creagh and Littlejohn [1] (section 3.2). (The trace formula had previously been derived by Richter [31] by another method.)
- Semiclassical estimation of the mode count and variance of the difference between the exact and average mode count for the concentric annulus and analysis (section 3.3).
- Unified presentation of the derivation of the resonance function for the stable, unstable and marginally stable periodic orbits (sections 4.1 and 4.2).
- Derivation of the resonance function for impedance boundary conditions (section 4.5).
- Approximation of mode shapes in a domain with mixed chaoticity with Dirichlet, Neumann and impedance boundary conditions using short periodic orbit techniques (section 5.4).
- Approximation of mode shapes in an integrable domain using SPOT (section 5.5).
- Approximation of mode shapes in the eccentric annulus domain using SPOT (section 5.6).
- Proposal of a design loop to allow understanding of how a mode shape will change if the boundary is perturbed (chapter 6).

- Exploration of methods to find the periodic orbits that underlie a mode shape. The development of the ray angle function. Decomposition of mode shapes in an enclosure with integrable and chaotic regions of space (chapter 6).
- Tracking of changes of mode shapes with changing eccentricity with reference to periodic orbits (chapter 6).

Chapter 2

Ray Mechanics

This thesis seeks to link quantities in ray mechanics, especially the periodic orbits, to wave mechanics. Some ideas in ray mechanics are reviewed here and are used in later chapters.

Rays appear in the high frequency limit of the Helmholtz equation. The mathematical justification of this will be given in section 2.1. A consequence of this ray approximation is a method to approximate mode wavenumbers, which will be given in section 2.2.

The Poincaré section will be described for rays in enclosures in section 2.3. Rays travel in straight lines in the enclosures under consideration here, unless they hit the boundary of the enclosure where they reflect. The angle of incidence equals the angle of reflection at a reflection. The ray dynamics in the eccentric annulus will be used as an example. The eccentric annulus has some regions where the ray dynamics are integrable and other regions where the dynamics are chaotic.

Periodic orbits will be used extensively in this thesis, but the periodic orbits are difficult to find in a given enclosure. In section 2.4 some methods will be described for finding periodic orbits. The ray dynamics are important for understanding periodic orbits in two-dimensional shapes.

The stability of periodic orbits will be investigated using the monodromy matrix

in section 2.5. The monodromy matrix is a linearization in the region around the periodic orbit and will be used frequently.

2.1 WBKJ approximation

The WKBJ approximation is a high frequency approximation. It can be used to provide the mathematical foundation of rays in acoustics. The WKBJ ansatz [14]

$$\psi(\mathbf{x},k) = A(\mathbf{x};k)\exp(\mathrm{i}ku(\mathbf{x})) \quad \text{as} \quad k \to \infty, \tag{2.1}$$

is substituted into the Helmholtz equation. The derivatives of $\psi(\mathbf{x})$ are taken first:

$$\nabla\psi = (\nabla A + ikA\nabla u)\exp(\mathrm{i}ku) \tag{2.2}$$

$$\nabla^2\psi = \left(2ik\nabla u\nabla A - k^2A|\nabla u|^2 + \nabla^2 A + \mathrm{i}kA\nabla^2 u\right)\exp(\mathrm{i}ku). \tag{2.3}$$

In the high frequency limit terms of $O(k^2)$ dominate, so that the Helmholtz equation is reduced to

$$|\nabla u|^2 = 1. \tag{2.4}$$

This is the eikonal equation, which in two-dimensional Cartesian coordinates can be written as

$$\left(\frac{\partial u}{\partial x}\right)^2 + \left(\frac{\partial u}{\partial y}\right)^2 = 1. \tag{2.5}$$

The eikonal equation can be solved using Charpit's equations [14] and the solutions are equations for rays. If s denotes the arc length along the ray then the solution can be written as

$$u = u_0 \pm s, \tag{2.6}$$

where the sign ambiguity can be solved by taking s increasing in the direction in which u increases. The rays travel in the direction $|\nabla u|$, which is the direction of

the normal to the wavefronts [14]. The surface $u =$ constant is a surface of constant phase. Hence rays appear as solutions to the Helmholtz equation in the high frequency limit. The link between rays and waves established by the WKBJ method is fundamental to all of what follows.

2.2 EBK quantization

The information provided by the high frequency limit can be used to approximate some of the wave-like properties of the system, for example the EBK quantization of integrable systems is based on the WKBJ method. The work of Keller [15, 16] will be followed in this section. This provides an example of rays being used to approximate mode wavenumbers.

The function $\psi(\mathbf{x})$ must be single-valued when a ray has reflected around the enclosure and has returned to its starting position. The condition that must be satisfied for $\psi(\mathbf{x})$ to be single-valued is Keller [15, 16]

$$k\Delta u = 2n\pi + \mathrm{i}\Delta \log A, \tag{2.7}$$

where Δu denotes the change in u, $\Delta \log A$ is the change in $\log A$ over the ray path and n is a positive integer. If the rays between each bounce or contact with a caustic are joined together the above equation can be used to give the following expression Keller [15, 16]

$$k \oint \nabla u . \mathrm{d}\sigma = 2n\pi + \mathrm{i}\delta \log A, \tag{2.8}$$

where the path integral is along a ray and $\delta \log A$ is the total change in $\log A$ along the ray. The change of $\log A$ when passing through a caustic is $-i\pi/2$ and $\log A$ changes by $-i\pi$ for each reflection against a Dirichlet boundary condition. There is no phase change for a reflection against a Neumann boundary condition. This means that the

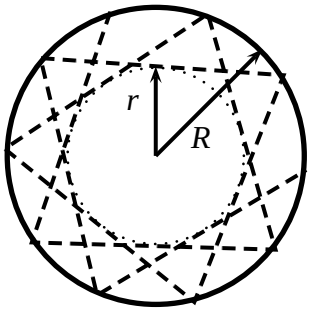

Figure 2.1: Circular enclosure with a ray (−−) bouncing inside. The dotted line denotes the caustic formed by the ray.

paths can be quantized as follows (Keller [15, 16])

$$k \oint \nabla u \, \mathrm{d}\sigma = 2\pi (n + m_c + m_d), \tag{2.9}$$

where m_c is the number of times the path crosses a caustic and m_d is the number of times the path touches a Dirichlet boundary condition.

2.2.1 Approximation of disk mode wavenumbers

An example of this theory is finding approximations to the mode wavenumbers in a disk as given in Keller [15, 16]. If a ray is allowed to propagate in a disk a circular caustic will be formed. The radius of the disk is R and the radius of the caustic is r, see figure 2.1.

Two linearly independent ray paths are required for this quantization method. The first will be taken to be the caustic curve itself and so equation (2.9) yields

$$k 2\pi r = 2\pi n_1, \qquad n_1 = 0, 1, 2 \cdots . \tag{2.10}$$

The second curve is taken to be along the ray path and then along an arc of the caustic curve so that it has three portions. The first two portions have length $(R^2 - r^2)^{1/2}$ and the length of the caustic arc is $2r\cos^{-1}(r/R)$. Using these lengths equation (2.9)

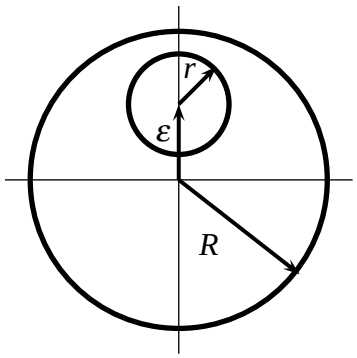

Figure 2.2: Eccentric annular billiard, eccentricity ε.

becomes

$$2k[(R^2-r^2)^{1/2}-r\cos^{-1}(r/R)]=2\pi(n_2+3/4) \qquad n_2=0,1,2\cdots. \tag{2.11}$$

Now equation (2.10) gives $r=n_1/k$ and so substituting this into equation (2.11) gives the expression for the approximation of the eigenvalues in the disk as Keller [15, 16]

$$[(kr)^2-n_1^2]-n_1\cos^{-1}\left(\frac{n_1}{kr}\right)=\pi\left(n_2+\frac{3}{4}\right) \qquad n_1,n_2=0,1,2\cdots. \tag{2.12}$$

This gives good estimates for the mode wavenumbers in the disk enclosure. This shows that approximations just using rays can provide information about the mode wavenumbers.

2.3 Poincaré section

The ray dynamics in an enclosure have to be understood if the rays are to be used to understand the modes. The Poincaré section will be used as a tool to display the ray dynamics.

The dynamics of rays in a two-dimensional enclosure are quite complex because

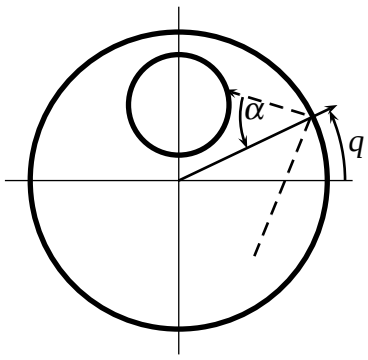

Figure 2.3: The annular billiard (after Gouesbet *et al*). The dashed line represents part of an orbit path, which bounces at q with momentum $p = \sin\alpha$.

at each point in the enclosure the ray will have a direction vector. This means four dimensions are required to describe the system completely. However, a Poincaré section of a section at the outer boundary will reduce it to a two-dimensional surface, the position being given as the distance q along the boundary and the momentum $p = \sin\alpha$ where α is the angle of incidence, see figure 2.3.

Figure 2.4 shows four eccentric annuli with different eccentricities. The eccentric annulus, see figure 2.2, is studied here because Gouesbet *et al* [32] have cataloged the periodic orbits up to six bounces for the case when $\varepsilon = 0.5$ and $r = 0.5$ when $R = 1$. Figure 2.5 shows four Poincaré sections one for each of the four eccentric annuli in figure 2.4. Each dot in these figures represents the position and momentum of the ray each time it hits the boundary. Rays are started at a number of different initial points and their paths recorded for seventy reflections.

Figure 2.5(a) shows the Poincaré section for a concentric annulus. There are two conserved quantities for this system; energy and angular momentum and so the dynamics are integrable. This can be seen from the horizontal lines on the Poincaré section. It is well known that the Helmholtz equation in this domain has an analytic solution. Figure 2.5(b) also has a region of horizontal lines which describes integrable motion, but it also has a region full of apparently randomly placed dots. This is a region associated with chaotic ray motion. In the chaotic region there are some areas that look more ordered appearing to be concentric circles of dots. These

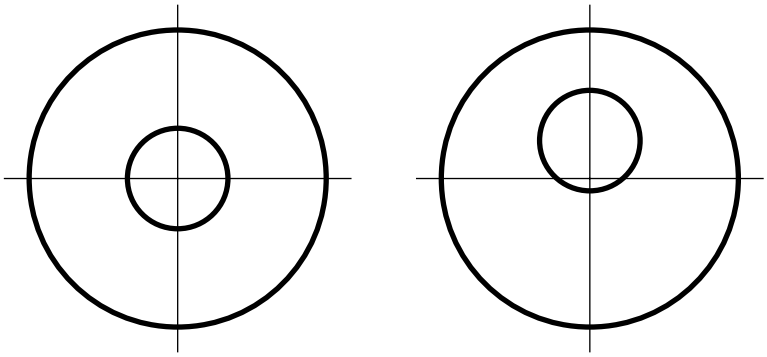

(a) $\varepsilon = 0$ (b) $\varepsilon = 0.25$

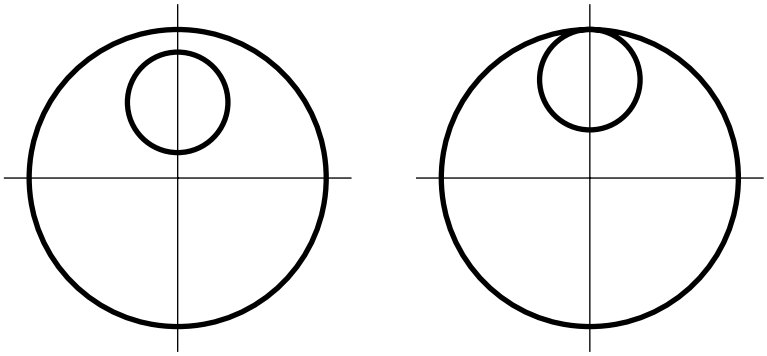

(c) $\varepsilon = 0.5$ (d) $\varepsilon = 0.65$

Figure 2.4: Annular enclosures with outer radius $R = 1$ and centre diameter $a = 0.35$. The eccentricity ε increases from $\varepsilon = 0$ to $\varepsilon = 0.65$.

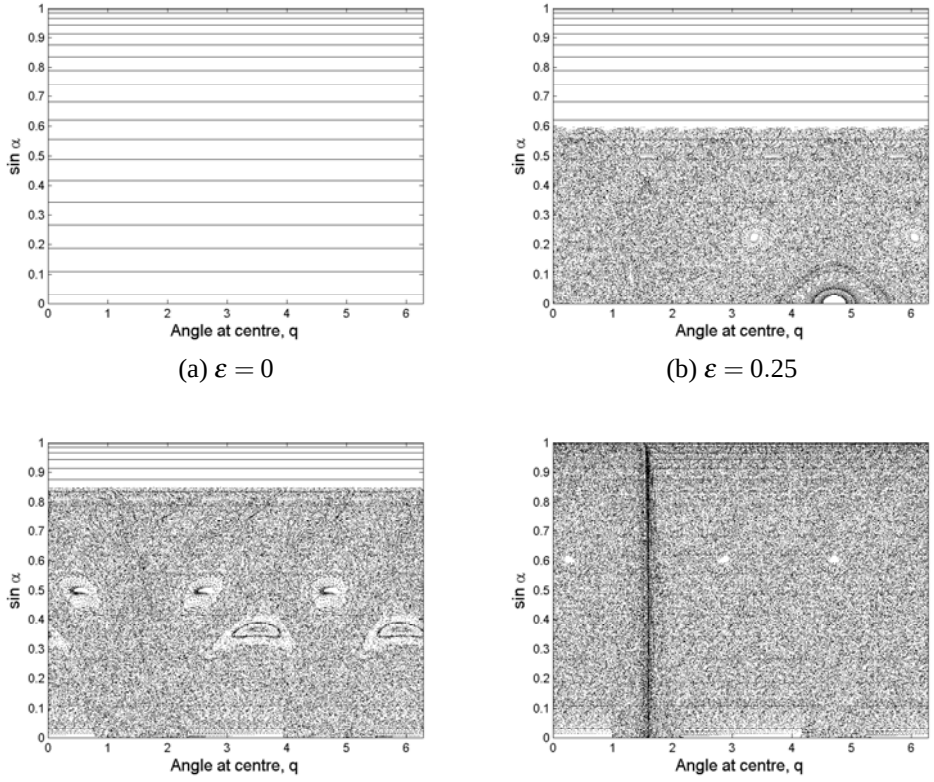

(a) $\varepsilon = 0$ (b) $\varepsilon = 0.25$

(c) $\varepsilon = 0.5$ (d) $\varepsilon = 0.65$

Figure 2.5: Poincaré section for four different values of eccentricity for the eccentric annulus.

are islands of stability which have a stable periodic orbit at their centre. It can be seen that as the eccentricity increases the chaotic portion of phase space increases too. Figure 2.5(c) corresponds to the system with the parameters used by Gouesbet *et al* [32]. If a domain has both integrable and chaotic regions it will be said to have mixed chaoticity. Figure 2.5(d) has the central hub touching the outer circle. This system is almost completely chaotic.

When enclosures are investigated later it will be important to know whether they are integrable, mixed or fully chaotic. Some of the methods presented require that the shape is integrable.

2.4 Short periodic orbits

Periodic orbits play a very significant role in semiclassical analysis. However, finding periodic orbits can be difficult. A review of one of the techniques used by Gouesbet *et al* [32] will be given here as an example.

Given initial conditions (q_0, p_0), where q_0 and $p_0 = \sin\alpha_0$ are position and momentum as before, the position after a given number of bounces N, (q_N, p_N), can be found. This allows the following quantities to be calculated

$$\Delta p(N) = p_N - p_0, \quad \text{and} \tag{2.13}$$

$$\Delta q(N) = q_N - q_0, \quad \text{modulo} \quad 2\pi. \tag{2.14}$$

A distance function can be defined from these equations

$$D(N)^2 = \Delta p(N)^2 + \Delta q(N)^2. \tag{2.15}$$

A periodic orbit of number of bounces N exists only if $D(N) = 0$. The quantity $D(N)$ can be searched for possible periodic orbits. The candidate periodic orbits can then be validated using analytical or numerical techniques.

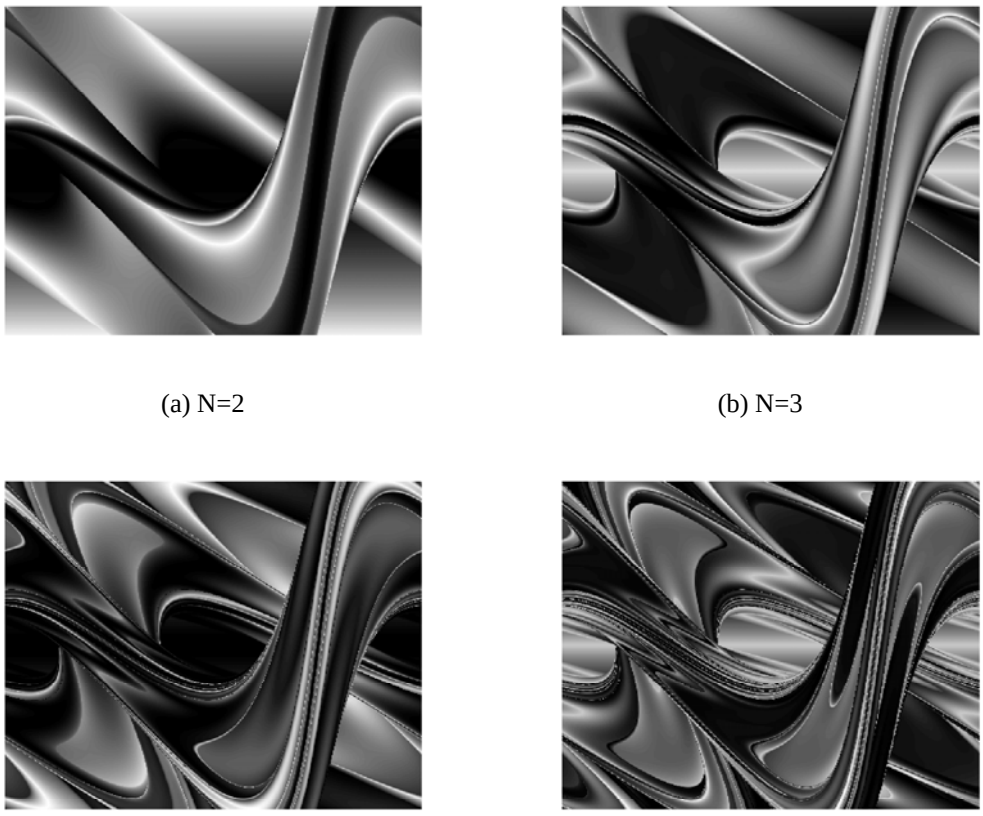

(a) N=2 (b) N=3

(c) N=4 (d) N=5

Figure 2.6: $D(N)^2$ with the number of bounces 2, 3, 4 and 5. The x-axis is initial q and the y-axis is the initial $\sin\alpha$ or p. The lighter the colour the smaller the value of $D(N)^2$.

$D(N)^2$ is plotted for 2, 3, 4 and 5 bounces against the outer boundary for the eccentric annulus with Gouesbet's parameters, $\varepsilon = 0.5$ and $r = 0.35$, in figure 2.6. However, it is not easy to determine periodic orbits quickly using this method. It can be seen from figure 2.6 that the zeros of the function $D(N)^2$ may be difficult to find.

Gouesbet *et al* [32] used other techniques to identify periodic orbits too. Most straightforwardly some periodic orbits may be found by inspection, especially bouncing ball orbits for example orbits labelled 1(1)1, 1(1)2 and 2(1)2 in figure 2.7. The notation used here to label the orbits is defined in Gouesbet *et al* [32]. The first number denotes the number of bounces against the outer boundary and the other numbers relate to the sequence of inner and outer boundary bounces. Stable periodic orbits

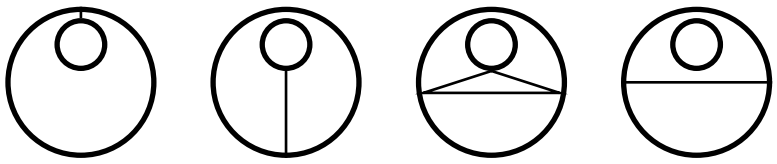

(a) Orbit 1(1)1 (length 0.15) (b) Orbit 1(1)2 (length 1.15) (c) Orbit 2(1)1 (length 4.04) (d) Orbit 2(1)2 (length 4)

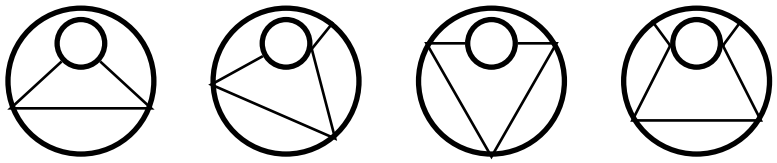

(e) Orbit 4(2)1 (length 3.705) (f) Orbit 5(4)3 (length 4.265) (g) Orbit 6(2)1 (length 4.495) (h) Orbit 6(8)1 (length 4.76)

Figure 2.7: The eight shortest periodic orbits in the eccentric annulus from Gouesbet *et al*. Radius of outer circle is one.

are at the centre of islands of stability in the Poincaré section and can be spotted very readily.

A large number of periodic orbits for the eccentric annulus are listed in [32] and figure 2.7 shows the shortest eight.

Another technique related to symbolic dynamics can also be used, Hansen [33]. In this method the boundary is cut up into segments in which the ray cannot bounce consecutively. All the bounce sequences are then listed for orbits with a given number of bounces. Only some of these sequences will be possible; all the impossible orbits are removed. The candidate sequence lengths are then minimized because periodic orbits often minimize the length of the path of these bounce sequences. Finally these orbits may be verified numerically.

In chapter 4 short periodic orbits will be a very important part of the method for approximating mode shapes. The ability to find periodic orbits is therefore very important to the method.

2.5 Monodromy matrix

The monodromy matrix is improtant for understanding the stability of a periodic orbit. The monodromy matrix is derived by linearizing the ray dynamics. A set of local coordinates is defined so that x is along the ray and y is in the direction perpendicular to the ray. The origin of the y direction can be defined so that $y = 0$ defines the ray itself. The quantities that are required for this linearization are the perpendicular position as a function of distance along the ray $Q(x)$ and the derivative of this quantity $Q'(x) = dQ(x)/dx \equiv P(x)$. $P(x)$ can be thought of as the momentum of a particle of unit mass tracing out the ray path.

The linearized propagation of a ray can be calculated using matrices, see for example Vergini [3] or Tureci *et al* [30]. The ray can propagate in a straight line a distance l from a position x as

$$\begin{pmatrix} Q(x+l) \\ P(x+l) \end{pmatrix} = \begin{pmatrix} 1 & l \\ 0 & 1 \end{pmatrix} \begin{pmatrix} Q(x) \\ P(x) \end{pmatrix} \equiv \mathbf{\Pi}(l) \begin{pmatrix} Q(x) \\ P(x) \end{pmatrix}. \tag{2.16}$$

This means that $P(x+l) = P(x)$ so that momentum is conserved. Also $Q(x+l) = Q(x) + lP(x)$ so this is a linear movement. The ray can also reflect at a boundary with radius of curvature R, therefore

$$\begin{pmatrix} Q(x_2) \\ P(x_2) \end{pmatrix} = \begin{pmatrix} 1 & 0 \\ \frac{-2}{R\cos\theta} & 1 \end{pmatrix} \begin{pmatrix} Q(x_1) \\ P(x_1) \end{pmatrix} = \mathscr{R}(\theta) \begin{pmatrix} Q(x_1) \\ P(x_1) \end{pmatrix}, \tag{2.17}$$

where θ is the angle of incidence of the ray with the boundary and x_1 is just before the bounce and x_2 is just after.

The matrix which propagates the ray right around a periodic orbit is called the monodromy matrix $\mathbf{M}(L)$. The monodromy matrix depends on the starting position but, wherever the starting position is chosen it gives a similar matrix, so the eigen-

values are the same. The monodromy matrix is thus

$$\mathbf{M}(L) = \mathbf{\Pi}(x - l_1)\mathscr{R}(\theta_m)\mathbf{\Pi}(l_m)...\mathbf{\Pi}(l_2)\mathscr{R}(\theta_1)\mathbf{\Pi}(l_1 - x), \tag{2.18}$$

where there are m bounces before the periodic orbit completes itself and its total length is

$$L = \sum_{j=1}^{n} l_j. \tag{2.19}$$

The trace of the monodromy matrix gives the stability of the orbit. If the trace is less than two the orbit is stable and the eigenvalues γ of the monodromy matrix $\mathbf{M}(L)$ are both complex, $\gamma_{\pm} = e^{\pm i\phi}$. If the trace is greater than two the orbit is unstable and the monodromy matrix has two real eigenvalues [18].

The periodic orbits within the integrable system only have marginally stable orbits; the trace of the monodromy matrix is exactly two. In fact the form of the monodromy matrix is

$$\mathbf{M}(L) = \begin{pmatrix} 1 & \varpi \\ 0 & 1 \end{pmatrix}, \tag{2.20}$$

where ϖ is a constant. The eigenvalues of the matrix are both one.

The monodromy matrix will be used extensively in calculating mode shape approximations in chapter 4 and also in determining the periodic orbit stability.

2.6 Concluding remarks

The mathematical derivation of rays has been given using the WKBJ method and this has been used to approximate the mode wavenumbers for the disk with Dirichlet or Neumann boundary conditions. This gives the first indication that ray theory will be useful in understanding modes. The link between waves and modes is important in all that follows.

The Poincaré section was presented for the annulus with several different ec-

centricities. This showed the difference between integrable and chaotic regions of phase space. It also showed how changing the eccentricity of the annulus changes the dynamics from integrable, when the eccentricity is zero, to fully chaotic, when the central disk touches the outer boundary.

Some methods for finding periodic orbits were discussed. In integrable enclosures finding periodic orbits is usually straightforward. However, in chaotic enclosures the problem is somewhat more difficult. Short periodic orbits will be used in much of the theory later so understanding methods for finding them is important

Linearization around the periodic orbits was discussed and the monodromy matrix was defined. The monodromy matrix allows the stability of the orbits to be calculated. The monodromy matrix will be used to determine stability and in the calculation of mode shape approximations.

Chapter 3

Concentric annulus trace formula

This chapter shows how periodic orbits in an integrable system can be used to model the spectrum of mode wavenumbers for the concentric annulus. The trace formula is a sum of a function over the periodic orbits of a system and it provides an approximation for the oscillating part of the level density.

This approximation for the level density can be used to provide an approximation to the mode count and the variance of the difference between the true and average mode counts for the concentric annulus. This variance allows confidence intervals to be calculated for the average mode count. The periodic orbit theory approximation is also used to understand certain aspects of the spectrum of the annular enclosure. This chapter follows an article by Wright and Ham [34].

Section 3.1 introduces the concentric annulus and gives the conditions for finding the modes. It gives the mode count and level density for the concentric annulus. It describes the problem of estimating the difference between the true and average mode counts. Section 3.2 introduces periodic orbit theory. The semiclassical trace formula for the concentric annulus is then derived. In section 3.3 the trace formula is used to provide mode count statistics and to analyse the spectrum of the concentric annulus. Conclusions are given in section 3.4.

3.1 Concentric annulus and mode count statistics

3.1.1 Exact annulus solutions

The modes of concentric annular enclosures are well known [34]. The outer radius of the annulus is R the inner radius is aR, where $0 \leq a \leq 1$, see figure 3.4a. The condition to be satisfied for k_{mn} to be an eigenvalue of the Helmholtz operator on the concentric annular domain with Dirichlet boundary conditions is

$$\mathrm{J}_m(aRk_{mn})\mathrm{Y}_m(Rk_{mn}) - \mathrm{Y}_m(aRk_{mn})\mathrm{J}_m(Rk_{mn}) = 0, \tag{3.1}$$

or, with Neumann boundary conditions is

$$\mathrm{J}'_m(aRk_{mn})\mathrm{Y}'_m(Rk_{mn}) - \mathrm{Y}'_m(aRk_{mn})\mathrm{J}'_m(Rk_{mn}) = 0, \tag{3.2}$$

where $\mathrm{J}_m(aRk_{mn})$ are Bessel functions of the first kind and $\mathrm{Y}_m(aRk_{mn})$ are Neumann functions of order m. The mode shapes are given by

$$\Psi(r) = A\mathrm{J}_m(rk_{mn}) + B\mathrm{Y}_m(rk_{mn}), \tag{3.3}$$

where r is the polar radius. The order of the mode in the radial direction is n. The trace formula will be used here to approximate the mode count. It should be noted that Chapman [35] has shown that the WKB method can be used to approximate the eigenvalues of a concentric annulus. This method still requires root finding and so does not provide the possibility of the analysis given here.

3.1.2 Average level density and mode count for the annulus

The average level density and the mode count are infinite expansions in $1/k$. The level density was defined in chapter 1. The first two terms in the approximation of

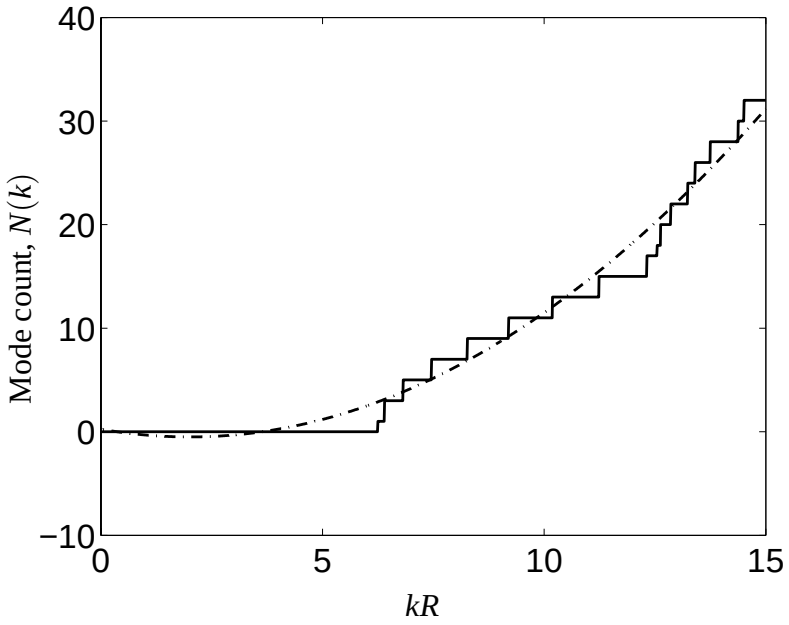

Figure 3.1: A three term approximation to the mode count ('-.-' line) and the exact mode count (solid line) for the annulus $a = 0.5$ with Dirichlet boundary conditions. The difference between these lines is the oscillating part of the mode count, $N_{\text{osc}}(k)$.

the level density for the concentric annulus are

$$\overline{\rho}(k) \approx \frac{R(1+a)}{2}(kR(1-a) \mp 1), \tag{3.4}$$

where the minus sign is for Dirichlet boundary conditions and the plus is for Neumann boundary conditions. The first three terms in the approximation of the mode count for the concentric annulus are

$$\overline{N}(k) \approx \frac{kR(1+a)}{2}\left(\frac{kR(1-a)}{2} \mp 1\right) + \frac{1}{4}. \tag{3.5}$$

A three term approximation to the mode count is compared against the exact mode count for the annulus in figure 3.1. Dirichlet boundary conditions will be assumed for the rest of the chapter.

3.1.3 Difference between true and average mode counts for the annulus

The error when $N(k)$ is approximated by $\overline{N}(k)$ is $N_{\text{osc}}(k)$, where $\overline{N}(k)$ is the first three terms of the approximation to the mode count. The relative difference between the exact mode count and the average mode count $(N(k)-\overline{N}(k))/N(k)$ can be readily calculated. This quantity is shown in figure 3.2. As expected the relative error falls as k increases. However, it remains at a level which may be significant for some applications. In fact, it is around 2% when $kR \approx 80$. This justifies interest in finding an error estimate for the mode count.

Figure 3.2 also shows that the relative error for $a = 0.4$ seems to be completely random, whereas the relative error for $a = 0.8$ appears to have oscillations on a scale of around $kR = 15$. This is because at $a = 0.8$ the annulus could be likened to a membrane that is long and thin. Modes with more excitations in the circumferential direction occur relatively often as frequency increases, but modes with more excitations in the radial direction will not occur as often. This means that the variance is large and has some structure with kR due to the relatively widely spaced cut-off frequencies of radial mode orders.

The variance of the oscillating term $N_{\text{osc}}(k)$ could be used to calculate a confidence interval around the average number of modes. It can be shown that $N_{\text{osc}}(k)$ grows as $\sqrt{k}$ so that $N_{\text{osc}}(k)/\sqrt{k}$ is stationary [22]. The variance of this quantity can be calculated as

$$\sigma^2\left(\frac{N_{\text{osc}}(k)}{\sqrt{k}}\right) = \lim_{\Omega\to\infty}\frac{1}{\Omega}\int_0^{\Omega}\left(\frac{N_{\text{osc}}(k)}{\sqrt{k}}\right)^2 \mathrm{d}k, \tag{3.6}$$

using the definition of the variance. This quantity is related to the spectral rigidity [22]. The spectral rigidity is the deviation of the mode count from the linear best fit when plotted against k^2. This method of finding an error estimate for the mode count is time-consuming for high frequencies because all the exact eigenvalues up to

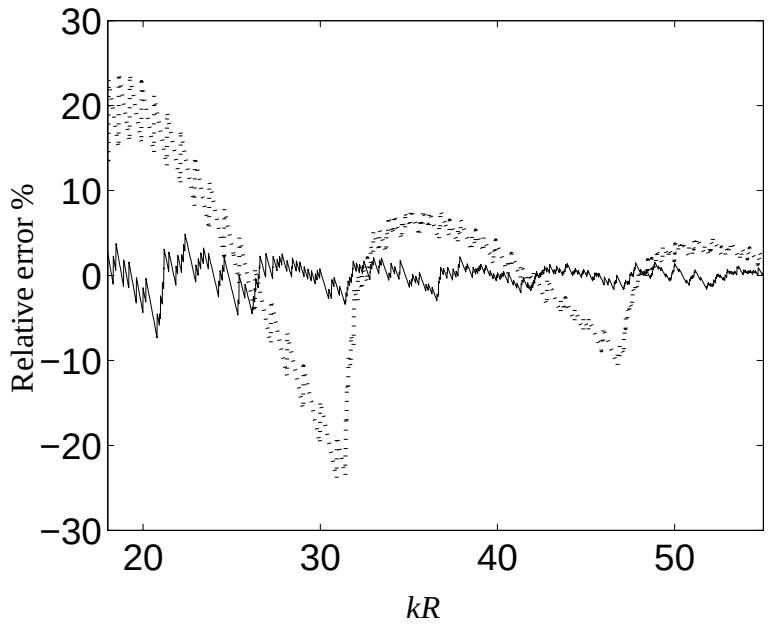

Figure 3.2: The relative error of the exact mode count to the average mode count $\left(\frac{N(k)-\overline{N}(k)}{N(k)}\right) \times 100$ for $a = 0.4$ (solid line) and $a = 0.8$ ('-.-' line) .

the required frequency must be found for the particular value of a. Figure 3.3 shows $N_{\text{osc}}(k)/\sqrt{k}$ for annuli with two different shape ratios a.

3.2 Annulus semiclassical trace formula

In this section the semiclassical trace formula will be derived, which will provide an approximation for the mode level density for the concentric annulus.

3.2.1 Periodic orbit theory

The level density can be found, without explicitly finding the exact eigenvalues of the system, using a semiclassical approximation. The trace formula is a sum over the periodic orbits of the enclosure [18], and it gives the oscillating part of the level density

$$\rho_{\text{osc}}(k) \approx \sum_{\gamma} \mathscr{A}_{\gamma} \cos(kL_{\gamma} - \phi_{\gamma}), \tag{3.7}$$

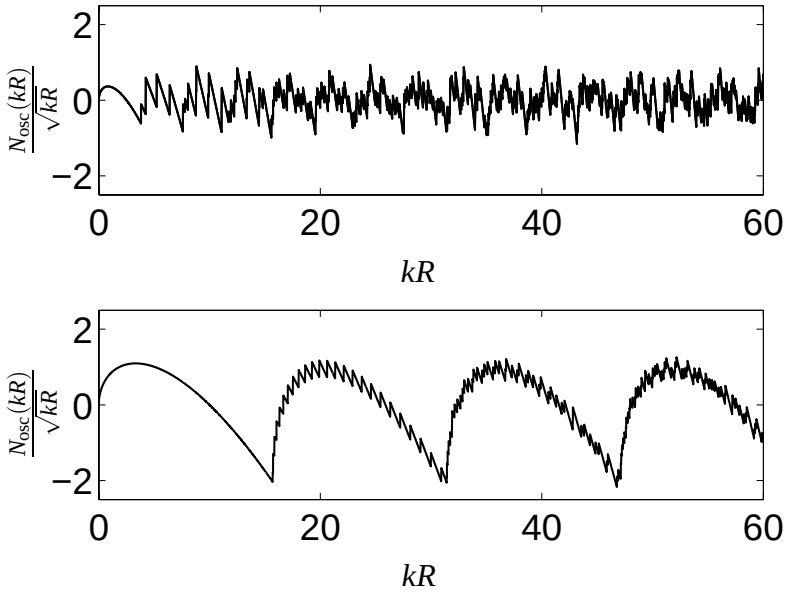

Figure 3.3: The oscillating part of the mode count divided by $\sqrt{kR}$ calculated using the exact eigenvalues for shape ratio $a = 0.2$ (top) and $a = 0.8$ (bottom).

where γ denotes a periodic orbit, $\mathscr{A}_\gamma$ is the amplitude associated with the orbit, L_γ is the length of the periodic orbit and ϕ_γ is a phase factor associated with the periodic orbit. An example of a periodic orbit in the annulus can be seen as the dashed line in figure 3.4a.

3.2.2 Semiclassical trace formula for continuous symmetries

The semiclassical trace formula for the concentric annulus was obtained by Richter [31, 36] who was interested in electrons confined in two-dimensional potentials and has been subsequently used by Mazzitelli *et al* [37] to study the Casimir effect between two concentric cylinders. Richter used the Berry and Tabor [20, 38] method for finding the trace formula for integrable systems. Snaith and Goodings [39] also studied the concentric annulus and included diffractive effects using the transfer method of Bogomolny [40].

The annulus trace formula will be derived here using the trace formula for continuous symmetries as given by Creagh and Littlejohn [1]. This formula can be simpli-

fied for a two-dimensional enclosure with axial symmetry [1, 18], which converted to wavenumber variables is

$$\rho_{\mathrm{osc}}(k) \approx \sqrt{\frac{2kR}{\pi}} \sum_{\gamma} \frac{L_\gamma \sqrt{\cos\psi}}{\alpha_\gamma |(\partial\Theta/\partial\psi)_\gamma|^{1/2}} \cos\Phi_\gamma, \tag{3.8}$$

where $\Phi_\gamma = kL_\gamma - (\mu_\gamma \pi/2) - \pi/4$, L_γ is the length of the periodic orbit and α_γ is the number of times the periodic orbit can be rotated onto itself. The Maslov index, μ_γ, is discussed in section (3.2.4) below. $(\partial\Theta/\partial\psi)$ measures the amount by which the periodic orbit fails to close when the initial angle has been perturbed. Θ denotes the angle of rotation necessary to bring the end point of the orbit back to the initial position, for example $\Theta = 0$ is the periodic orbit itself. ψ is the initial angle of the periodic orbit to the radius, see figure 3.5. The enclosure is assumed to have a constant outer radius R.

3.2.3 Annular periodic orbits

The periodic orbits for the annulus need to be found so that the quantities required by equation (3.8) can be derived for each orbit. There are two families of periodic orbit within the annulus enclosure: type I orbits, which do not touch the central inclusion, for example figure 3.4a and type II orbits, which do touch the central inclusion, for example figure 3.4b. The path length L_γ, $(\partial\Theta/\partial\psi)$ and $\cos\psi$ need to be calculated for each orbit.

Type I orbits

The length of the type I orbits is $L_{\mathrm{I},vw} = 2vR\sin\phi_{vw}$ where $\phi_{vw} = \pi w/v$, v is the number of times the orbit hits the outer boundary and w is the number of times the orbit winds around the centre. There is a relationship between the angle ϕ_{vw} and ψ in the case of the type I orbits, namely $\cos\psi = \sin\phi_{vw}$. Figure 3.5 shows the effect of a small perturbation on a type I orbit . Geometry can be applied to show that the

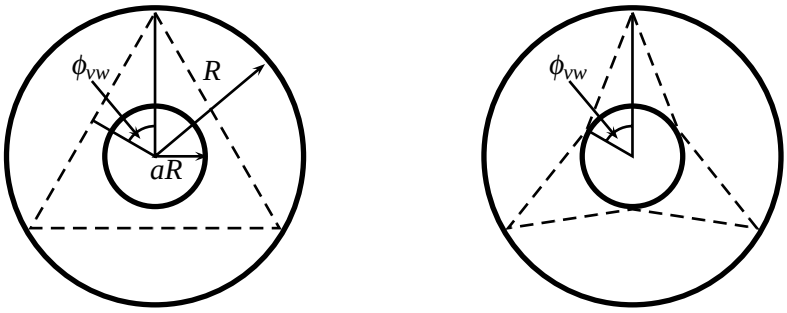

(a) A type I periodic orbit $(v,w) = (3,1)$ (dashed line)

(b) A type II periodic orbit $(v,w) = (3,1)$ (dashed line)

Figure 3.4: The two types of periodic orbit within an annular enclosure.

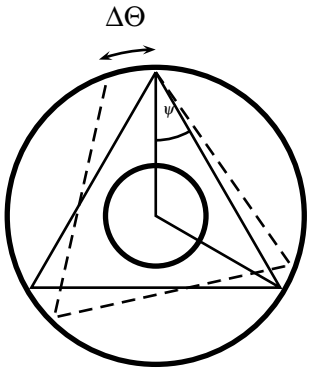

Figure 3.5: Unperturbed periodic orbit (solid line) and perturbed orbit (dashed line) for a type I orbit. $(v,w) = (3,1)$.

effect of a small perturbation on the initial angle is such that

$$\left|\frac{\partial\Theta}{\partial\psi}\right|_{\gamma} = 2v. \tag{3.9}$$

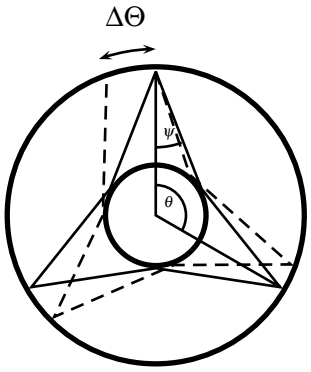

Figure 3.6: Unperturbed periodic orbit (solid line) and perturbed orbit (dashed line) for a type II orbit. $(v,w) = (3,1)$.

Type II orbits

The length of the type II orbits is $L_{\mathrm{II},vw} = 2vR\sqrt{1+a^2-2a\cos\phi_{vw}}$. The angle ψ has a much more complicated expression for the type II orbits and is such that

$$\cos\psi = \frac{(1-a\cos\phi_{vw})}{\sqrt{1+a^2-2a\cos\phi_{vw}}}. \tag{3.10}$$

Figure 3.6 shows the effect on the type II orbit of a small perturbation. Geometry is used as before to find the sensitivity to an initial perturbation for the type II orbits

$$\left|\frac{\partial\Theta}{\partial\psi}\right|_{\gamma} = \frac{2v(1-2a\cos\phi_{vw}+a^2)}{a(\cos\phi_{vw}-a)}, \tag{3.11}$$

where $\phi = \pi w/v$ for the orbit.

3.2.4 Maslov index

The full details of the Maslov index can be found in books on Quantum Chaology such as [4, 13, 18]. The Maslov index was originally associated with the WKBJ method and quantization [15, 16]. There are two contributions in the case of the concentric annulus. It counts the number of times the orbit grazes a caustic, with

Orbit	Boundary Condition	μ_b	μ_c	δ	μ_γ
Type I	Dirichlet	2ν	ν	1	$3\nu-1$
Type I	Neumann	0	ν	1	$\nu-1$
Type II	Dirichlet	4ν	0	0	4ν
Type II	Neumann	0	0	0	0

Table 3.1: The Maslov index for different orbits and boundary conditions

$\mu_{\mathrm{c}} = +1$ for each caustic touched. It also counts the number of bounces against a Dirichlet boundary condition, $\mu_{\mathrm{b}} = +2$ for each. There is no contribution from a bounce against a Neumann boundary condition. Connected to the Maslov index there is also a third contribution δ that needs to be added in Creagh and Littlejohn's formulation. If the sign of $\partial\Theta/\partial\psi$ is negative $\delta = 0$ and if positive $\delta = 1$. The total Maslov index $\mu_\gamma = \mu_{\mathrm{c}} + \mu_{\mathrm{b}} - \delta$ is just made up of these three parts. See table 3.1 for the particular values of the Maslov index for each type of orbit and boundary condition.

3.2.5 Annular trace formula

Putting the details calculated above in to equation (3.8) the trace formulae, equations (3.12) and (3.13), are obtained. The first few terms in the expansion in $1/k$ for the level density for the concentric annulus are

$$\rho_{\mathrm{I}}(k) \approx \sum_{w=1}^{\infty}\sum_{\nu=\nu_0}^{\infty} \sqrt{\frac{2k}{\pi}} \frac{L_{\mathrm{I},\nu w}^{3/2}}{\nu^2} \cos\left(kL_{\mathrm{I},\nu w} \pm \frac{\nu\pi}{2} + \frac{\pi}{4}\right), \tag{3.12}$$

for type I orbits and

$$\rho_{\mathrm{II}}(k) \approx \sum_{w=0}^{\infty}\sum_{\nu=\nu_0}^{\infty} f_{\nu w}\sqrt{\frac{8k}{\pi}} \frac{R^2}{L_{\mathrm{II},\nu w}^{1/2}} A_{\nu w} \cos\left(kL_{\mathrm{II},\nu w} - \frac{\pi}{4}\right), \tag{3.13}$$

for type II orbits, where the plus sign is for Dirichlet boundary conditions and the minus sign for Neumann. The orbits are indexed by ν and w, where ν is the number of times the orbit hits the outer boundary and w is the number of times the orbit

winds around the center. The index v starts from $v_0 = \lceil w\pi/\cos^{-1}(a)\rceil$, where $\lceil x\rceil$ denotes the smallest integer greater than or equal to x. The coefficient $f_{vw} = 2$ for all of the orbits except ones where $w = 0$ in which case $f_{v0} = 1$. Finally, $A_{vw} = \sqrt{(1-a\cos\phi_{vw})a(\cos\phi_{vw}-a)}$.

The level density formula is the sum of these two elements and the smooth part

$$\rho(k) \approx \overline{\rho}(k) + \rho_{\mathrm{I}}(k) + \rho_{\mathrm{II}}(k). \tag{3.14}$$

3.3 Modeling the annular spectrum

The level density formulae, equation (3.12) and (3.13), can be used to understand the spectrum of the annular enclosure. Equation (1.8) will be used to find an approximation for the mode count and equation (3.6) will provide an estimate of the variance so that an error estimate can be derived for the average mode count.

3.3.1 Annular mode count

The expressions for the level density are integrated to find the mode count. The integrals from the oscillating part of the level density are related to the Fresnel integrals by a change of variable and so an approximation is made for these integrals as follows:

$$\int_0^k \sqrt{k}\cos(kL+C)\mathrm{d}k \simeq \frac{\sqrt{k}}{L}\sin(kL+C) + O(k^0). \tag{3.15}$$

The constant terms of $O(k^0)$ are ignored in the following analysis because they are small compared to the other terms for large k. The mode count contribution for the type I orbits is

$$\begin{aligned} N_{\mathrm{I}}(k) = \quad & \frac{4R^{3/2}}{\sqrt{\pi}} \sum_{w=1}^{\infty}\sum_{v=v_0}^{\infty} \frac{\sin^{3/2}\phi_{vw}}{\sqrt{v}} \\ \times \quad & \frac{\sqrt{k}\sin(kL_{\mathrm{I},vw} \pm (v\pi/2) + (\pi/4))}{L_{\mathrm{I},vw}}, \end{aligned} \tag{3.16}$$

where v_0 is as previously described. The mode count for the type II orbits is

$$\begin{aligned} N_{\text{II}}(k) &= \frac{2R^{3/2}}{\sqrt{\pi}} \sum_{w=1}^{\infty} \sum_{v=v_0}^{\infty} f_{vw} \frac{A_{vw}}{\sqrt{v}(1-2a\cos\phi+a^2)^{\frac{1}{4}}} \\ &\times \frac{\sqrt{k}\sin(kL_{\text{II},vw}-\frac{\pi}{4})}{L_{\text{II},vw}}, \end{aligned} \tag{3.17}$$

The Maslov index for the type II orbits is either 0 or $4v$ so the extra terms from the Fresnel integrals cancel out. The extra terms from the Fresnel integrals for the type I orbits are negligible. The total mode count is therefore

$$N(k) \approx \overline{N}(k) + N_{\text{I}}(k) + N_{\text{II}}(k). \tag{3.18}$$

3.3.2 Variance of the difference between true and average mode counts for the annulus

Equation (3.6) along with the orthogonality of sine and cosine functions is used to calculate an estimate of the variance of the difference between the true and average mode counts for the annulus. Only the leading order terms are kept because the cross terms are negligible in the limit in equation (3.6). Only two terms are left, from the type I orbits

$$\begin{aligned} \sigma^2\left(\frac{N_{\text{I}}(k)}{\sqrt{k}}\right) &= \frac{8R^3}{\pi} \sum_{w=1}^{\infty} \sum_{v=v_0}^{\infty} \frac{\sin^3\phi_{vw}}{v{L_{\text{I},vw}}^2} \\ &= \frac{2R}{\pi} \sum_{v} \sum_{w} \frac{\sin\phi_{vw}}{v^3}, \end{aligned} \tag{3.19}$$

and from the type II orbits part

$$\sigma^2\left(\frac{N_{\text{II}}(k)}{\sqrt{k}}\right) = \frac{R}{2\pi} \sum_{w=0}^{\infty} \sum_{v=v_0}^{\infty} f_{vw}^2 \frac{A_{vw}^2}{v^3(1-2a\cos\phi_{vw}+a^2)^{3/2}}. \tag{3.20}$$

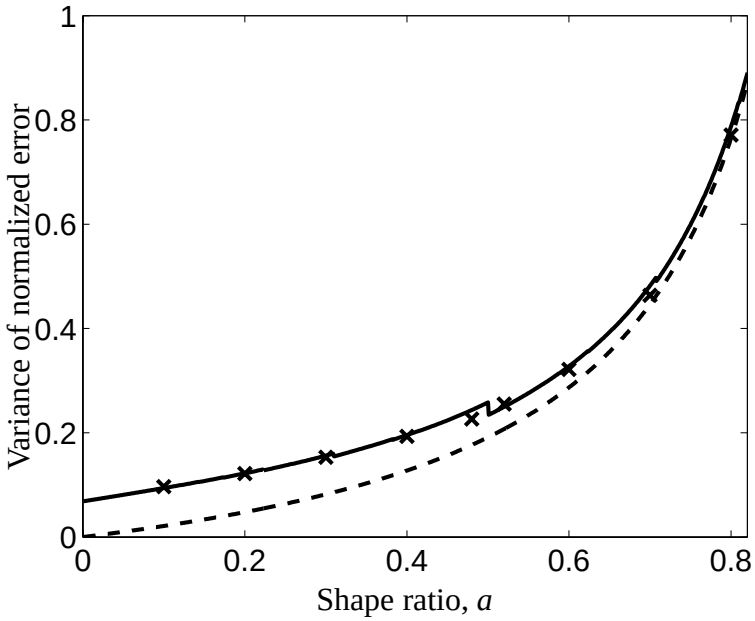

Figure 3.7: The variance calculated using the complete formula (solid line), the type II orbits with $w = 0$ alone (dashed line) and the variance estimated using analytic eigenvalues ($\times$). The variance was estimated using 5000 points between $k = 150$ and $k = 250$. The jumps in the solid line are explained in section 3.3.6.

The total semiclassical approximation to the variance of the difference between the exact mode count and the average mode count is just the sum of these two terms. This approximation is plotted with the variance calculated using the exact eigenvalues in figure 3.7.

3.3.3 Bouncing ball orbits and larger scale oscillation

The orbits that are type II with $w = 0$ travel via the shortest route between the inner and outer circles. This orbit dominates for large shape ratio, a. The variance for these orbits alone can be calculated from equation 3.20 by setting $w = 0$

$$\sigma^2\left(\frac{N_{\mathrm{II},w=0}(k)}{\sqrt{k}}\right) = \sum_{\nu}\frac{4R^3(1-a)a}{2\nu\pi L^2_{\mathrm{II},w=0}} = \frac{\zeta(3)}{\pi}\frac{aR}{2(1-a)}, \tag{3.21}$$

where $\zeta(3) = \sum_{n=1}^{\infty} n^{-3} = 1.202\ldots$ is Apéry's constant.

Figure 3.7 shows the contributions of the different types of orbit to the total vari-

ance. The type II orbits with $w = 0$ dominate for large shape ratio a. This means that the broad structure of the mode count could be well approximated by just taking the average mode count and the contribution of the type II orbits with $w = 0$ to the mode count. The rest of the type II and type I orbits are responsible for much smaller and seemingly more random variations. The jumps in the solid line are explained in section 3.3.6.

3.3.4 Degeneracy

The variance calculation assumes there are no cross terms. However, if two orbits have the same length there will be a cross term and this is called a degeneracy. There cannot be degeneracy between two orbits of the same type. Fortunately, these degeneracies are small compared to the variance so they can be safely ignored as explained in Wright and Ham [34].

3.3.5 Small shape ratios

The behaviour of the variance of the difference between the average and true mode counts for the concentric annulus as the shape ratio tends to zero, $a \to 0$, requires further thought. Consider two systems, the first a circular enclosure with Dirichlet boundary conditions and the second the same but pinned at the centre. The first few terms in the expansion in $1/k$ for the average mode count of the first system are

$$\overline{N}(k) \approx \frac{Rk}{2}\left(\frac{Rk}{2} \mp 1\right) + \frac{1}{4}. \tag{3.22}$$

The first few terms in the expansion in $1/k$ for the average mode count of the second system are calculated by considering the concentric annulus and letting the shape ratio tend to zero to give

$$\overline{N}(k) \approx \lim_{a\to 0} \frac{Rk(1+a)}{2}\left(\frac{Rk(1-a)}{2} \mp 1\right) + \frac{1}{4} = \frac{Rk}{2}\left(\frac{Rk}{2} \mp 1\right) + \frac{1}{4}. \tag{3.23}$$

Equations (3.22) and (3.23) are identical at leading order. This means that the eigenfunctions of the pinned circular drum are not those of the unpinned drum with the zeroth modes removed. There would be insufficient modes for the average mode count, equation (3.23), to be correct in this case. The paper by Gottlieb [41] concludes that the eigenvalues of the pinned drum will tend to the eigenvalues of the drum as $a \to 0$.

The eigenvalues of the concentric annulus tend to those of the circle as $a \to 0$ and thus the variance must approach that of the circle. However the periodic orbits going from one side of the circle to the other will be removed by a pin and hence the semiclassical estimate for the pinned drum is less than that of the unpinned drum. In fact the semiclassical estimate for the pinned drum would be

$$\frac{2R}{\pi} \sum_{w=1}^{\infty} \sum_{v=2w+1}^{\infty} \frac{\sin \phi_{vw}}{v^3} = 0.06855R. \tag{3.24}$$

The value for the unpinned drum would be $0.09246R$ so this is an underestimate.

The semiclassical estimate does not take account of diffraction, which is known to occur around the central circle in the annulus, Robinett [42, 43] see figure 3.8. It might be that the periodic orbits diffract around the central point, the smaller the central point the greater the effect. These diffracted periodic orbits should be included in the semiclassical sum and thus the semiclassical estimate of the variance would agree with that of the circle. This would agree with conclusions in Seba's paper on quantum billiards [44]. Rosenqvist *et al* [45] also deals with scattering from small disks and discusses the diffraction constant for a point scatterer. It is very difficult to produce convincing numerical estimates at very small values of a. This is because numerically finding the mode wavenumbers at small values of a is difficult.

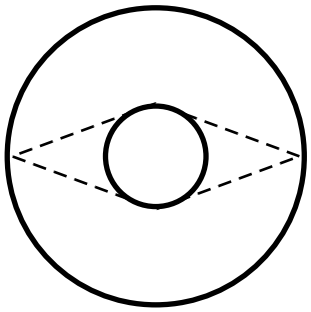

Figure 3.8: The dashed line shows the path of an orbit that is diffracted around the central inclusion of the annulus.

3.3.6 Variance step

The variance calculated using periodic orbit theory and the variance calculated using exact eigenvalues are a close fit. However a clear step can be seen in the periodic orbit variance formula at $a = 0.5$ which does not appear in the variance of the exact mode wavenumbers. There are also steps at $a = \cos\phi_{vw}$ for small values of v and w. These are the values of a for which a family of periodic orbits is destroyed. Figure 3.9 shows the variance in a region around $a = 0.5$, with the variance estimated from the analytic eigenvalues for points around $a = 0.5$. The variance from the analytic eigenvalues does not show a step. The step in the formula variance occurs because the triangular orbits of the type shown in figure 3.10 are all excluded from the type I orbit sum at $a = 0.5$. It is suggested that the stationary phase approximation which is involved in deriving the trace formula breaks down as the shape ratio $a = 0.5$ is approached from below for these orbits. If diffraction caused this the step would be expected to occur after $a = 0.5$ not before it.

There are steps that occur as the other short periodic orbits are removed such as one at $a = 1/\sqrt{2}$ associated with the square periodic orbit. The depth of these steps is much less than the one at $a = 0.5$ however.

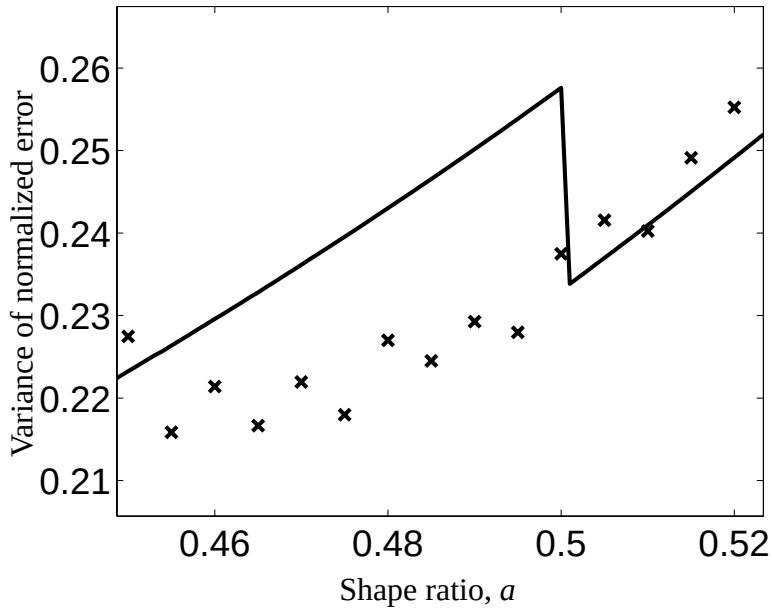

Figure 3.9: The variance calculated using equation (3.19) and equation (3.20), (solid line), which has a step at $a = 0.5$. The variance was estimated using 5000 points between $k = 150$ and $k = 250$, '$\times$'.

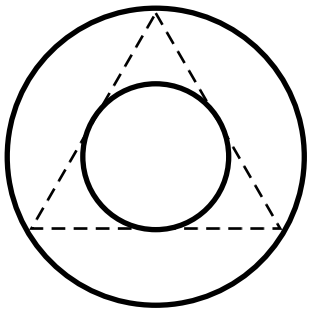

Figure 3.10: Path of a periodic orbit at $a = 0.5$.

3.4 Concluding Remarks

The exact solutions for the mode shapes in a concentric annulus enclosure for Dirichlet and Neumann boundary conditions were given. The average mode count was then compared to the exact mode count and the difference between the two was plotted. The variance of the difference between the true and average mode counts was defined.

A trace formula, which is a sum over periodic orbits, was derived for the concentric annulus enclosure using a more general trace formula for systems with axial symmetry by Creagh and Littlejohn [1]. This trace formula was used to derive an approximation to the oscillating part of the level density and thus the oscillating part of the mode count for the concentric annulus enclosure. The approximation is valid in the semiclassical limit.

The variance calculated using the semiclassical approximation has been compared to the variance calculated using the exact eigenvalues and it has been found to produce a good estimate at high but finite wavenumbers. The estimate of the variance can be used to provide an estimate of the error of the average mode count to the exact mode count for the annulus. The behaviour at small shape ratio has been investigated.

Periodic orbits were useful in this chapter to provide mode count statistics. However, the periodic orbits here could not provide any information on the mode shapes. The connection of periodic orbits to mode shapes will be investigated in the next chapters.

The periodic orbits do seem to provide useful information about the mode wavenumbers and to this extent the two hypotheses are supported, however the actual mode shapes were not approximated here.

Chapter 4

Short periodic orbit theory

In this thesis so far the mode wavenumbers have been approximated using periodic orbit theory. This is only useful up to a point. The mode shapes themselves are often required in applications. If an enclosure has integrable ray dynamics generally there is an analytic expression for the mode shapes, while for enclosures which have chaotic or partially chaotic ray dynamics there is not. If there is no analytic expression for the mode shapes a numerical technique can be used to approximate the mode shapes. Unfortunately, these techniques give no understanding of how the mode shapes are linked to the geometry of the enclosure. In this chapter a technique to approximate mode shapes will be developed, which is called Short Periodic Orbit Theory (SPOT). This theory provides a link between the geometry of the enclosure and the mode shapes via the periodic orbits.

The construction of semiclassical mode shape approximations using short periodic orbits depends upon the stability of the orbit. The stable orbit theory was detailed in a book by Babič and Buldyrev [2] based on earlier papers by Babič and Lazutkin [28, 29]. The theory relating to the resonances around stable periodic orbits given in Babič and Buldyrev [2] focuses on the multidimensional case. However, Tureci *et al* [30] have considered the two-dimensional construction for stable periodic orbits and their treatment will be followed in section 4.1.

The unstable orbit theory was proposed by Vergini [3] and developed with Carlo [27, 46, 47] much more recently. This will be reviewed in section 4.2. The constructions for the unstable periodic orbits are not themselves approximations to mode shapes. These constructions or resonance functions need to be combined to form the mode shape approximations. The theory for marginally stable orbits will also be presented. It has not been previously been published.

The mode shape approximations are semiclassical approximations so there is some error for finite wavenumbers. The error in the construction of these approximations will be estimated and discussed in section 4.3.

The approximation of mode shapes has previously been restricted to Dirichlet and Neumann boundary conditions, but is extended in this thesis to impedance boundary conditions in section 4.5. Some concluding remarks are made in section 4.7.

4.1 Resonance function construction on stable periodic orbits

A stable periodic orbit is defined as one with $\mathrm{Tr}(\mathbf{M}) < 2$ as seen in chapter 2. This section will be based on the derivation in Tureci *et al* [30], although this is just a two-dimensional version of the derivation given in Babič and Buldyrev [2].

Consider a two-dimensional enclosure with Dirichlet boundary conditions. This will be modelled with the Helmholtz equation

$$(\nabla^2 + k^2)\Psi(\mathbf{x}) = 0, \tag{4.1}$$

with the boundary condition

$$\Psi(\mathbf{x}) = 0 \quad \text{on} \quad \partial\mathscr{D}, \tag{4.2}$$

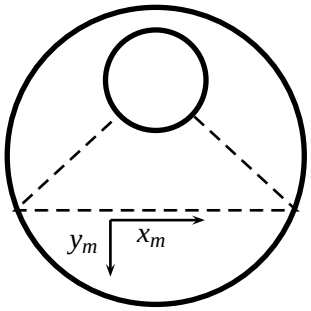

Figure 4.1: Periodic orbit (dashed line) in the eccentric annular billiard.

where $\mathscr{D}$ is the enclosure domain. The periodic orbit is split up into the straight sections between each bounce point. The resonance function is constructed along each straight section of the periodic orbit. The resonance function is then the sum of the resonance functions along each arm.

A particular periodic orbit has N bounces before it completes the orbit. The length of each arm is denoted as l_m and the total length is L where

$$L = \sum_{m=1}^{N} l_m. \tag{4.3}$$

A new coordinate system is defined based around the mth arm of the periodic orbit where x_m is along the orbit and y_m is perpendicular to it, see figure 4.1.

The solution of equation (4.1) can be written as

$$\Psi(X,Y) = \sum_{m=1}^{N} \Psi_m(x_m(X,Y), y_m(X,Y)), \tag{4.4}$$

where (X,Y) are the global coordinate set and (x_m, y_m) are the local coordinate sets. (x_m, y_m) are of course related to (X,Y) by a set of translations and reflections.

Tureci *et al* [30] now assumes that the main variation of the phase is in the x_m-

direction so that it can be factored out, therefore

$$\Psi_m(x_m, y_m, k) = \psi_m(x_m, y_m, k)\exp(\mathrm{i}kx_m). \tag{4.5}$$

The solutions given in equation (4.4) are substituted into equation (4.1) which gives

$$(\nabla_m^2 + k^2)\Psi_m = 0, \tag{4.6}$$

and the boundary condition, which is now given by

$$\Psi_m + \Psi_{m+1}|_{\partial D} = 0. \tag{4.7}$$

∇_m is the Laplacian expressed in local coordinates. Tureci *et al* [30] states that the solutions must be well localized and the reflection points well separated for these expressions to be valid.

The arm index m will now be dropped. Equation (4.5) is substituted into equation (4.6) and the factor $\exp(\mathrm{i}kx)$ dropped to give

$$\frac{\partial^2\psi}{\partial x^2} + \frac{\partial^2\psi}{\partial y^2} + 2\mathrm{i}k\frac{\partial\psi}{\partial x} = 0. \tag{4.8}$$

It is now assumed by Tureci *et al* [30] that after removal of the phase factor that the dependance in the x-direction is slow, so that $\partial\psi/\partial x \sim \psi/l$ and $\partial^2\psi/\partial x^2 \sim \psi/l^2$, where l is the typical length scale associated with the boundary. The high frequency limit implies that $l \gg \lambda$ where λ is the typical wavelength of the resonance. The transverse variation of ψ is assumed by Tureci *et al* [30] to occur on a scale $\sqrt{l\lambda}$ between the wavelength and the enclosure scale. This is so that the orders of the second and third terms of equation (4.8) are the same. This motivates a rescaling of

the y-direction so that $\tilde{y} = \sqrt{k}y$, which gives the following version of equation (4.8):

$$\frac{1}{k}\frac{\partial^2\psi}{\partial x^2} + \frac{\partial^2\psi}{\partial \tilde{y}^2} + 2\mathrm{i}\frac{\partial\psi}{\partial x} = 0. \tag{4.9}$$

The ψ_{xx} term can now be neglected because $kl \gg 1$. Thus the partial differential equation becomes

$$\mathscr{L}\psi(x,\tilde{y}) = \frac{\partial^2\psi(x,\tilde{y})}{\partial \tilde{y}^2} + 2\mathrm{i}\frac{\partial\psi(x,\tilde{y})}{\partial x} = 0. \tag{4.10}$$

This is a parabolic equation [14]. The following ansatz is made by Tureci *et al* [30]

$$\psi(x,y) = cA(x)\exp\left(\frac{\mathrm{i}}{2}\Omega(x)ky^2\right), \tag{4.11}$$

where c is an arbitrary constant. This ansatz is similar to the WKBJ approximation explained earlier. This ansatz is inserted into equation (4.10) and yields

$$\Omega^2 + \frac{\mathrm{d}\Omega}{\mathrm{d}x} = 0, \tag{4.12}$$

and

$$A\Omega + 2\frac{\mathrm{d}A}{\mathrm{d}x} = 0. \tag{4.13}$$

Tureci *et al* [30] make the substitution $\Omega(x) = Q'(x)/Q(x)$ ($P(x) \equiv Q'(x)$), where $Q(x)$ describes the position in the y-direction of a ray near to the periodic orbit as a function of x, thus

$$\frac{\mathrm{d}^2Q(x)}{\mathrm{d}x^2} = 0, \tag{4.14}$$

and

$$\frac{1}{Q}\frac{\mathrm{d}Q}{\mathrm{d}x} + \frac{2}{A}\frac{\mathrm{d}A}{\mathrm{d}x} = 0. \tag{4.15}$$

The solution to equation (4.14) is just $Q(x) = \alpha x + \beta$, so $Q(x)$ could be interpreted as a ray nearby the periodic orbit. The solution to equation (4.15) is $A(x) = Q(x)^{-1/2}$

so the final approximation on each arm is

$$\Psi_m(x,y) = \frac{c_m}{\sqrt{Q(x)}} \exp\left(\mathrm{i}kx + \frac{\mathrm{i}}{2}\frac{P(x)}{Q(x)}ky^2\right), \tag{4.16}$$

where c_m is a constant. This represents a plane wave in the direction of the periodic orbit arm and a Gaussian decay perpendicular to it.

4.1.1 Boundary conditions

The boundary conditions connect the approximations on consecutive arms of the periodic orbit. Putting the solution into equation (4.7) for the boundary conditions the explicit boundary condition becomes

$$\begin{aligned} & \frac{c_i}{\sqrt{Q_i(x_i)}} \exp\left(\mathrm{i}kx_i + \frac{\mathrm{i}}{2}\Omega(x_i)\tilde{y}_i^2\right) \\ + \quad & \frac{c_r}{\sqrt{Q_r(x_r)}} \exp\left(\mathrm{i}kx_r + \frac{\mathrm{i}}{2}\Omega(x_r)\tilde{y}_r^2\right)\Bigg|_{\partial D} = 0, \end{aligned} \tag{4.17}$$

where i subscript denotes the incident ray and r subscript denotes the reflected ray. Tureci *et al* [30] shows that this must be satisfied on an arc of the boundary of length $\sim \sqrt{\lambda l}$ around the reflection point. This length is much less than l so the boundary can be approximated by a circular arc of radius R. The phase and the amplitude before and after the bounce must be equal. The coordinates are transformed to the local normal, **n**, and tangent, **t** vectors at the bounce point. The coordinate transform equations are

$$x_i = l_m + t\sin\chi + n\cos\chi, \tag{4.18}$$

$$x_r = l_m + t\sin\chi - n\cos\chi, \tag{4.19}$$

$$y_i = t\cos\chi - n\sin\chi, \tag{4.20}$$

$$y_r = t\cos\chi + n\sin\chi, \tag{4.21}$$

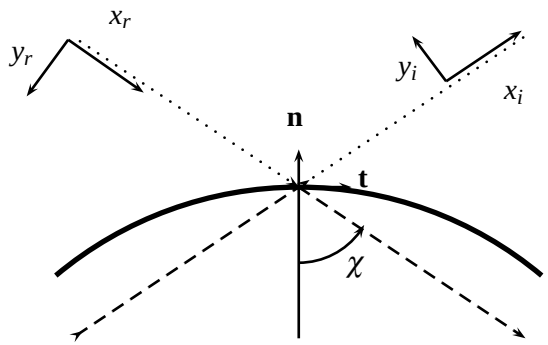

Figure 4.2: The solid line denotes a section of the boundary of the enclosure with radius of curvature R at the bounce point. The dashed lines show the paths of the incoming and reflected rays.

where $t = |\mathbf{t}|$ and $n = |\mathbf{n}|$. Figure 4.1.1 shows the boundary and the bounce point. The dotted lines extended outside of the enclosure to show the axes along each section, after [30]. The direction of positive y_i and y_r are arranged so that a ray with positive y will still be positive after the reflection.

Notice that the equation of the circle is given by $(n+R)^2 + t^2 = R^2$ so that $n^2 + 2nR + t^2 = 0$. Assuming n^2 is small yields $n = \frac{-t^2}{2R}$. The phase equation is given by

$$k \left(l_i + \frac{1}{\sqrt{k}}\tilde{t}\sin\chi - \frac{1}{k}\frac{\tilde{t}^2}{2R}\cos\chi \right) + \frac{1}{2}\frac{P_i}{Q_i}\left(\tilde{t}\cos\chi + \frac{1}{k}\frac{\tilde{t}^2}{2R}\sin\chi \right)^2 = k\left(l_i + \frac{1}{\sqrt{k}}\tilde{t}\sin\chi + \frac{1}{k}\frac{\tilde{t}^2}{2R}\cos\chi \right) + \frac{1}{2}\frac{P_r}{Q_r}\left(\tilde{t}\cos\chi + \frac{1}{k}\frac{\tilde{t}^2}{2R}\sin\chi \right)^2. \quad (4.22)$$

The amplitude equation is given by

$$\frac{c_i}{\sqrt{Q_i(x_i)}} + \frac{c_r}{\sqrt{Q_r(x_r)}} = 0. \quad (4.23)$$

It is assumed that $Q_r = Q_i$ so the phase conditions give

$$\begin{pmatrix} Q_r(x) \\ P_r(x) \end{pmatrix} = \begin{pmatrix} 1 & 0 \\ \frac{-2}{R\cos\theta} & 1 \end{pmatrix} \begin{pmatrix} Q_i(x) \\ P_i(x) \end{pmatrix} \equiv \mathscr{R} \begin{pmatrix} Q_i(x) \\ P_i(x) \end{pmatrix}. \quad (4.24)$$

This is the reflection condition previously given for the monodromy matrix. The amplitude equation gives

$$c_r = \mathrm{e}^{\mathrm{i}\pi} c_i. \quad (4.25)$$

The additional phase at each Dirichlet boundary condition is π as expected.

4.1.2 Quantization

The solution can now be propagated around the periodic orbit, but it must be single-valued after the ray has travelled around the orbit. Tureci *et al* [30] gives the following quantization condition

$$\Psi(x+L,y) = \Psi(x,y), \tag{4.26}$$

which further implies that

$$\psi(x+L,y)\mathrm{e}^{\mathrm{i}kL} = \psi(x,y). \tag{4.27}$$

This condition will only be solvable for discrete values of k. Equation (4.16) gives the equation for $\Psi(x,y)$. Tureci *et al* [30] points out that the phase $\Omega(x) = P(x)/Q(x)$ will be unchanged if $P(x+L)/Q(x+L) = P(x)/Q(x)$. This condition is met when (Q,P) is chosen to be an eigenvector of the monodromy matrix. If λ_1 is a given eigenvalue of the monodromy matrix then $P(x+L) = \lambda_1 P(x)$ and $Q(x+L) = \lambda_1 Q(x)$. The ratio $\Omega(x) = \Omega(x+L)$ thus remains unchanged. This only works for stable orbits because the eigenvectors and eigenvalues for the unstable or marginally stable cases are real and so there is no Gaussian decay perpendicular to the orbit.

The eigenvalues of the stable orbits come in complex conjugate pairs and so a choice must be made between them. Tureci *et al* [30] choose the eigenvector (Q,P) so that

$$PQ^* - QP^* = 2\mathrm{i}. \tag{4.28}$$

This condition also implies that $\Im\{\Omega\} > 0$, which means that the resonance decays properly in the perpendicular direction, where $\Im\{x\}$ denotes the imaginary part of x.

Noting that

$$Q(x+L)^{-1/2} = Q(x)^{-1/2}\exp(\pm \mathrm{i}\phi)^{-1/2} = Q(x)^{-1/2}\exp(\mp \mathrm{i}\phi/2). \tag{4.29}$$

This means that

$$\psi(x+L,y) = \exp(-i\phi/2 - \mathrm{i}\pi(\nu/2+N))\psi(x,y), \tag{4.30}$$

where ϕ is the Floquet phase, which is determined from the eigenvalue of the monodromy matrix $\lambda = \exp(\pm \mathrm{i}\phi)$. N is the number of bounces against a Dirichlet boundary condition during the periodic orbit and ν is the Maslov phase.

Tureci *et al* [30] state that the Floquet phase can be expressed as $\phi = \arg[Q(L)/Q(0)]$, where arg[.] denotes the principal argument. Equation (4.16) involves $\sqrt{Q(z)}$ and so the number of times $Q(z)$ goes around the origin will be important. Tureci *et al* [30] conclude that the actual phase advance will be $\phi + 2\pi\nu$ where

$$\nu = \left[\frac{1}{2\pi \mathrm{i}}\int_0^L \mathrm{d}(\ln Q(x))\right], \tag{4.31}$$

where $[.]$ denotes the integer part.

The rule for quantization in the enclosure is thus

$$k_{BS}L = \frac{\phi}{2} + 2\pi n + N\pi + \frac{\nu\pi}{2}, \tag{4.32}$$

where $n = 0, 1, 2...$ and k_{BS} is the Bohr–Sommerfeld wavenumber. This is the Bohr–Sommerfeld quantization rule.

4.1.3 Transverse excitations

The theory above allows only a Gaussian curve perpendicular to the direction of travel of the periodic orbit. However, oscillations perpendicular to the direction of

travel may be included [2, 30]. These oscillations will be called transverse excitations.

The ansatz, equation (4.16), is not the only possible solution to equation (4.10). It represents the lowest transverse excitation solution or the vacuum state as it is called by Vergini [46]. This vacuum state solution will be denoted as $\psi^{(0)}(x,y)$.

The theory of harmonic oscillators in quantum mechanics points to developing recursion relations. These are called creation and annihilation operators or up and down operators [48, 49]. These operators are defined [2] as

$$\Lambda(x) = -iQ(x)\frac{\partial}{\partial\tilde{y}} - P(x)\tilde{y}, \tag{4.33}$$

$$\Lambda^{\dagger}(x) = -iQ^{*}(x)\frac{\partial}{\partial\tilde{y}} - P^{*}(x)\tilde{y}, \tag{4.34}$$

where $\Lambda^{\dagger}(x)$ is the creation operator and $\Lambda(x)$ is the annihilation operator. The operators Λ and $\Lambda^{\dagger}$ do not commute but have the relationship

$$\Lambda\Lambda^{\dagger} - \Lambda^{\dagger}\Lambda = 1. \tag{4.35}$$

The differential operator $\mathscr{L}$, equation (4.10), commutes with both of these operators. This means that $\mathscr{L}\Lambda^{\dagger}\psi^{(0)}(x,y) = 0$ and $\mathscr{L}\Lambda\psi^{(0)}(x,y) = 0$ so that $\Lambda^{\dagger}\psi^{(0)}(x,y)$ and $\Lambda\psi^{(0)}(x,y)$ are both solutions of $\mathscr{L}$. It is straightforward to calculate that $\Lambda\psi^{(0)}(x,y) = 0$ and that $\Lambda^{\dagger}\psi^{(0)}(x,y) \neq 0$.

The $\Lambda^{\dagger}$ operator produces a new solution. This operator can be applied again so that $\Lambda^{\dagger}\Lambda^{\dagger}\psi^{(0)}(x,y)$ is also a solution and so on. This process produces a whole family of new solutions, which can be written as

$$\psi^{(m)}(x,y) = (\Lambda^{\dagger})^{m}\psi^{(0)}(x,y), \tag{4.36}$$

where $\psi^{(m)}(x,y)$ is the solution with m excitations.

There will be an extra phase term resulting from the use of the $\Lambda^{\dagger}$ operator. The

effect of travelling around the orbit on $Q^*(x)$ and $P^*(x)$ is

$$Q^*(x+L) = \mathrm{e}^{-\mathrm{i}\phi} Q^*(x), \tag{4.37}$$

$$P^*(x+L) = \mathrm{e}^{-\mathrm{i}\phi} P^*(x), \tag{4.38}$$

so that

$$\Lambda^\dagger(x+L) = \mathrm{e}^{-i\phi} \Lambda^\dagger(x). \tag{4.39}$$

This means that the solution will gain an extra phase of $-\phi$. If there are m excitations the Bohr–Sommerfeld quantization rule becomes

$$k_{BS} L = (m+\frac{1}{2})\phi + 2\pi n + N\pi + \frac{\nu\pi}{2}. \tag{4.40}$$

It is possible to use the creation and annihilation operators to find explicit forms of the new resonance functions. Tureci *et al* [30] give the explicit form for stable orbits as

$$\psi^{(m)}(x,y) = \left(\mathrm{i}\sqrt{\frac{Q^*(x)}{2Q(x)}}\right)^m H_m\left(\sqrt{\Im\left[\frac{P(x)}{Q(x)}\right]}\sqrt{k}y\right)\psi^{(0)}(x,y), \tag{4.41}$$

where H_m are the Hermite polynomials.

Alternatively, as given in [48], it is possible to show that the operator $\mathscr{L}$ is related to the equation

$$\frac{\mathrm{d}^2 u}{\mathrm{d}z^2} + (2\varepsilon - z^2)u = 0, \tag{4.42}$$

for a given transverse plane. In turn a solution of the form $u = F(z)\exp(-z^2/2)$ can be proposed and substituted. This yields

$$\frac{\mathrm{d}^2 F}{\mathrm{d}z^2} - 2z\frac{\mathrm{d}F}{\mathrm{d}z} + (2\varepsilon+1)F = 0, \tag{4.43}$$

which is Hermite's equation.

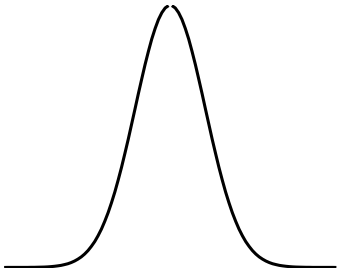

(a) No excitations in the transverse direction.

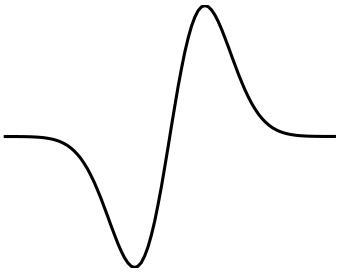

(b) One excitation in the transverse direction.

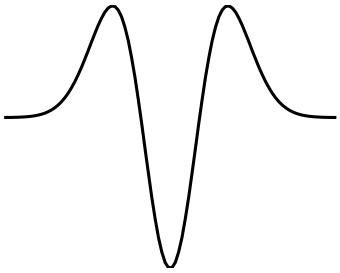

(c) Two excitations in the transverse direction.

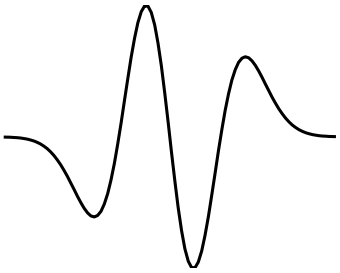

(d) Three excitations in the transverse direction.

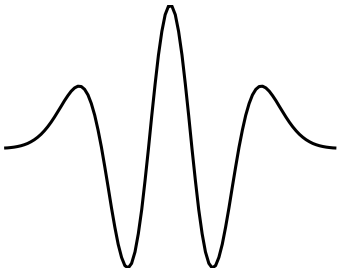

(e) Four excitations in the transverse direction.

Figure 4.3: First five levels of excitation transverse to the direction of travel of the periodic orbit.

Figure 4.3 shows a transverse slice of the first five levels of transverse excitation. Figure 4.3(a) shows a Gaussian which is used in the basic theory. Figures 4.3(b-e) show a Gaussian multiplied by the first four Hermite polynomials.

4.2 Resonance function construction on unstable periodic orbits

The theory for the unstable orbits is somewhat newer and has been developed by Vergini and others [3, 10, 27, 46, 47, 50–52], based on the the stable orbit theory. The method for the stable orbits cannot be used for the unstable orbits because the eigenvalues of the monodromy matrix have a non-zero real part. This means that the resonance function will not decay in the direction perpendicular to the periodic orbit. In fact some authors have stated that the unstable construction is not possible [30]. However, Vergini has been able to formulate a construction for unstable orbits. Vergini and Carlo [46] will be followed in this section.

An isolated unstable periodic orbit γ will be investigated here. This unstable periodic orbit will have a hyperbolic structure in phase space with a stable and unstable manifold [46]. The stable manifold in phase space is the manifold on which trajectories are purely attracted to the periodic orbit. The periodic orbit is a fixed point in phase space. The unstable manifold in phase space is the manifold on which trajectories are purely repelled from the periodic orbit.

Again, a coordinate system is also introduced based on the periodic orbit such that the x-axis is taken to be along the periodic orbit and the y-axis is perpendicular to it. Thus the periodic orbit itself will be where $y = 0$. The system can be linearized around the periodic orbit with the monodromy matrix.

The eigenvectors of the monodromy matrix are the stable and unstable manifolds; $\boldsymbol{\xi}_s$ and $\boldsymbol{\xi}_u$ respectively. The coordinate system will be changed so that the construction now takes place on these manifolds. The eigenvalue corresponding to

the unstable manifold is $\exp[\lambda L]$ where λ is the Lyapunov exponent for the periodic orbit. The eigenvectors evolve around the orbit as

$$\tilde{\boldsymbol{\xi}}_s(x) = \mathbf{M}(x)\boldsymbol{\xi}_s, \tag{4.44}$$

$$\tilde{\boldsymbol{\xi}}_u(x) = \mathbf{M}(x)\boldsymbol{\xi}_u. \tag{4.45}$$

The evolution around the full orbit of length L is then such that

$$\tilde{\boldsymbol{\xi}}_s(L) = (-1)^{\mu} e^{-\lambda L}\boldsymbol{\xi}_s, \tag{4.46}$$

$$\tilde{\boldsymbol{\xi}}_u(L) = (-1)^{\mu} e^{\lambda L}\boldsymbol{\xi}_u, \tag{4.47}$$

where μ is the number of half turns made by $\tilde{\boldsymbol{\xi}}_s(x)$ as it evolves around the orbit. These equations show that the stable and unstable manifolds return exactly to their starting positions after evolving around the orbit up to a change in sign. This means that a wavepacket started on the periodic orbit will evolve such that is has the greatest overlap with the original wavepacket after one complete period.

Vergini and Carlo [46] chose the origin of the of the x-axis so that the monodromy matrix has the property $m_{11}(L) = m_{22}(L)$ where

$$\mathbf{M}(L) = \begin{pmatrix} m_{11}(L) & m_{12}(L) \\ m_{21}(L) & m_{22}(L) \end{pmatrix}. \tag{4.48}$$

There are at least 2ν ways of choosing such a point [46], where ν is the Maslov index. This is not essential for the construction, but it is a mathematical convenience. The monodromy matrix can now be written as

$$\mathbf{M}(L) = (-1)^{\nu} \begin{pmatrix} \cosh(\lambda L) & \sinh(\lambda L)/\tan(\varphi) \\ \sinh(\lambda L)\tan(\varphi) & \cosh(\lambda L) \end{pmatrix}, \tag{4.49}$$

where λ is the Lyapunov exponent and $\tan(\varphi)$ gives the slope of the unstable mani-

fold and $-\tan(\varphi)$ is the slope of the stable manifold. Vergini and Carlo [46] change the axes so that the new ones are on the stable and unstable manifolds, $\boldsymbol{\xi}_s$ and $\boldsymbol{\xi}_u$ respectively. The matrix $\mathbf{B}$ which transforms the old coordinates to the new is

$$\mathbf{B} = (\boldsymbol{\xi}_u \quad \boldsymbol{\xi}_s) = (1/\sqrt{2}) \begin{pmatrix} 1/\alpha & -s/\alpha \\ s\alpha & \alpha \end{pmatrix}, \tag{4.50}$$

where $\alpha = \sqrt{|\tan(\varphi)|}$ and $s = \text{sign}(\varphi)$. The matrix $\mathbf{B}$ provides a transformation of the form $\mathbf{B}^{-1}\mathbf{M}(L)\mathbf{B} = (-1)^{\nu}\exp(\lambda L\mathbf{D})$ where $\mathbf{D}$ is the diagonal matrix with $d_{11} = 1$ and $d_{22} = -1$.

Next, Vergini and Carlo [46] decompose $\mathbf{M}(x)$ into a periodic matrix $\mathbf{F}(x)$, which describes the evolution of the manifolds, and a matrix that describes the contraction or dilation along the manifolds

$$\mathbf{M}(x) = \mathbf{F}(x)\exp(x\lambda\mathbf{K}) = \mathbf{F}(x)\mathbf{B}\exp(x\lambda\mathbf{D})\mathbf{B}^{-1}, \tag{4.51}$$

where

$$\mathbf{K} = \mathbf{B}\mathbf{D}\mathbf{B}^{-1} = \begin{pmatrix} 0 & 1/\tan(\varphi) \\ \tan(\varphi) & 0 \end{pmatrix}. \tag{4.52}$$

This decomposition represents the Floquet Theorem [46]. This equation defines $\mathbf{F}(x)$ in terms of $\mathbf{M}(x)$ so that

$$\mathbf{F}(x) \equiv \mathbf{M}(x)\exp(-f(x)\lambda\mathbf{K}) \tag{4.53}$$

where $f(x) = x$ will be used for simplicity, although other options are possible. The function $f(x)$ defines the contraction-dilation rate along manifolds. It is defined to have $f(0) = 0$ and $f(L) = L$. Vergini and Carlo [46] point out that $f(x) = x$ gives a uniform increment of length with x. Another choice could be $f(x) = t(x)L/T$ (where T is the period of the periodic orbit) and this would give a uniform increment of time

with x. Vergini and Carlo [46] show the effect of the $\mathbf{F}(x)$ matrix on the stable and unstable manifolds

$$\boldsymbol{\xi}_u(x) \equiv \begin{pmatrix} Q_u(x) \\ P_u(x) \end{pmatrix} \equiv \mathbf{F}(x)\boldsymbol{\xi}_u \equiv e^{-\lambda f(x)}\mathbf{M}(x)\boldsymbol{\xi}_u, \tag{4.54}$$

and

$$\boldsymbol{\xi}_s(x) \equiv \begin{pmatrix} Q_s(x) \\ P_s(x) \end{pmatrix} \equiv \mathbf{F}(x)\boldsymbol{\xi}_s \equiv e^{\lambda f(x)}\mathbf{M}(x)\boldsymbol{\xi}_s. \tag{4.55}$$

These equations mean that it is not necessary to explicitly evaluate $\mathbf{F}(x)$. Vergini and Carlo [46] also note the fact that $\mathbf{F}(x)$ is area preserving, which guarantees the following normalization condition

$$Q_s(x)P_u(x) - Q_u(x)P_s(x) = Q_sP_u - Q_uP_s = J. \tag{4.56}$$

Vergini and Carlo [46] state that the $\mathbf{F}(x)$ acts in a very unusual way; it is neither hyperbolic or elliptic. This means that all the orbits near the central periodic orbit are also periodic with length L.

It is now possible to calculate resonances based round the periodic orbits using similar equations to the stable orbit theory given earlier. Vergini and Carlo [46] give the resonance function in quantum mechanics variables, but in wavenumber variables it is

$$\Psi(x,y) = \frac{\exp(\mathrm{i}[kL + y^2\Omega(x)/2] - \mathrm{i}\phi(x)/2)}{\sqrt{L}[\pi(1/J)|Q(x)|^2]^{1/4}}, \tag{4.57}$$

where J is the unit area in the $Q-P$ plane. As before $\Omega(x) = P(x)/Q(x)$ with $Q(x)$ and $P(x)$ the components of the complex vector

$$\boldsymbol{\xi}_u(x) + \mathrm{i}\boldsymbol{\xi}_s(x) = \mathbf{F}(x)(\boldsymbol{\xi}_u + \mathrm{i}\boldsymbol{\xi}_s) = \mathbf{M}(x)\mathbf{B}\begin{pmatrix} \mathrm{e}^{-x\lambda} \\ \mathrm{i}\mathrm{e}^{x\lambda} \end{pmatrix} = \begin{pmatrix} Q(x) \\ P(x) \end{pmatrix}. \tag{4.58}$$

This means that $\mathbf{F}(x)$ does not need to be explicitly evaluated and the area-preserving property provides the normalization condition

$$Q^*(x)P(x) - Q(x)P^*(x) = 2\mathrm{i}J. \tag{4.59}$$

Finally the complex number $Q(x)$ sweeps out the angle $\varphi(x)$ while evolving from 0 to x and $\nu = \varphi(L)/\pi$ which is the Maslov index.

The accumulated phase around the orbit must be a multiple of 2π if $\Psi(x,y)$ is to be a continuous function. This again results in the Bohr-Sommerfeld quantization condition

$$k_{BS}L = 2\pi n + N\pi + \frac{\nu\pi}{2}, \tag{4.60}$$

where $n = 0, 1, ...$ is the number of excitations along the periodic orbit and N is the number of collisions with boundary.

4.2.1 Transverse excitations

Transverse excitations are possible for the unstable orbits as well. Vergini [46] gives the theory to include such excitations, which is derived in a similar manner to the stable orbit case. If there are m excitations the Bohr–Sommerfeld quantization rule becomes

$$k_{BS}L = 2\pi n + N\pi + (m + \frac{1}{2})\nu\pi. \tag{4.61}$$

The function used to produce the new mode shape functions becomes

$$\psi^{(m)}(x,y) = \frac{e^{-im\phi(x)}}{\sqrt{2^m m!}} H_m\left[\frac{y\sqrt{J}}{|Q(x)|}\right] \psi^{(0)}(x,y), \tag{4.62}$$

where H_m are the Hermite polynomials.

4.2.2 Marginal stable orbits

Marginally stable orbits have a monodromy matrix of the form

$$\begin{pmatrix} 1 & \varpi \\ 0 & 1 \end{pmatrix}, \tag{4.63}$$

and so both eigenvalues are exactly one. This means that neither the stable or unstable orbits method can be used to construct a resonance. A small perturbation to the length of each of the periodic orbit legs will be used in the calculation of the monodromy matrix only. This means that the perturbed orbit will either be stable or unstable [53].

The marginally stable orbits occur in integrable systems such as the square enclosure or the disk enclosure. This approximation allows the approximation of mode shapes in these domains, which has not been possible by this method before.

4.3 Error of the resonance functions

The error of the constructions is the extent to which the construction does not satisfy the Helmholtz equation. This is called the dispersion by Vergini and Carlo [46]. The error depends upon whether the periodic orbit is stable or unstable and so each case will be derived separately.

4.3.1 Stable orbits

The error for stable orbits will be calculated first. The formula used to construct the resonance function for each leg m of a stable periodic orbit is given by

$$\Psi_m(x,y) = \frac{c_m}{\sqrt{Q(x)}} \exp\left(\mathrm{i} k_{BS} x + \frac{\mathrm{i}}{2} \frac{P(x)}{Q(x)} k_{BS} y^2 \right), \tag{4.64}$$

where k_{BS} is the semiclassical wavenumber given by the Bohr-Sommerfeld quantization formula. The c_m are determined by matching the incoming and outgoing functions at the bounce points of the periodic orbit. The local coordinates of each leg are related to the global coordinates via translations and rotations. These same translations and rotations can be applied to the resonance function on each leg to give their location in global coordinates, Vergini [27]. The sum of these resonance functions on each leg in global coordinates produces the overall resonance function. This accounts for some of the interference type patterns that appear in the resonance functions. The resonance function is used to form the semiclassical approximation of the mode shape. The subscripts *BS* and *m* will be dropped for the rest of this section.

It is important to note here that $Q'(x) \equiv P(x)$ and that for stable orbits $P'(x) = 0$, which simplifies the derivatives with respect to x and y. The second order derivatives with respect to x and y are taken as follows

$$\frac{\partial \Psi}{\partial y} = \mathrm{i}yk\frac{P(x)}{Q(x)}\frac{c}{\sqrt{Q(x)}}\exp\left(\mathrm{i}kx + \frac{\mathrm{i}}{2}\frac{P(x)}{Q(x)}ky^2\right). \tag{4.65}$$

The second derivative with respect to y is

$$\frac{\partial^2 \Psi}{\partial y^2} = \left(\mathrm{i}k\frac{P(x)}{Q(x)} - y^2k^2\frac{P(x)^2}{Q(x)^2}\right)\frac{c}{\sqrt{Q(x)}}\exp\left(\mathrm{i}kx + \frac{\mathrm{i}}{2}\frac{P(x)}{Q(x)}ky^2\right). \tag{4.66}$$

The derivatives with respect to x are be taken next

$$\frac{\partial \Psi}{\partial x} = \left(\frac{-P(x)}{2Q(x)} + \mathrm{i}k - \frac{\mathrm{i}y^2k}{2}\frac{P(x)^2}{Q(x)^2}\right)\frac{c}{\sqrt{Q(x)}}\exp\left(\mathrm{i}kx + \frac{\mathrm{i}}{2}\frac{P(x)}{Q(x)}ky^2\right). \tag{4.67}$$

The second derivative with respect to x is

$$\begin{aligned}\frac{\partial^2\Psi}{\partial x^2} &= \frac{c}{\sqrt{Q(x)}}\exp\left(\mathrm{i}kx+\frac{\mathrm{i}}{2}\frac{P(x)}{Q(x)}ky^2\right) \\ &\times\left(\frac{1}{4}\frac{P^2(x)}{Q^2(x)}-k^2-\frac{y^4k^2}{2}\frac{P^4(x)}{Q^4(x)}\right. \\ &\left.-\mathrm{i}k\frac{P(x)}{Q(x)}+\frac{\mathrm{i}y^2k}{2}\frac{P^3(x)}{Q^3(x)}+y^2k^2\frac{P^2(x)}{Q^2(x)}+\frac{1}{2}\frac{P^2(x)}{Q^2(x)}+\mathrm{i}y^2k\frac{P^3(x)}{Q^3(x)}\right).\end{aligned} \tag{4.68}$$

Therefore, substituting the above into the Helmholtz equation

$$\begin{aligned}(\frac{\partial^2}{\partial x^2}+\frac{\partial^2}{\partial y^2}+k^2)\psi &= \frac{c}{\sqrt{Q(x)}}\exp\left(\mathrm{i}kx+\frac{\mathrm{i}}{2}\frac{P(x)}{Q(x)}\tilde{y}^2\right)\times \\ &\left[\frac{3}{4}\frac{P^2(x)}{Q^2(x)}-\tilde{y}^4\frac{P^4(x)}{Q^4(x)}+\frac{\mathrm{i}3\tilde{y}^2k}{2}\frac{P^3(x)}{Q^3(x)}\right],\end{aligned} \tag{4.69}$$

so that

$$(\nabla^2+k^2)\Psi(x,y)=0+O(1). \tag{4.70}$$

The approximation for stable orbits is therefore correct to $O(1)$ inside the domain.

4.3.2 Unstable orbits

The derivation of the error is more difficult for unstable orbits than for stable orbits because $P'(x)\neq 0$. The derivation given by Vergini [53] will be followed here. The starting point is the resonance function for each leg of an unstable periodic orbit

$$\Psi_m(x,y)=\frac{c_m}{\sqrt{Q(x)}}\exp\left(\mathrm{i}k_{BS}x+\frac{\mathrm{i}}{2}\frac{P(x)}{Q(x)}k_{BS}y^2\right), \tag{4.71}$$

where c_m is an arbitrary amplitude and k_{BS} is the semiclassical wavenumber given by the Bohr-Sommerfeld quantization formula. The subscripts BS and m will be dropped for the rest of this section. The partial derivatives are taken again up to

order k so that

$$\frac{\partial^2\Psi(x,y)}{\partial x^2} = -\left(k^2 + k^2y^2\frac{\mathrm{d}}{\mathrm{d}x}\frac{P(x)}{Q(x)} + \frac{\mathrm{i}k}{Q(x)}\frac{\mathrm{d}}{\mathrm{d}x}Q(x) + O(1)\right)\Psi(x,y), \tag{4.72}$$

and

$$\frac{\partial^2\Psi(x,y)}{\partial y^2} = -\left(k^2y^2\frac{P^2(x)}{Q^2(x)} - \mathrm{i}k\frac{P(x)}{Q(x)}\right)\Psi(x,y). \tag{4.73}$$

The derivatives of $Q(x)$ and $P(x)$ are given by

$$\frac{\mathrm{d}}{\mathrm{d}x}\begin{pmatrix} Q(x) \\ P(x) \end{pmatrix} = \begin{pmatrix} 0 & 1 \\ 0 & 0 \end{pmatrix}\mathbf{M}(x)\mathbf{B}\begin{pmatrix} \mathrm{e}^{-\lambda x} \\ \mathrm{i}\mathrm{e}^{\lambda x} \end{pmatrix} + \mathbf{M}(x)\mathbf{B}\begin{pmatrix} -\lambda\mathrm{e}^{-\lambda x} \\ \mathrm{i}\lambda\mathrm{e}^{\lambda x} \end{pmatrix}. \tag{4.74}$$

This equation can be simplified to

$$\frac{\mathrm{d}}{\mathrm{d}x}\begin{pmatrix} Q(x) \\ P(x) \end{pmatrix} = \begin{pmatrix} P(x) \\ 0 \end{pmatrix} - \lambda\begin{pmatrix} Q^*(x) \\ P^*(x) \end{pmatrix}. \tag{4.75}$$

This result can now be used to give the result in Vergini and Carlo [46]. The degree to which the resonance functions satisfy the Helmholtz equation semiclassically is

$$(\nabla^2 + k^2)\Psi(x,y) = -\mathrm{i}\lambda k\frac{Q^*(x)}{Q(x)}\left(\frac{2ky^2J}{|Q(x)|^2} - 1\right)\Psi(x,y) + O(1). \tag{4.76}$$

This derivation shows that the error for unstable orbits is of order k not order 1 as for the stable orbits. The error of the construction for unstable orbits therefore increases with wavenumber. Mode shapes will be approximated by a combination of these resonance functions so that the error of the mode shape approximations themselves will not increase with k.

Vergini [53] explains this by first normalizing the resonance functions

$$\int|\Psi(x,y)|^2\mathrm{d}x\mathrm{d}y \simeq \int_0^L \mathrm{d}x\int_\infty^\infty \exp\left(-\frac{kJy^2}{|Q(x)|^2}\right)\frac{\mathrm{d}y}{\sqrt{|Q(x)|^2}} = L\sqrt{\frac{\pi}{kJ}}, \tag{4.77}$$

where $\simeq$ denotes that this is a leading order approximation in k. The identity

$$\frac{P(x)}{Q(x)} = g(x) + \mathrm{i}\frac{J}{|Q(x)|^2}, \tag{4.78}$$

where $g(x) = (Q(x)P^*(x) + Q^*(x)P(x))/2|Q(x)|^2$ is a real function, has been used in the integration.

Vergini [53] then uses equation (4.76) with the normalized resonance functions to produce

$$\int \Psi^*(x,y)(\nabla^2 + k^2)\Psi(x,y)\mathrm{d}x\mathrm{d}y = O(1). \tag{4.79}$$

The significance of this equation can be seen by considering the enclosure mode wavenumbers k_ν and enclosure mode shape functions Φ_ν. The resonance functions used to approximate these mode shape functions will be denoted Ψ_n with the associated wavenumber k_n. The mode shapes will be approximated as $\Phi_\nu \simeq \sum a_n \Psi_n$, a combination where a_n are the required amplitudes of the resonance functions. This gives the following

$$\sum k_n |a_n|^2 = k_\nu^2 + O(1). \tag{4.80}$$

Thus showing the approximation does not get worse as k increases.

4.3.3 Error on the boundary

The error of the resonance functions on the boundary can also be calculated. This subsection follows unpublished work by Vergini [53].

Vergini has calculated the approximate error of the constructions on the boundary. An understanding of the types of resonance functions that have low error on the boundary may be important.

The same coordinate system will be used as for the construction of the resonance function at the bounce point on the boundary. The normal vector **n** and the tangent vector **t** at the bounce point will be used. The bounce point itself will be taken as the

origin.

Let the incoming ray have coordinates (x_1, y_1) and the outgoing (x_2, y_2). The incoming ray will hit the boundary at an angle of θ to the inward pointing normal vector. The coordinates can thus be reexpressed in terms of θ, t and n so that

$$x_1 = t\sin\theta + n\cos\theta, \tag{4.81}$$

$$y_1 = -t\cos\theta + n\sin\theta, \tag{4.82}$$

$$x_2 = t\sin\theta - n\cos\theta, \tag{4.83}$$

$$y_2 = t\cos\theta + n\sin\theta. \tag{4.84}$$

The distance along the boundary must also be approximated for this calculation. If an angle ϕ is subtended at the centre of the radius of curvature, this will represent a distance $q \approx R\phi$ travelled along the boundary or a distance $t \approx R\sin\phi$ along the tangent vector. Thus for small ϕ, $t = q$. The equation of the circle centred at the bounce point also yields $n \approx -t^2/2R$ so this further means that $n \approx -q^2/2R$.

Approximate expressions can now be derived for the resonance function on the incoming and out going rays. The expressions for (Q, P) are required first. Just before the bounce

$$\begin{pmatrix} Q(x_1) \\ P(x_1) \end{pmatrix} = \begin{pmatrix} 1 & x_1 \\ 0 & 1 \end{pmatrix} \begin{pmatrix} Q(x_0) \\ P(x_0) \end{pmatrix}. \tag{4.85}$$

In the other direction there is a bounce and then an evolution to x_2, which means that

$$\begin{pmatrix} Q(x_2) \\ P(x_2) \end{pmatrix} = \begin{pmatrix} 1 & x_2 \\ 0 & 1 \end{pmatrix} \begin{pmatrix} 1 & 0 \\ -2/R\cos\theta & 1 \end{pmatrix} \begin{pmatrix} Q(x_0) \\ P(x_0) \end{pmatrix}. \tag{4.86}$$

The construction on the incoming ray is

$$\psi_{\text{in}} = \frac{1}{\sqrt{Q(x_1)}} \exp(ikx_1 + \mathrm{i}k\frac{P(x_1)}{Q(x_1)}\frac{y_1^2}{2}), \tag{4.87}$$

and for the out going ray is

$$\psi_{\text{out}} = \frac{1}{\sqrt{Q(x_2)}} \exp(ikx_2 + \mathrm{i}k\frac{P(x_2)}{Q(x_2)}\frac{y_2^2}{2}). \tag{4.88}$$

The error on the boundary for a Dirichlet boundary condition is $\psi_{\text{in}} - \psi_{\text{out}} = \psi_{\text{Error}}$. On substituting in the above equations the expression on the boundary is

$$\begin{aligned} \psi_{\text{Error}} &= \frac{1}{\sqrt{Q(x_0)}} \exp\left(ikQ(x_0)\sin\theta + \mathrm{i}k\left(\frac{P(x_0)}{Q(x_0)} - \frac{1}{R\cos\theta}\right)\frac{\cos^2\theta Q(x_0)^2}{2}\right) \\ &\times \left(\frac{-Q(x_0)\sin\theta}{R}\left[1 + \mathrm{i}k\cos\theta\left(\frac{P(x_0)}{Q(x_0)} - \frac{1}{R\cos\theta}\right)Q(x_0)^2\right] + O(Q(x_0)^2)\right). \end{aligned} \tag{4.89}$$

Thus the error on the boundary is of order $Q(x_0)$ which means it is of order $k^{-1/2}$ since $Q(x_0) = O(k^{-1/2})$. However if $\theta = 0$, which are resonance functions which bounce perpendicular to the boundary, then the error is order k^{-1}. Therefore, bouncing ball type orbits should have less error.

4.4 Mode shape approximation

The fact that the error of the unstable orbits is of order k means that they have to be combined together to find approximations for mode shapes.

4.4.1 Resonance function basis

Mode shapes can be approximated for a given enclosure by combining resonance functions. There are many more resonance functions than modes in a given enclosure. Therefore a basis of resonance functions needs to be chosen. Vergini [3, 27] gives a method for constructing a basis of resonance functions.

The number of resonance functions required is given by the Weyl formula so that the number of resonances in the basis equals the average number of modes. If fewer resonance functions were chosen then the generalized eigenvalue problem

below would not produce approximations to all of the mode shapes. If too many resonance functions are included the problem becomes over specified and spurious mode shapes are produced often at wavenumbers outside the region of interest.

The resonances of the shortest periodic orbits are calculated first and the ones with the smallest error are used. It is helpful to pick a basis of resonance functions that are quasi-orthogonal. Excitations of the same periodic orbit, especially bouncing ball orbits, are generally quasi-orthogonal. Resonance functions calculated from bouncing ball periodic orbits are often chosen first.

The construction of a basis of resonance functions is not entirely straightforward. The process is not unique since the resonance functions are not orthogonal. Indeed different bases will provide different mode shape approximations. This will be discussed further in the next chapter when examples are given.

4.4.2 Combining resonances

Vergini [3] gives the following normalizations in the semiclassical limit, therefore as $k \to \infty$,

$$\int_{\mathscr{D}} \psi_\gamma^* \psi_\gamma \, \mathrm{d}\mathbf{r} \to 1. \tag{4.90}$$

The Helmholtz equation is also assumed to be satisfied in the semiclassical limit therefore

$$\int_{\mathscr{D}} \psi_\gamma^* (-\nabla^2 \psi_\gamma) \, \mathrm{d}\mathbf{r} \to \kappa^2, \tag{4.91}$$

where κ is the (approximate) mode wavenumber. Finally, the error in how the Helmholtz equation is satisfied in the semiclassical limit is

$$\sigma^2 \equiv \int_{\mathscr{D}} \psi_\gamma^* (-\nabla^4 \psi_\gamma) \, \mathrm{d}\mathbf{r} - \kappa^4 \to 2\kappa^2 \lambda^2, \tag{4.92}$$

where σ^2 is the error squared and λ is the Lyapunov exponent.

Unfortunately, interactions between resonance functions do not commute so that

$$\int_{\mathscr{D}} \psi_\delta^*(-\nabla^2\psi_\gamma)\,\mathrm{d}\mathbf{r} \neq \int_{\mathscr{D}} \psi_\gamma^*(-\nabla^2\psi_\delta)\,\mathrm{d}\mathbf{r}. \tag{4.93}$$

Vergini [3] defines the interaction between two resonance functions as

$$\int_{\mathscr{D}} \psi_\delta^*(-\nabla^2\psi_\gamma)\,\mathrm{d}\mathbf{r} \equiv \left[\int_{\mathscr{D}} \psi_\delta^*(-\nabla^2\psi_\gamma)\,\mathrm{d}\mathbf{r} + \left(\int_{\mathscr{D}} \psi_\gamma^*(-\nabla^2\psi_\delta\,\mathrm{d}\mathbf{r})\right)^*\right]/2. \tag{4.94}$$

This quantity is required for approximating the modes, see the next section.

4.4.3 Approximating modes

Vergini [3] states that the modes are constructed by combining the basis of resonance functions. Let the resonances functions be consecutive in energy $\psi_{\Gamma_1}, \psi_{\Gamma_1}, ..., \psi_{\Gamma_N}$, where $N > N_r$. The generalized eigenvalue problem

$$[\mathbf{A} - \kappa^2\mathbf{B}]\boldsymbol{\zeta} = 0, \tag{4.95}$$

where

$$A_{ij} = \int_{\mathscr{D}} \psi_i^*(-\nabla^2\psi_j)\,\mathrm{d}\mathbf{r}, \tag{4.96}$$

and

$$B_{ij} = \int_{\mathscr{D}} \psi_i^*\psi_j\,\mathrm{d}\mathbf{r} \tag{4.97}$$

produces the approximate mode wavenumbers, κ. The proportions of each resonance function to be combined to get the mode shape are given by $\boldsymbol{\zeta}$ [3].

4.4.4 Relative computational cost

It is difficult to compare the relative computational cost of SPOT with say FEM. If mode shapes need to be approximated at low wavenumbers, then FEM will be faster and more accurate at producing mode shapes than SPOT. However, at higher

wavenumbers a fine mesh will be required when using FEM to get accurate approximations. This will increase the computational cost of FEM considerably. The production of the mode shapes in figure 1.2 took approximately 30 minutes.

The computational time required by SPOT to find a large number of mode shapes given the resonance functions is of the order of seconds. However, finding the periodic orbits in a given shape can be very time consuming.

It is not suggested that SPOT be used as a replacement for methods such as FEM for finding mode shapes. However, FEM gives no understanding of why the mode shapes look as they do. SPOT provides a link between the geometry of the enclosure and the mode shapes via the periodic orbits.

4.5 Other boundary conditions

The construction can be made for other boundary conditions. The monodromy matrix will remain the same for all of the following boundary conditions. The effect of reflections on the phase at the boundaries must be calculated in each case. This phase is also required for the quantization of the orbit. The construction is semiclassical so only the leading order term in wavenumber k_{BS} is taken.

4.5.1 Neumann boundary conditions

The construction with Neumann boundary conditions has not been explicitly reported in the literature before. The Neumann boundary condition is

$$\frac{\partial \Psi}{\partial n} = 0 \quad \text{on} \quad \partial\Omega, \tag{4.98}$$

where $\mathbf{n}$ is the normal to the boundary. Constructions on incoming, Ψ_i, and reflected, Ψ_r, rays are considered at a bounce point. At the bounce point the sum of the incoming and outgoing constructions should be such that the boundary condition is

satisfied, therefore

$$\left(\frac{\partial \Psi_i}{\partial n}+\frac{\partial \Psi_r}{\partial n}\right)\Big|_{\partial D}=0. \tag{4.99}$$

The coordinates at the bounce point can be resolved to a new system tangential and normal to the boundary at the bounce point, as for Dirichlet boundary conditions. This means the construction

$$\Psi_i(x,y)=\frac{c_i}{\sqrt{Q_i(x)}}\exp\left(\mathrm{i}kx+\frac{\mathrm{i}}{2}\frac{P(x)}{Q(x)}ky^2\right), \tag{4.100}$$

can be written as

$$\begin{aligned}\Psi_i(t,n) &= \frac{c_i}{\sqrt{Q_i(l_i+t\sin\chi-n\cos\chi)}}\times \\ &\quad \exp\left(\mathrm{i}k(l_m+t\sin\chi-n\cos\chi)\right)\times \\ &\quad \exp\left(\frac{\mathrm{i}}{2}k\frac{P(l_m+t\sin\chi-n\cos\chi)}{Q(l_m+t\sin\chi-n\cos\chi)}(t\cos\chi+n\sin\chi)^2\right),\end{aligned} \tag{4.101}$$

where t denotes the magnitude of tangent vector at the bounce point and n denotes the magnitude of the normal vector. The following identities are used in this derivation

$$\frac{\partial P(x)}{\partial x}=0 \quad \text{and} \quad \frac{\partial Q(x)}{\partial x}=P(x), \tag{4.102}$$

and

$$\frac{\partial}{\partial x}\frac{1}{\sqrt{Q(x)}}=\frac{-1}{2}\frac{1}{\sqrt{Q(x)}}\frac{P(x)}{Q(x)}. \tag{4.103}$$

The normal derivative is

$$\frac{\partial \Psi_i(t,n)}{\partial n}=\frac{c_i}{\sqrt{Q_i(\varsigma_x)}}\exp\left(\mathrm{i}k(\varsigma_x)\right)\exp\left(\frac{\mathrm{i}}{2}k\frac{P(\varsigma_x)}{Q(\varsigma_x)}(\varsigma_y)^2\right), \tag{4.104}$$

where $\varsigma_x=l_m+t\sin\chi-n\cos\chi$ and $\varsigma_y=t\cos\chi+n\sin\chi$. This is substituted into equation (4.99) and on noting this is a semiclassical approximation, so that $k\to\infty$,

this gives

$$c_r = c_i. \tag{4.105}$$

This means there is no phase to be added for a bounce against a Neumann boundary condition.

4.5.2 Impedance boundary conditions

The impedance boundary condition is a more general case than Dirichlet or Neumann boundary conditions. In fact the Neumann boundary condition is just a special case of impedance boundary condition as will be seen.

Impedance boundary conditions arise, for example, in the case of lined ducts. The specific acoustic impedance is defined as [54]

$$z = \frac{p}{u_n}, \tag{4.106}$$

where p is the pressure and u_n is the particle velocity normal to the boundary. The linearized Euler equations can be written as

$$\frac{\partial u_n}{\partial t} = -\frac{1}{\rho_o}\frac{\partial p}{\partial n}, \tag{4.107}$$

where ρ_o is the mean density. Next, assume that the particle velocity and the pressure can be written as

$$u_n(\mathbf{x},t) = \hat{u}_n(\mathbf{x})\mathrm{e}^{\mathrm{i}\omega t}, \tag{4.108}$$

$$p(\mathbf{x},t) = \hat{p}(\mathbf{x})\mathrm{e}^{\mathrm{i}\omega t}. \tag{4.109}$$

This means that equation (4.107) can be written as

$$i\omega\hat{u}_n = -\frac{1}{\rho_0}\frac{\partial \hat{p}}{\partial n}. \tag{4.110}$$

The impedance boundary condition can be written as

$$\hat{p} = z\hat{u}_n \quad \text{at} \quad r = b. \tag{4.111}$$

Equation 4.110 can be used to write this as

$$\hat{p} = z\left(\frac{-1}{\mathrm{i}\omega\rho_0}\right)\frac{\partial \hat{p}}{\partial n} \quad \text{at} \quad r = b. \tag{4.112}$$

This means that

$$\frac{\partial \hat{p}}{\partial n} = \frac{\mathrm{i}\omega\rho_0\hat{p}}{-z}. \tag{4.113}$$

Now use $c_0 = \omega/k$ and $k = 2\pi/\lambda$ so that

$$\frac{\partial \hat{p}}{\partial n} = \frac{-\mathrm{i}k}{Z}\hat{p}, \tag{4.114}$$

where $Z = z/\rho_0 c_0$ which is the non-dimensional impedance. The non-dimensional admittance is $A = 1/Z$. The impedance is often written as $Z = R + \mathrm{i}X$. The typical values that might be expected for the lining of an aircraft engine would be $0.5 < R < 4$ and X is generally modelled as a function of frequency as $X \approx -\cot(kh)$, where h is the thickness of the liner. The impedance boundary condition is thus given as

$$\frac{\partial \Psi}{\partial n} = \mathrm{i}kA\Psi \quad \text{on} \quad \partial\Omega, \tag{4.115}$$

where A is a complex number, which may depend on the frequency of vibration. Now that the form of the impedance boundary condition has been established the same process as for Neumann boundary conditions is followed to find the phase change at the boundary. Incoming and outgoing rays at a bounce point are considered. The condition on the boundary is

$$\left(\frac{\partial \psi_i}{\partial n} - \mathrm{i}kA\psi_i + \frac{\partial \psi_r}{\partial n} - \mathrm{i}kA\psi_r\right)\Bigg|_{\partial D} = 0. \tag{4.116}$$

This is a semiclassical approximation again and so it is assumed that wavenumber is high. This means that only leading order terms in k are considered. This results in

$$\mathrm{i}k\cos\chi - \mathrm{i}kA - (\mathrm{i}k\cos\chi + \mathrm{i}kA)\,\frac{c_i}{c_r} = 0, \tag{4.117}$$

where χ is the angle of incidence of the periodic orbit ray at the bounce point and so

$$\frac{c_i}{c_r} = \frac{\cos\chi - A}{\cos\chi + A}. \tag{4.118}$$

The Bohr–Somerfeld quantisation Rule thus becomes

$$k_{BS}L = \frac{1}{2}\phi + 2\pi n + \frac{\nu\pi}{2} + \mathrm{i}\sum_{d=1}^{N}\log\frac{\cos\chi - A}{\cos\chi + A}. \tag{4.119}$$

for impedance boundary conditions. This is only based on leading order approximations.

4.6 Scar functions

Vergini and Carlo [46] also introduce what they call the scar function. This seeks to minimize the error of the construction by using a linear combination of resonance functions. In fact it is a linear combination of resonance functions on the same periodic orbit, but with increasing numbers of transverse excitations. The form of the scar function is

$$\phi_\gamma = \sum_{j=0}^{M} c_j \psi_\gamma^{(4j)} \Big/ \sqrt{\sum_{j=0}^{M} c_j^2}, \tag{4.120}$$

where c_j are the coefficients and M is the number of resonances included. The combination includes every fourth excitation for a given orbit because Vergini and Carlo [46] showed that the error of the resonance function with m transverse excitations is related to the resonance functions with $m+2$ and $m-2$ transverse excitations. If the error is calculated for the function in equation (4.120) then it will be possible to

arrange for the higher excitation error terms to cancel with each other.

In the wavenumber range that is being investigated here the benefit of using the scar functions is small. They will therefore not be included in the following work.

4.7 Concluding remarks

The theory for approximating mode shapes using periodic orbits has been given in this chapter. The stability of the periodic orbit is very important as this determines the method of calculation of the resonance function. The stable orbit version was developed by Babič *et al* first and the unstable orbit construction was developed recently by Vergini [3]. A small perturbation method was proposed for marginally stable orbits, which have not previously been approximated. The theory for transverse excitations has also been given for stable and unstable periodic orbits.

The error in the construction of the resonance functions has been analysed for the stable and unstable orbits. The error for the stable orbits is only $O(1)$, whereas the error for unstable orbits is $O(k)$ which suggests that the high frequency approximations to modes connected to stable periodic orbits will be much better. The error on the boundary local to the bounce point has also been estimated. If the periodic orbit bounces perpendicular to the boundary the error is reduced.

The theory for Neumann boundary conditions has been explicitly calculated. The theory has also been extended to allow resonance functions to be calculated for ducts with impedance boundary conditions.

The theory in this chapter suggests that mode shapes can be approximated using resonance functions in the semiclassical limit. This would support the two hypothesis. However the examples in the next chapter may help to establish whether mode shapes can be approximated in practice.

The following chapters investigate the use of SPOT to approximate mode shapes in different enclosure shapes and with different boundary conditions.

Chapter 5

Mode shape approximations using SPOT

The theory developed in the last chapter to approximate the mode shapes in enclosures will be used in this chapter on four different enclosure shapes, with different boundary conditions. The first two sections discuss some of the practical issues with approximating mode shapes. In section 5.3 short periodic orbit theory (SPOT) will be applied to the quarter stadium, which has completely chaotic ray dynamics [55]. The Dirichlet boundary condition case will be first, as calculated by Vergini and Carlo [27]. This will then be extended to the quarter stadium with a Neumann boundary condition on one of the boundary edges and Dirichlet on all of the others.

In section 5.4 SPOT will be applied to the quadrupole enclosure. The quadrupole was the shape used by Tureci *et al* [30] when studying the stable orbit construction. The quadrupole has mixed ray dynamics which means that it has both stable and unstable periodic orbits. The stable and unstable orbit theory has not previously been applied in the same shape. Dirichlet, Neumann and impedance boundary conditions will be considered for this enclosure.

In section 5.5 SPOT will be applied to the circle enclosure. The circle is an integrable shape and so all its periodic orbits are marginally stable. Finally, the

eccentric annulus with Dirichlet boundary conditions will covered in section 5.6. This enclosure has mixed dynamics and a hole in it, which provides another layer of complexity for the theory. Finally, some conclusions about the practical application of SPOT are given.

5.1 Mode hypothesis and comparing mode shapes

The Mode Resonance Function Hypothesis was framed in the first chapter. This hypothesis will be tested by calculating mode shapes using SPOT in this chapter. This hypothesis must be restated in a properly testable form first, but to do this a method for comparing modes shapes is required. SPOT is a semiclassical approximation, so demanding that the results match numerical approximations perfectly even at low wavenumber is unrealistic.

It is possible to compare the mode shapes produced by the finite element method and the semiclassical approximation qualitatively by plotting both cases next to each other. However, a quantitative method is required here so this is not satisfactory. Vergini [3] uses a quantity called the overlap between the two mode shapes. This is very similar to the 'Modal Assurance Criterion' (MAC) [56]. The MAC is defined as

$$MAC(N,S) = \frac{\left|\sum_{j=1}^{n}(\Psi_N)_j(\Psi_S)_j^*\right|^2}{\left(\sum_{j=1}^{n}(\Psi_S)_j(\Psi_S)_j^*\right)\left(\sum_{j=1}^{n}(\Psi_N)_j(\Psi_N)_j^*\right)}, \tag{5.1}$$

where Ψ_N is the mode shape calculated numerically and Ψ_S is the semiclassical approximation to the mode shape. The mode shapes are both assumed to be calculated over the same grid of points. Ewins [56] states that a MAC of over 90% should be attained for well correlated modes. The overlap is the square root of the MAC and so an overlap of around 95% is required for well correlated modes.

The figure given by Ewins [56] is intended for comparing experimental results to analytical or numerically approximated modes. The aim in this thesis is slightly

different. It is known that the SPOT approximations will contain semiclassical errors so a slightly lower figure will be used. An overlap of 90% or more will indicate well correlated modes. Although, the figure of 90% for the overlap is arbitrary it gives a criterion to assess the results. This figure could be strengthened or weakened depending on the situation.

The Mode Resonance Function Hypothesis can now be restated in a more testable form:

Mode Resonance Function Hypothesis:
The first 20 mode shapes in a given enclosure can be approximated using the resonance functions based on a given set of short periodic orbits. The mode shape approximations have an overlap of 90% or more with the numerical approximation to the mode shape.

It may be possible that the Mode Resonance Hypothesis is valid for certain enclosures and not for others. It should be noted that the choice of the first 20 modes was arbitrary. Sufficient modes are required to demonstrate whether the method is working, but not so many as to make the computation of examples onerous. Vergini and Carlo [27] calculated the first 25 mode shapes.

5.2 Resonance function basis selection

The selection of the basis of resonance functions is important to the overall success of SPOT approximation. The error calculation in chapter 4 indicates that the stable orbits should be used primarily, since the error of their resonance functions increases as $O(1)$ rather than $O(k)$ for the unstable orbits.

The periodic orbits that are chosen to generate the resonance functions are generally the shortest available from the catalogue of periodic orbits available. These are the orbits that dominate the SPOT approximation. The periodic orbits chosen should

also travel through the main part of the enclosure. The bouncing ball orbits and the short periodic orbits which retrace their orbit path are often of particular importance.

It is advantageous to choose all the excitations from one periodic orbit once that periodic orbit has been included because the resonance functions of an orbit are approximately orthogonal with each other. This generally means that the mode shapes are better approximated.

An algorithm for selecting the resonance functions was attempted but unfortunately the results were not as good as could be obtained when the basis was improved by hand. The basis selected by Vergini and Carlo [27] for the quarter stadium rests heavily on the 'bouncing ball' regime. This does not transfer to other enclosures in a straightforward manner. Further investigation into optimal basis selection is required. A proof of principle is demonstrated here.

5.3 Quarter stadium enclosure

Vergini and Carlo [27] constructed the first 25 mode shapes in the quarter stadium enclosure with Dirichlet boundary conditions using only 5 short periodic orbits. This was the first example of mode shape construction using the unstable orbits. Vergini and Carlo [27] used the symmetry of the quarter stadium in their construction. In general, symmetry will not be available to simplify the problem. The method used here will not use the symmetry of the quarter stadium to approximate the mode shapes. The full stadium mode shapes will be calculated using the full stadium periodic orbits. The odd-odd symmetry mode shapes in the full stadium will be approximated because these correspond to the quarter stadium with Dirichlet boundary conditions. Only a quarter stadium will be plotted so that the results can be compared to those in Vergini and Carlo [27].

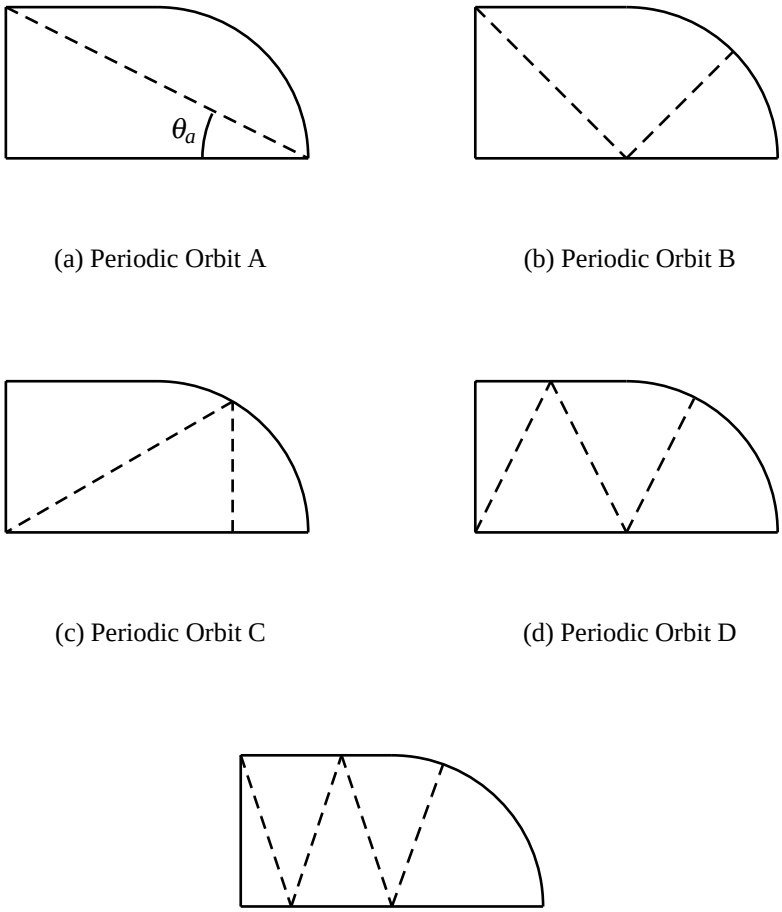

(a) Periodic Orbit A

(b) Periodic Orbit B

(c) Periodic Orbit C

(d) Periodic Orbit D

(e) Periodic Orbit E

Figure 5.1: Desymmetrized short periodic orbits for the stadium billiard, after Vergini and Carlo.

5.3.1 Periodic orbits in the quarter stadium

First, the short periodic orbits that will be used for the construction are shown in figure 5.1. All of these orbits are unstable and so the resonances must be constructed using Vergini's formulation. The quarter stadium periodic orbits map to the full stadium periodic orbits by using reflections at the boundary.

5.3.2 Attributes of the periodic orbits

The monodromy matrices, given in Vergini and Carlo [27], for each of these orbits is calculated next. The boundary conditions do not affect the monodromy matrix. The straight line evolution matrix is defined as

$$\mathbf{M}_1(l) = \begin{pmatrix} 1 & l \\ 0 & 1 \end{pmatrix}. \tag{5.2}$$

The reflection matrix is defined as

$$\mathbf{M}_2(l) = \begin{pmatrix} 1 & 0 \\ -2/R\cos\theta & 1 \end{pmatrix}, \tag{5.3}$$

where the angle θ is between the incoming ray and the radial direction and R is the radius of the boundary at the bounce point. If the point $x = 0$ is over a circle the contribution of $M_2(\theta)$ can be split up into an incoming and outgoing portion. It is therefore useful to define

$$\sqrt{\mathbf{M}_2(l)} = \begin{pmatrix} 1 & 0 \\ -1/R\cos\theta & 1 \end{pmatrix}. \tag{5.4}$$

The quarter stadium monodromy matrices for the five orbits are given in table 5.1 for half the length of the full orbit. The monodromy matrices for the periodic orbit in the full stadium are calculated in a similar way. Vergini and Carlo [27] use a time reversal argument to find the monodromy matrix for the full orbit from the half orbit since if

$$\tilde{\mathbf{M}}(L/2) = \begin{pmatrix} a & b \\ c & d \end{pmatrix}, \tag{5.5}$$

Orbit	$\tilde{\mathbf{M}}(L/2)$
A	$\mathbf{M}_1(\sqrt{5})\sqrt{\mathbf{M}_2(\theta_a)}$
B	$\mathbf{M}_1(1+\sqrt{2})\sqrt{\mathbf{M}_2(0)}$
C	$\mathbf{M}_1(\sqrt{3})\sqrt{\mathbf{M}_2(\pi/6)}\mathbf{M}_1(\sqrt{3}/2)$
D	$\sqrt{\mathbf{M}_2(0)}\mathbf{M}_1(1+\sqrt{5})$
E	$\sqrt{\mathbf{M}_2(0)}\mathbf{M}_1(1+\sqrt{10})$

Table 5.1: The monodromy matrices for five short periodic orbits in the quarter stadium.

then the full monodromy matrix is given by

$$\tilde{\mathbf{M}}(L) = \begin{pmatrix} d & b \\ c & a \end{pmatrix} \begin{pmatrix} a & b \\ c & d \end{pmatrix}. \tag{5.6}$$

The wavenumber associated with each resonance is calculated using the Bohr-Sommerfeld quantization rule

$$k = (2n\pi + N_s\pi + \frac{\nu\pi}{2})/L, \tag{5.7}$$

where N_s denotes the number of times the orbit collides with the boundary, ν is the Maslov index and the length of the orbit is L.

Vergini and Carlo [27] have developed a method for evaluating the resonance fuunction and accounting for the phase around the orbit. The details will not be given here. The method is equivalent to evaluating

$$\Psi_m(x,y) = \frac{c_m}{\sqrt{Q(x)}} \exp\left(\mathrm{i}kx + \frac{\mathrm{i}}{2}\frac{P(x)}{Q(x)}ky^2\right), \tag{5.8}$$

on each leg of the periodic orbit and adding these contributions over the enclosure.

5.3.3 Combining resonances

The resonance functions have now been calculated, but these resonance functions need to be combined to form the semiclassical approximations to the modes that are

required.

An appropriate basis of resonance functions is chosen so that the semiclassical approximations to the odd-odd modes can be found. Not all of the resonance functions are required to find the modes of the system. A basis of resonance functions is chosen by noting that there is a so called bouncing ball region of resonance functions that are connected with a ball bouncing between to top and bottom boundaries [57]. Vergini and Carlo [27] choose the bouncing ball resonances (M,N) so that they have the lowest error σ of the possible candidates. The Weyl formula

$$\overline{N}(k) \approx \frac{(4+\pi)k^2-(16+2\pi)k}{16\pi}+\frac{1}{4}, \tag{5.9}$$

approximates the number of resonance functions that are required in addition to the bouncing ball resonances. Orbit C is used first after the bouncing ball orbits because it has the lowest error of the first three orbits, then orbit A is used then orbit B. This means that the density of resonances agrees with the semiclassical mean density. Note for $k > 15$ more periodic orbits are needed than the five given here.

5.3.4 Calculating modes

Vergini and Carlo [27] approximate the modes by using a linear combination of resonance functions in the basis calculated above. Let the resonances selected be consecutive in energy $\psi_{\Gamma_1}, \psi_{\Gamma_1}, ..., \psi_{\Gamma_N}$, where $N > N_r$. The linear combination required is given by the generalized eigenvalue problem

$$[\mathbf{A}-\kappa^2\mathbf{B}]\boldsymbol{\xi} = 0, \tag{5.10}$$

where

$$A_{ij} = \int_{\mathscr{D}} \psi_i^*(-\nabla^2\psi_j)\,\mathrm{d}\mathbf{r}, \tag{5.11}$$

and

$$B_{ij} = \int_{\mathscr{D}} \psi_i^* \psi_j \, \mathrm{d}\mathbf{r}. \tag{5.12}$$

The proportions of each resonance to be combined to get the mode shape function is given by $\boldsymbol{\xi}$.

5.3.5 Dirichlet boundary conditions

The results of using SPOT in the quarter stadium with Dirichlet boundary conditions are summarized in figure 5.2. The top plot shows the unfolded mode count, where '$\times$' denotes the FEM mode wavenumber and 'o' denotes the SPOT approximation. The SPOT approximations match up with the FEM results very well. The next plot shows the normalized error, which is the unfolded FEM wavenumber minus the SPOT unfolded wavenumber. This again shows the agreement is very good. The error is much less than the average space between two mode wavenumbers. The bottom plot shows the overlap between the FEM and SPOT mode shapes. The overlap is the square root of the MAC between the FEM and SPOT mode shapes. The overlap is well over 90% for all the mode shapes apart from mode 20. Mode 20 would be much better approximated if the next few resonance functions were also included. Vergini and Carlo [27] approximate the first 25 mode shapes using the first 27 resonance functions. The results show that the 20th mode is actually well approximated in that case.

Figure 5.3 shows the resonance functions used to construct the SPOT mode shape approximations. Figure 5.4 shows which resonance functions have contributed to each mode shape approximation. The darker the grey the greater the contribution. Some modes, for example mode 6, are mostly constructed from one resonance function other modes, for example mode 11, are a combination of several resonance functions. Figure 5.5 shows the SPOT mode shape approximations and figure 5.6 shows the FEM mode shapes. The agreement between the SPOT and FEM mode

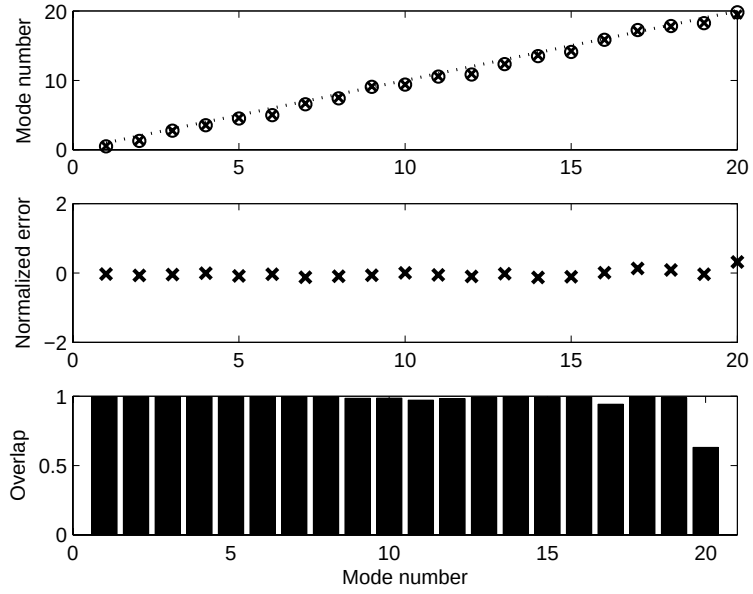

Figure 5.2: SPOT results for quarter stadium with Dirichlet boundary conditions. The top plot show the unfolded mode count with '$\times$' denoting the FEM mode wavenumbers and 'o' showing the SPOT approximation. The dotted line shows the approximation to the average mode count. The middle plot shows the normalized error and the bottom plot show the overlaps.

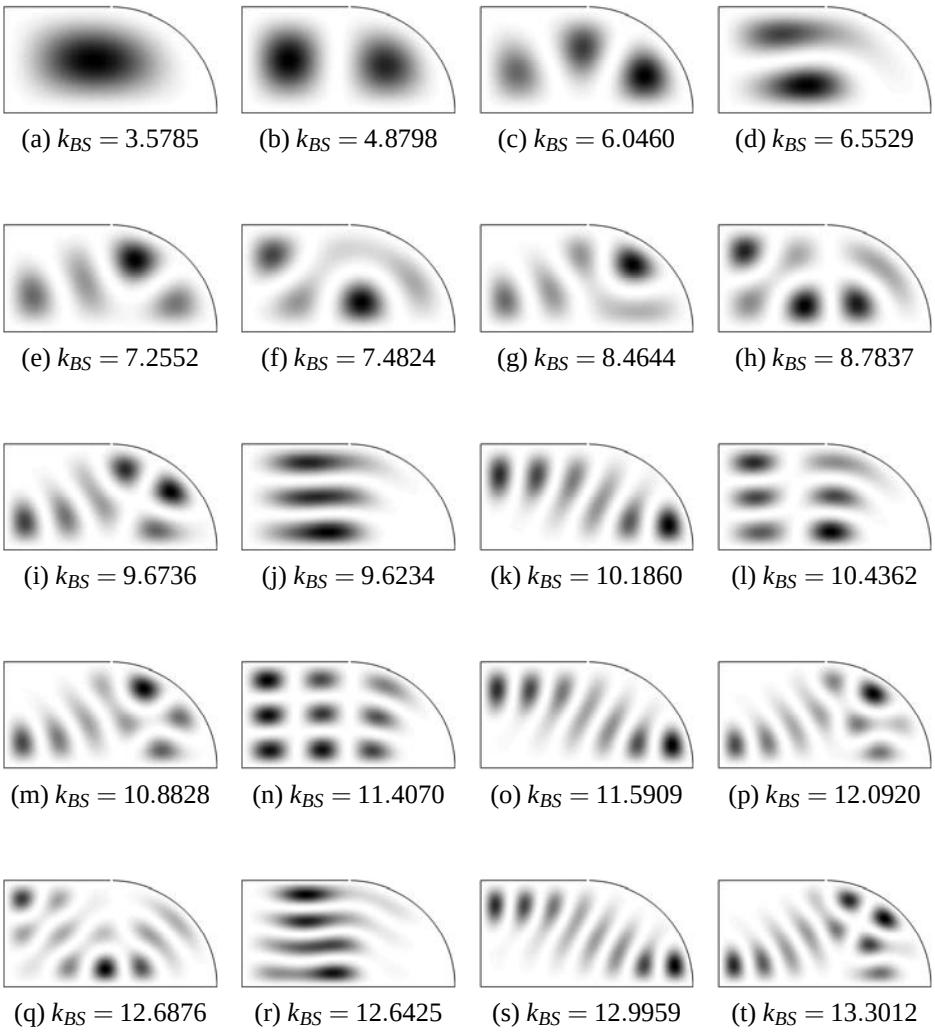

(a) $k_{BS} = 3.5785$ (b) $k_{BS} = 4.8798$ (c) $k_{BS} = 6.0460$ (d) $k_{BS} = 6.5529$

(e) $k_{BS} = 7.2552$ (f) $k_{BS} = 7.4824$ (g) $k_{BS} = 8.4644$ (h) $k_{BS} = 8.7837$

(i) $k_{BS} = 9.6736$ (j) $k_{BS} = 9.6234$ (k) $k_{BS} = 10.1860$ (l) $k_{BS} = 10.4362$

(m) $k_{BS} = 10.8828$ (n) $k_{BS} = 11.4070$ (o) $k_{BS} = 11.5909$ (p) $k_{BS} = 12.0920$

(q) $k_{BS} = 12.6876$ (r) $k_{BS} = 12.6425$ (s) $k_{BS} = 12.9959$ (t) $k_{BS} = 13.3012$

Figure 5.3: First 20 resonance functions of the quarter stadium with Dirichlet boundary conditions. Bohr-Sommerfeld quantization number is shown below.

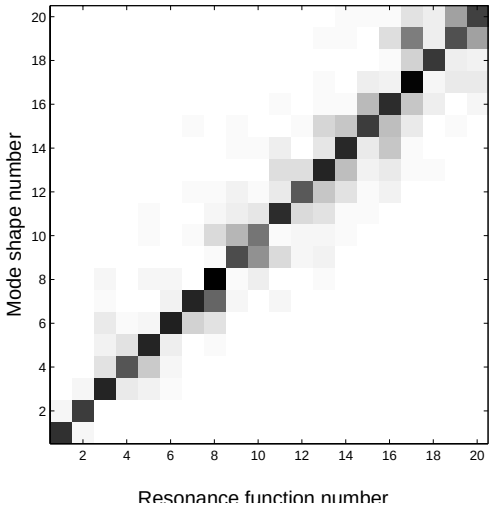

Figure 5.4: Contribution of resonance functions to each mode shape approximation. The darker the square the nearer the contribution is to one .

shapes is clearly seen.

(a) $\kappa = 3.5885$ overlap=0.9985 (b) $\kappa = 4.6798$ overlap=0.9985 (c) $\kappa = 6.0130$ overlap=0.9989 (d) $\kappa = 6.6121$ overlap=0.9984

(e) $\kappa = 7.2452$ overlap=0.9971 (f) $\kappa = 7.5481$ overlap=0.9992 (g) $\kappa = 8.3990$ overlap=0.9955 (h) $\kappa = 8.8340$ overlap=0.9953

(i) $\kappa = 9.5896$ overlap=0.9846 (j) $\kappa = 9.7320$ overlap=0.9853 (k) $\kappa = 10.2178$ overlap=0.9718 (l) $\kappa = 10.3326$ overlap=0.9825

(m) $\kappa = 10.9154$ overlap=0.9902 (n) $\kappa = 11.3387$ overlap=0.9975 (o) $\kappa = 11.5587$ overlap=0.9913 (p) $\kappa = 12.1627$ overlap=0.9938

(q) $\kappa = 12.6121$ overlap=0.9924 (r) $\kappa = 12.8035$ overlap=0.9985 (s) $\kappa = 12.9264$ overlap=0.9889 (t) $\kappa = 13.4011$ overlap=0.6302

Figure 5.5: First 20 mode shape approximations using SPOT in the quarter stadium with Dirichlet boundary conditions. Mode wavenumber shown below.

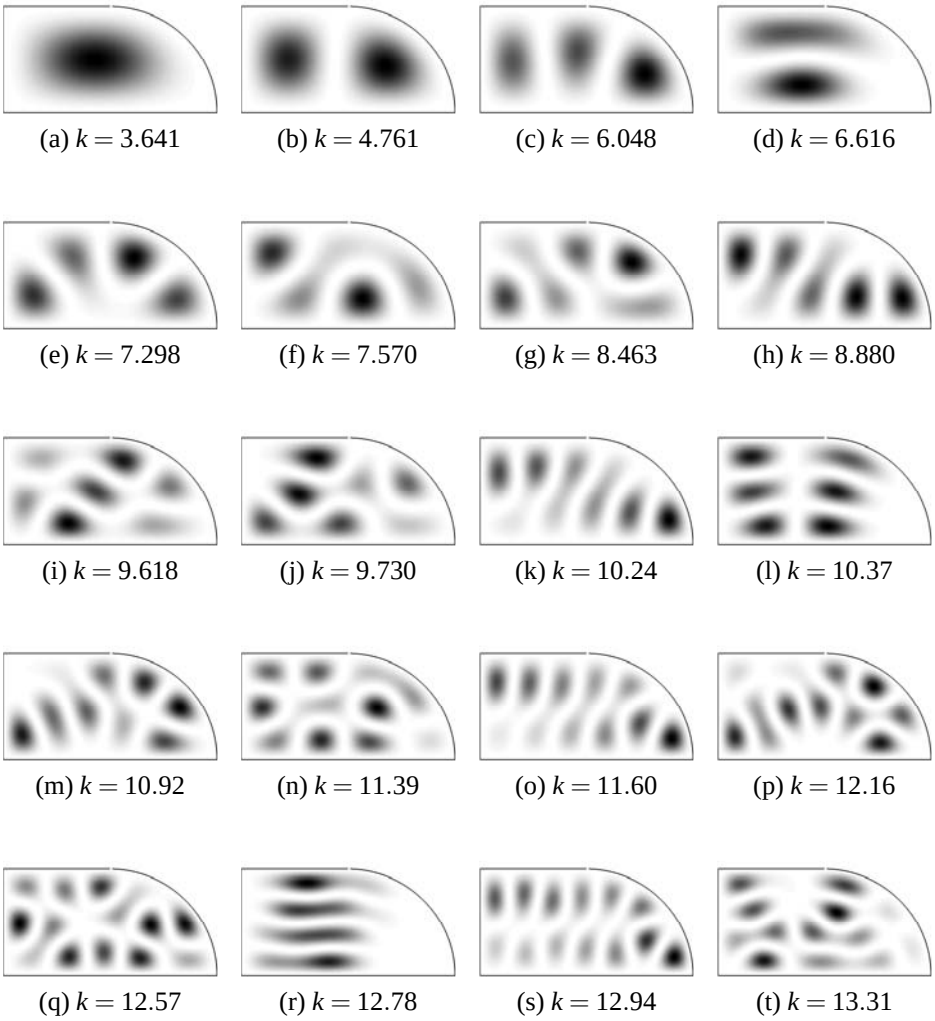

(a) $k = 3.641$ (b) $k = 4.761$ (c) $k = 6.048$ (d) $k = 6.616$

(e) $k = 7.298$ (f) $k = 7.570$ (g) $k = 8.463$ (h) $k = 8.880$

(i) $k = 9.618$ (j) $k = 9.730$ (k) $k = 10.24$ (l) $k = 10.37$

(m) $k = 10.92$ (n) $k = 11.39$ (o) $k = 11.60$ (p) $k = 12.16$

(q) $k = 12.57$ (r) $k = 12.78$ (s) $k = 12.94$ (t) $k = 13.31$

Figure 5.6: First 20 numerically approximated mode shapes in the quarter stadium with Dirichlet boundary conditions. Mode wavenumber is shown below.

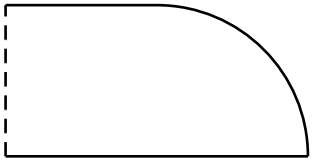

Figure 5.7: Quarter stadium with Neumann boundary condition (dashed line) on one side and Dirichlet boundary condition on the other sides.

5.3.6 Neumann boundary conditions

SPOT can be used to calculate the modes with a Neumann boundary condition on one side of the quarter stadium and Dirichlet on the other sides, see figure 5.7. The periodic orbits used are exactly the same. The monodromy matrix for each of the orbits is also exactly the same. The Bohr-Sommerfeld quantization rule will change because bounces at a Neumann boundary condition do not contribute to a phase change.

The results for the quarter stadium with a Neumann boundary condition on one boundary edge and Dirichlet on the others are summarized in figure 5.8. Close agreement, as in the Dirichlet boundary condition case, is seen for both the wavenumber and overlap between the FEM and SPOT mode shapes. All the overlaps are over 90%.

Figure 5.9 shows the resonance functions used for the SPOT approximations. Figure 5.10 shows that SPOT mode shape approximations and figure 5.11 show the FEM mode shapes. Again good agreement is seen between the mode shapes.

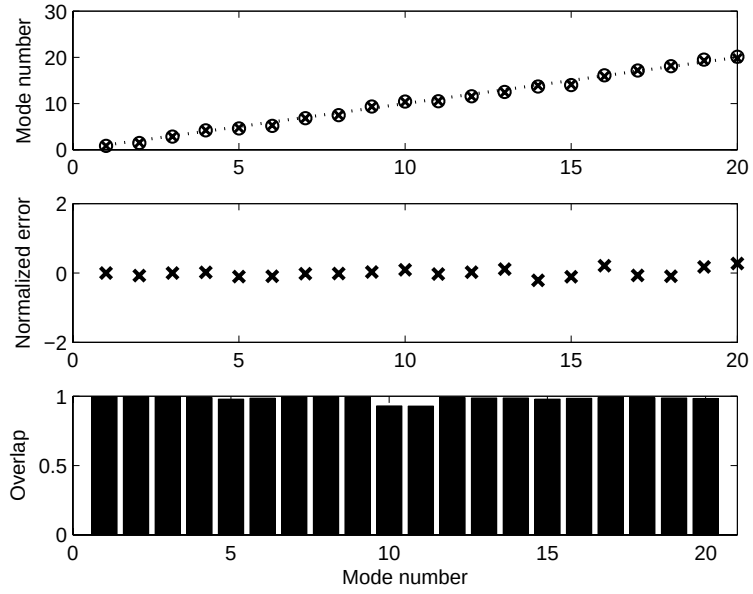

Figure 5.8: SPOT results for quarter stadium with Dirichlet and Neumann boundary conditions. The top plot show the unfolded mode count with '$\times$' denoting the FEM mode wavenumbers and 'o' showing the SPOT approximation. The dotted line shows the approximation to the average mode count. The middle plot shows the normalized error and the bottom plot shows the overlaps.

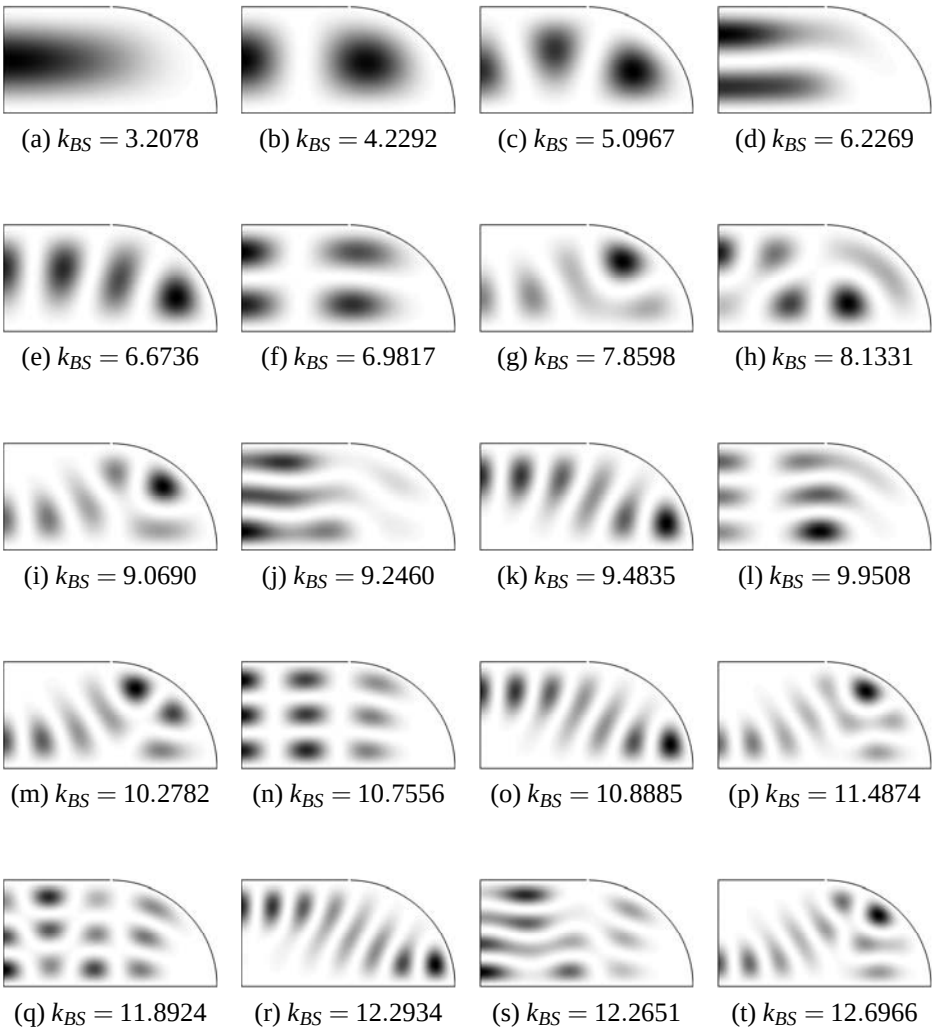

(a) $k_{BS} = 3.2078$ (b) $k_{BS} = 4.2292$ (c) $k_{BS} = 5.0967$ (d) $k_{BS} = 6.2269$

(e) $k_{BS} = 6.6736$ (f) $k_{BS} = 6.9817$ (g) $k_{BS} = 7.8598$ (h) $k_{BS} = 8.1331$

(i) $k_{BS} = 9.0690$ (j) $k_{BS} = 9.2460$ (k) $k_{BS} = 9.4835$ (l) $k_{BS} = 9.9508$

(m) $k_{BS} = 10.2782$ (n) $k_{BS} = 10.7556$ (o) $k_{BS} = 10.8885$ (p) $k_{BS} = 11.4874$

(q) $k_{BS} = 11.8924$ (r) $k_{BS} = 12.2934$ (s) $k_{BS} = 12.2651$ (t) $k_{BS} = 12.6966$

Figure 5.9: First 20 resonance functions of the quarter stadium with Neumann boundary condition on one boundary. Bohr-Sommerfeld quantization number is shown below.

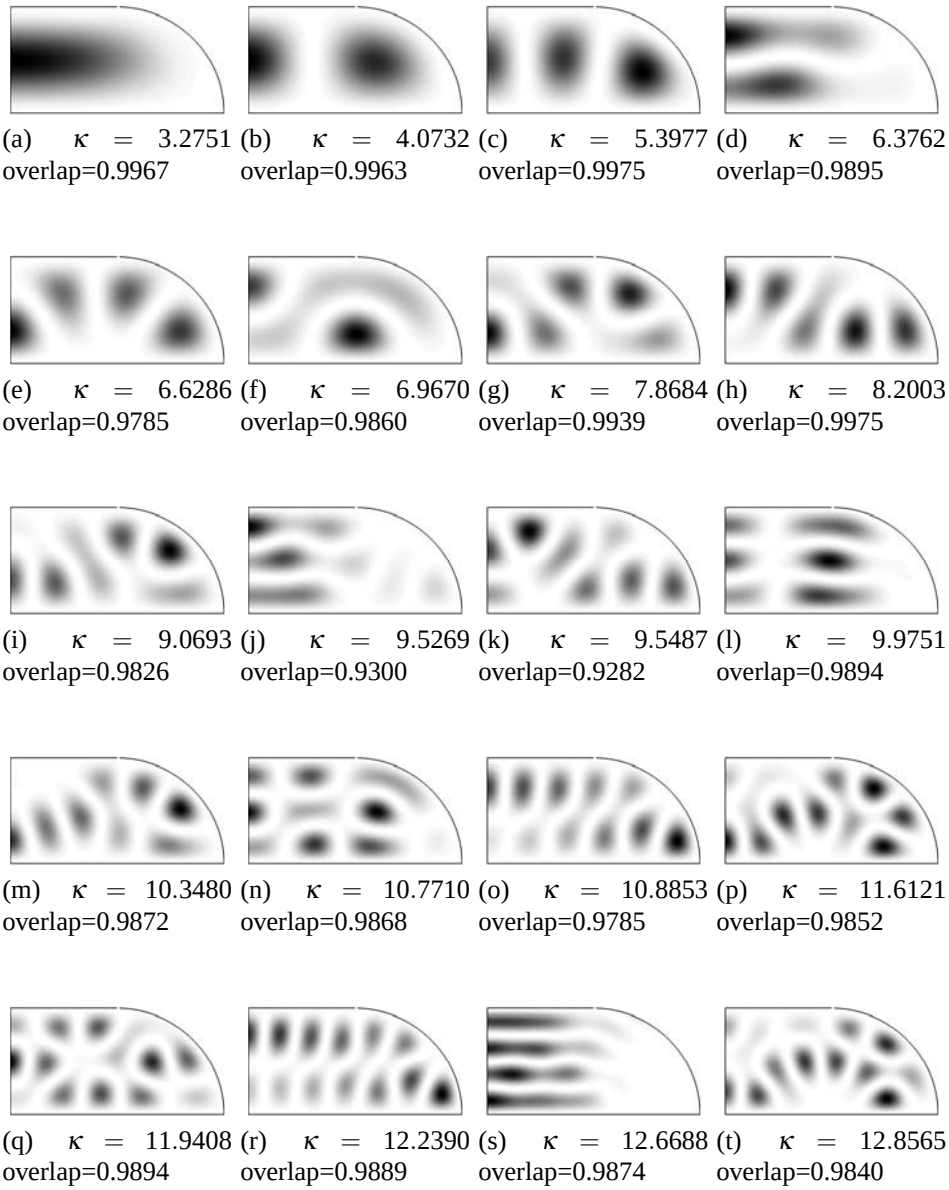

Figure 5.10: First 20 mode shape approximations using SPOT in the quarter stadium with Neumann boundary condition on one boundary. Mode wavenumber shown below.

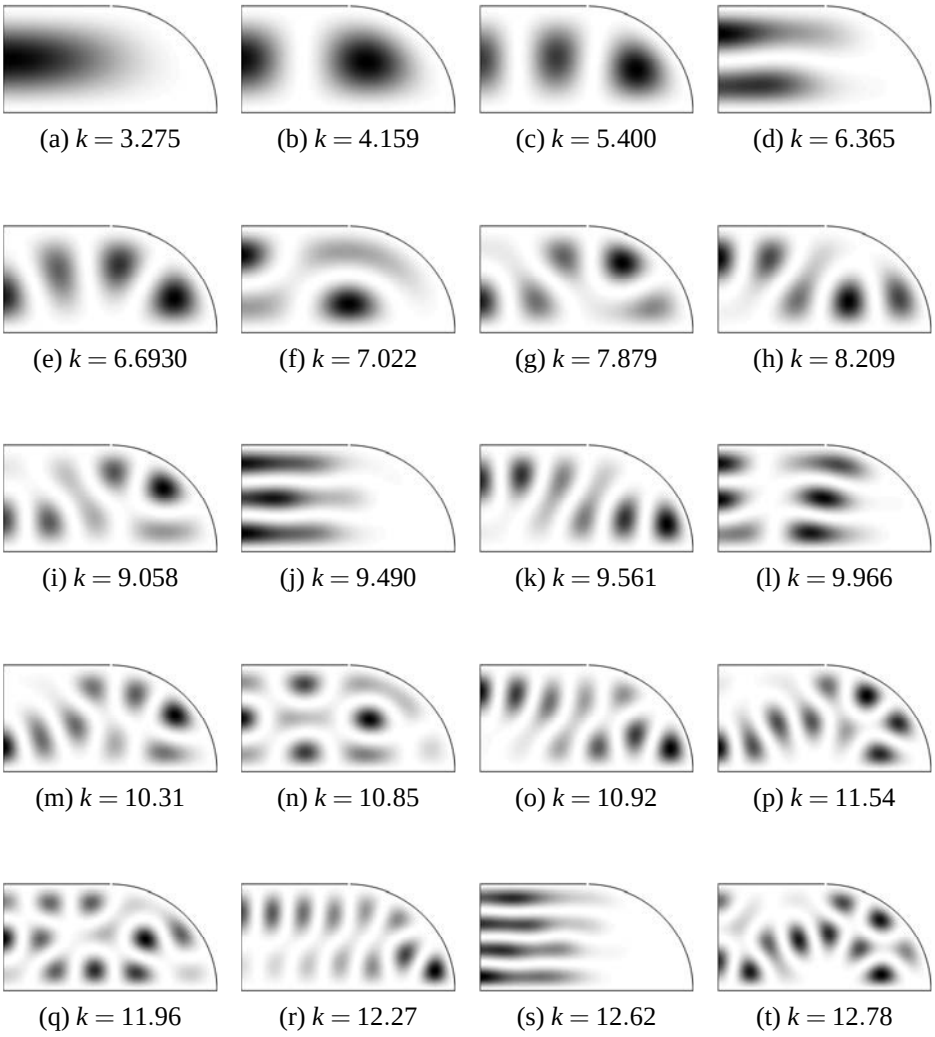

(a) $k = 3.275$ (b) $k = 4.159$ (c) $k = 5.400$ (d) $k = 6.365$

(e) $k = 6.6930$ (f) $k = 7.022$ (g) $k = 7.879$ (h) $k = 8.209$

(i) $k = 9.058$ (j) $k = 9.490$ (k) $k = 9.561$ (l) $k = 9.966$

(m) $k = 10.31$ (n) $k = 10.85$ (o) $k = 10.92$ (p) $k = 11.54$

(q) $k = 11.96$ (r) $k = 12.27$ (s) $k = 12.62$ (t) $k = 12.78$

Figure 5.11: First 20 numerically approximated mode shapes in the quarter stadium with Neumann boundary condition on one boundary. Mode wavenumber shown below.

5.4 Quadrupole enclosure

The boundary of the quadrupole enclosure is given by

$$r(\phi) = R(1 + \varepsilon \cos 2\phi), \tag{5.13}$$

where ϕ is the angle at the centre, ε is the shape constant and R is a constant. Tureci *et al* [30] approximate a stable mode shape in a quadrupole using SPOT. Tureci *et al* [30] take $\varepsilon = 0.17$ in their calculations and that will be the value used in the rest of this thesis. The name quadrupole may be slightly confusing, since in the acoustics literature it generally refers to a type of source. The use of quadrupole here will refer to the quadrupole enclosure. The quadrupole enclosure has mixed ray dynamics. The mode shapes of an enclosure with mixed phase space have not previously been calculated using SPOT.

The mode shapes for the quadrupole will be approximated for three different boundary conditions; Dirichlet, Neumann and impedance. This will be the first time that SPOT has been used to approximate the mode shapes of an enclosure with completely Neumann or impedance boundary conditions. The SPOT approximations will be compared against numerically approximated mode shapes.

5.4.1 Short periodic orbits

The short periodic orbits used here have been found by inspection or have been found in other work (Tureci *et al* [30]). However, the techniques mentioned above, such as inspection of the Poincaré section for stable periodic orbits, could have been used.

There are two bouncing ball orbits, see figure 5.12(a) and (b). There are the whispering gallery orbits that do not cross themselves, see figure 5.12(c) and (d). There are infinitely many of these orbits because the number of bounces against the boundary can always be increased by one. However the length of these orbits is limited by the length of the boundary. Finally, there are orbits that do cross themselves, such as

the bow tie, again there are an infinite number of these orbits. Bouncing ball orbit 1 and the bow tie orbit are both stable. The other periodic orbits shown are unstable.

5.4.2 Resonance functions

The resonance functions for the stable orbits are calculated using the same code as for the quarter stadium, but the starting values for P and Q are calculated from the eigenvector of the monodromy matrix. Tureci *et al* [30] previously calculated a high frequency mode approximation for the bow tie orbit in the quadrupole billiard. The resonance functions for the unstable orbits can be calculated using the work of Vergini. These have not previously been calculated.

5.4.3 Mode shape approximations

The error of the resonances is required to calculate the mode shape approximations. The semiclassical approximation for the error can be used or the error can be numerically approximated. The semiclassical error has been used here.

5.4.4 Dirichlet boundary conditions

Figure 5.13 summarizes the SPOT results for the quadrupole enclosure with Dirichlet boundary conditions. The top plot shows the unfolded mode count. It shows that the mode wavenumbers are well approximated by SPOT although the normalized error is slightly larger than for the quarter stadium case. The overlaps are all above 90% which indicates that the SPOT and FEM mode shapes are closely correlated.

Figure 5.14 shows the resonance functions used in the construction of the SPOT approximations. Note that only four periodic orbits were required to approximate the first 20 mode shapes. Figure 5.15 shows the SPOT approximations and figure 5.16 show the FEM mode shapes.

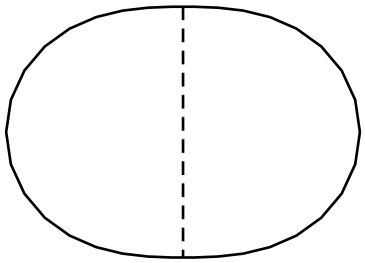

(a) Bouncing ball orbit 1

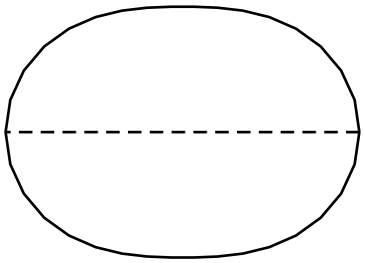

(b) Bouncing ball orbit 2

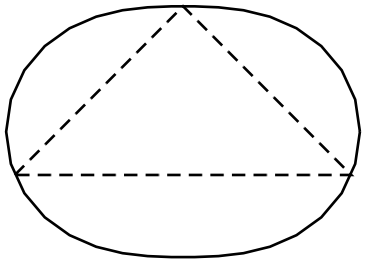

(c) Triangle orbit

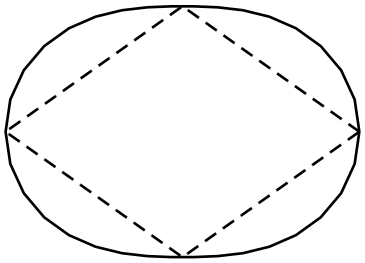

(d) Diamond orbit

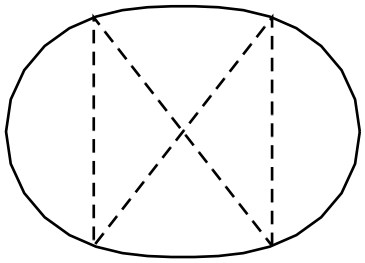

(e) Bow tie orbit

Figure 5.12: Short periodic orbits of the quadrupole enclosure.

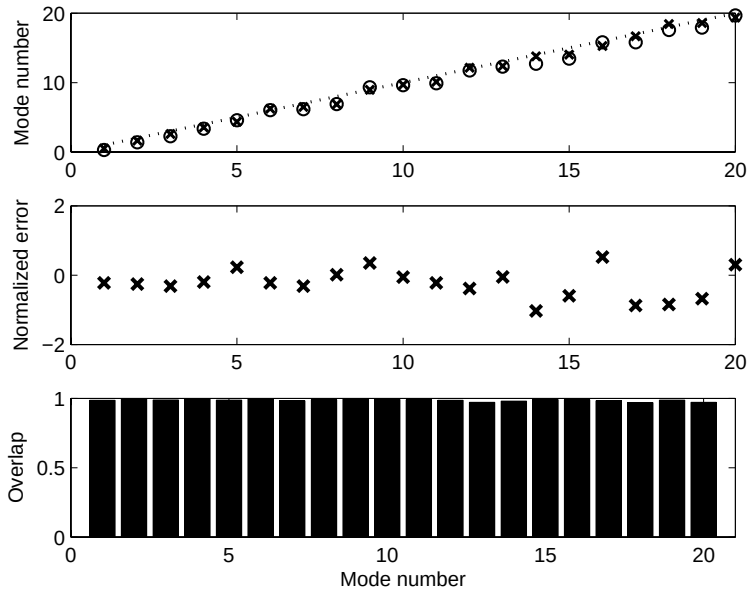

Figure 5.13: SPOT results for quadrupole enclosure with Dirichlet boundary conditions. The top plot show the unfolded mode count with '$\times$' denoting the FEM mode wavenumbers and 'o' showing the SPOT approximation. The middle plot shows the normalized error and the bottom plot shows the overlaps.

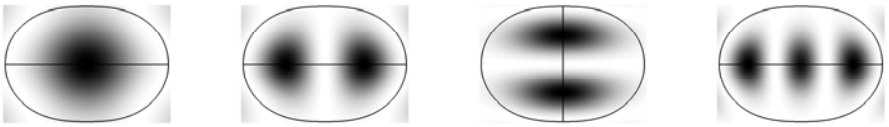

(a) $k_{BS} = 2.0138$ (b) $k_{BS} = 3.3564$ (c) $k_{BS} = 4.0495$ (d) $k_{BS} = 4.6990$

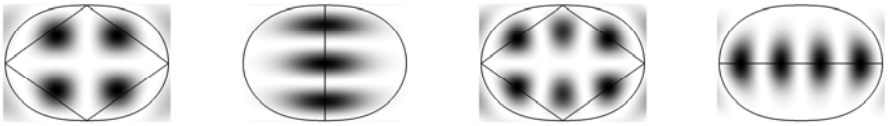

(e) $k_{BS} = 4.9275$ (f) $k_{BS} = 5.9421$ (g) $k_{BS} = 6.0226$ (h) $k_{BS} = 6.0415$

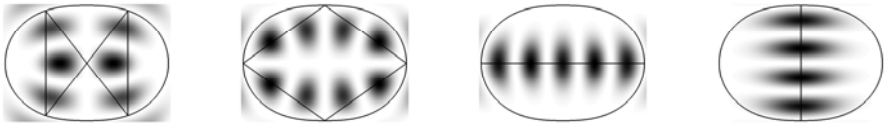

(i) $k_{BS} = 7.0865$ (j) $k_{BS} = 7.1176$ (k) $k_{BS} = 7.3841$ (l) $k_{BS} = 7.8346$

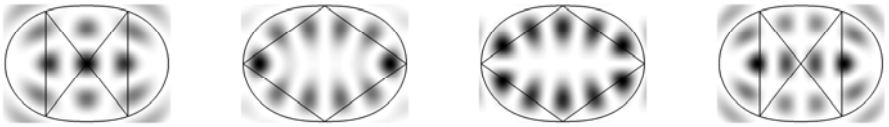

(m) $k_{BS} = 8.0027$ (n) $k_{BS} = 8.2126$ (o) $k_{BS} = 8.2126$ (p) $k_{BS} = 8.9188$

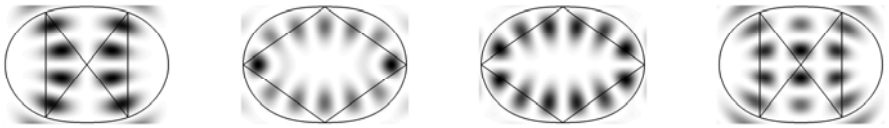

(q) $k_{BS} = 8.9188$ (r) $k_{BS} = 9.3076$ (s) $k_{BS} = 9.3076$ (t) $k_{BS} = 9.8350$

Figure 5.14: First 20 resonances functions in the quadrupole enclosure with Dirichlet boundary conditions. Bohr-Sommerfeld quantization number is shown below.

(a) $\kappa = 2.1072$ overlap=0.9865 (b) $\kappa = 3.3560$ overlap=0.9966 (c) $\kappa = 4.0240$ overlap=0.9879 (d) $\kappa = 4.6609$ overlap=0.9981

(e) $\kappa = 5.2761$ overlap=0.9869 (f) $\kappa = 5.9006$ overlap=0.9990 (g) $\kappa = 5.9529$ overlap=0.9826 (h) $\kappa = 6.2431$ overlap=0.9890

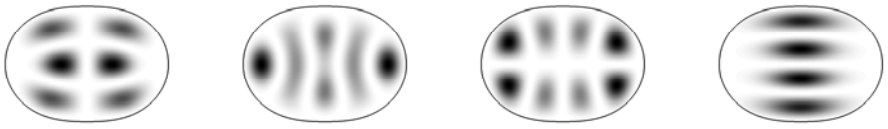

(i) $\kappa = 7.0881$ overlap=0.9945 (j) $\kappa = 7.1889$ overlap=0.9926 (k) $\kappa = 7.2736$ overlap=0.9894 (l) $\kappa = 7.8349$ overlap=0.9855

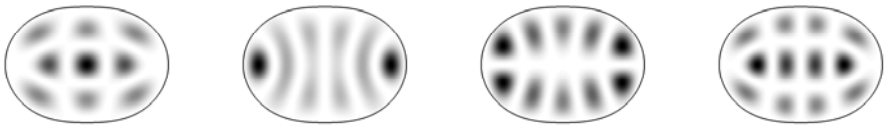

(m) $\kappa = 7.9997$ overlap=0.9718 (n) $\kappa = 8.1175$ overlap=0.9803 (o) $\kappa = 8.3093$ overlap=0.9912 (p) $\kappa = 8.9213$ overlap=0.9900

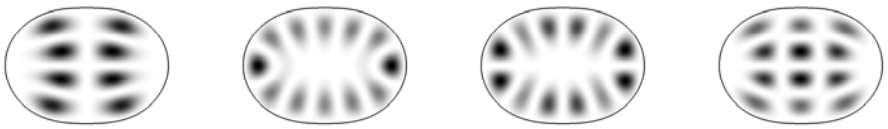

(q) $\kappa = 8.9225$ overlap=0.9823 (r) $\kappa = 9.3593$ overlap=0.9685 (s) $\kappa = 9.4348$ overlap=0.9876 (t) $\kappa = 9.8404$ overlap=0.9714

Figure 5.15: First 20 mode approximations in the quadrupole enclosure with Dirichlet boundary conditions. Mode wavenumber shown below.

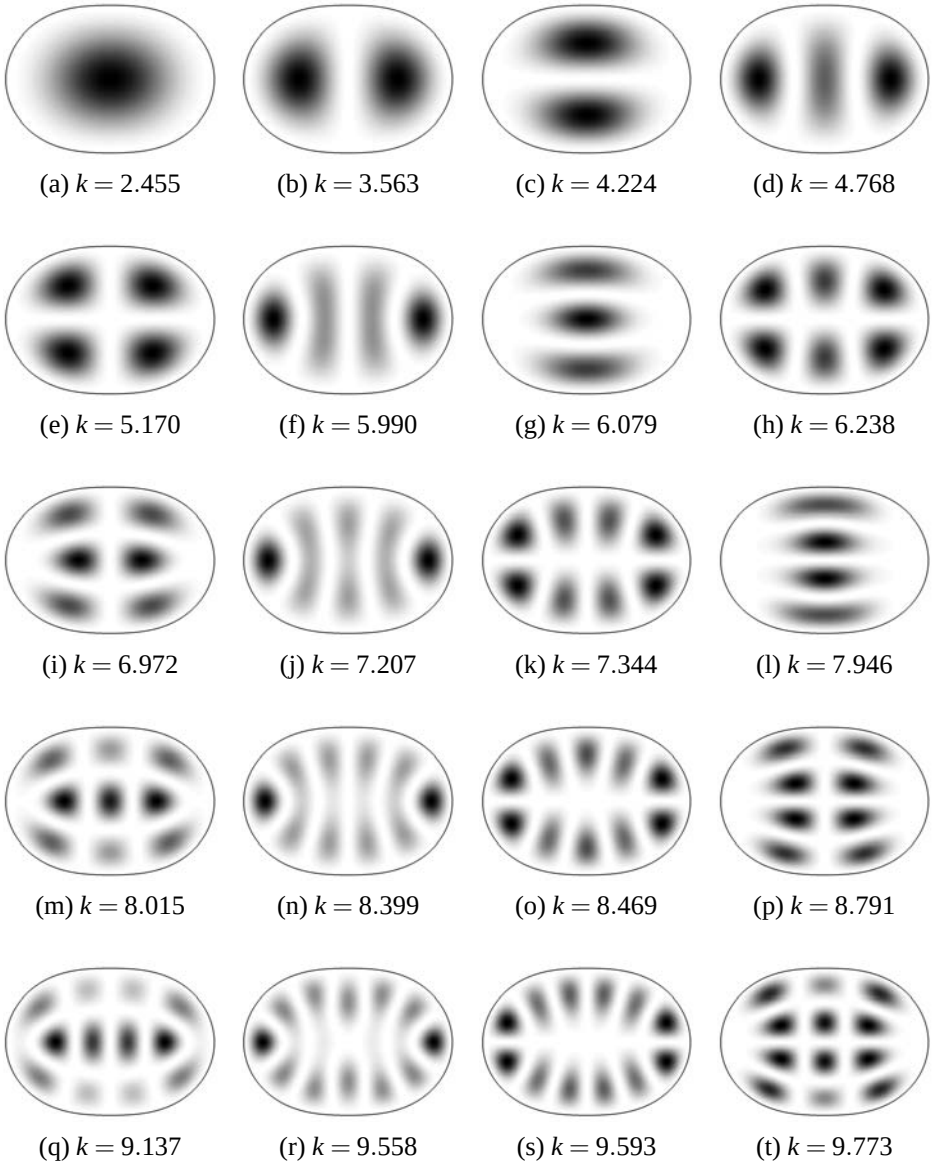

(a) $k = 2.455$ (b) $k = 3.563$ (c) $k = 4.224$ (d) $k = 4.768$

(e) $k = 5.170$ (f) $k = 5.990$ (g) $k = 6.079$ (h) $k = 6.238$

(i) $k = 6.972$ (j) $k = 7.207$ (k) $k = 7.344$ (l) $k = 7.946$

(m) $k = 8.015$ (n) $k = 8.399$ (o) $k = 8.469$ (p) $k = 8.791$

(q) $k = 9.137$ (r) $k = 9.558$ (s) $k = 9.593$ (t) $k = 9.773$

Figure 5.16: First 20 numerically approximated mode shapes of the quadrupole with Dirichlet boundary conditions. Mode wavenumber shown below.

5.4.5 Neumann boundary conditions

The same process for the Dirichlet boundary conditions has been completed for the Neumann boundary conditions. An example using Neumann boundary conditions has not perviously been published. The periodic orbits are completely identical to the quadrupole with Dirichlet boundary conditions. However, a new basis of resonance functions is required because the Weyl formula depends on the boundary conditions.

Figure 5.17 summarizes the results of SPOT approximation for the quadrupole with Neumann boundary conditions. The top plot shows the unfolded wavenumbers and it shows they are generally well approximated. However, the approximation seems to be less good than for the Dirichlet case, especially for mode 18. Mode 18 might include contributions from the resonance functions not included in the basis, such as resonance function 21. If further resonance functions are included then the approximation may be improved. The overlaps are again all over 90% indicating that the SPOT approximations and the numerical approximations are well correlated.

Figure 5.18 shows the resonance functions used in the construction of the SPOT approximations. Notice that only three periodic orbits have been used here. The same basis from the Dirichlet case could not be used here because the mode count depends on the boundary conditions. Figure 5.19 shows the SPOT approximations and figure 5.20 show the FEM mode shapes. Notice that some of the mode shapes have been swapped.

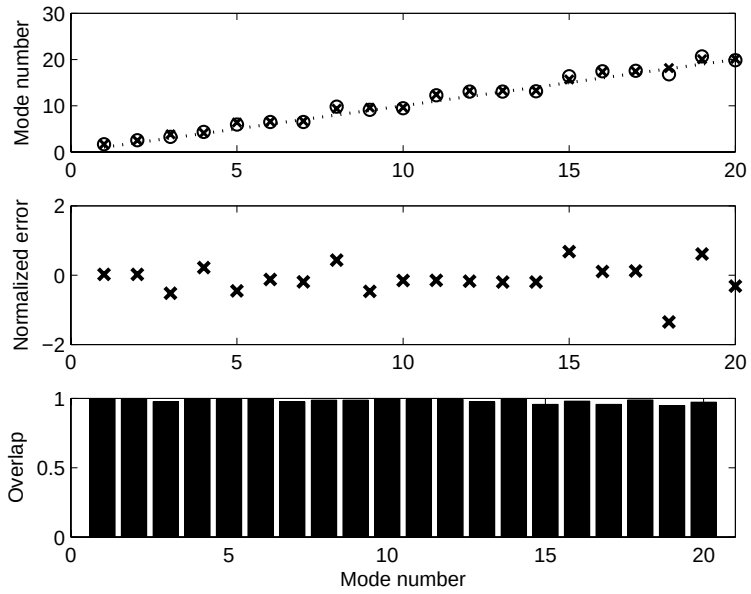

Figure 5.17: SPOT results for quadrupole with Neumann boundary conditions. The top plot show the unfolded mode count with '$\times$' denoting the FEM mode wavenumbers and 'o' showing the SPOT approximation. The middle plot shows the normalized error and the bottom plot shows the overlaps.

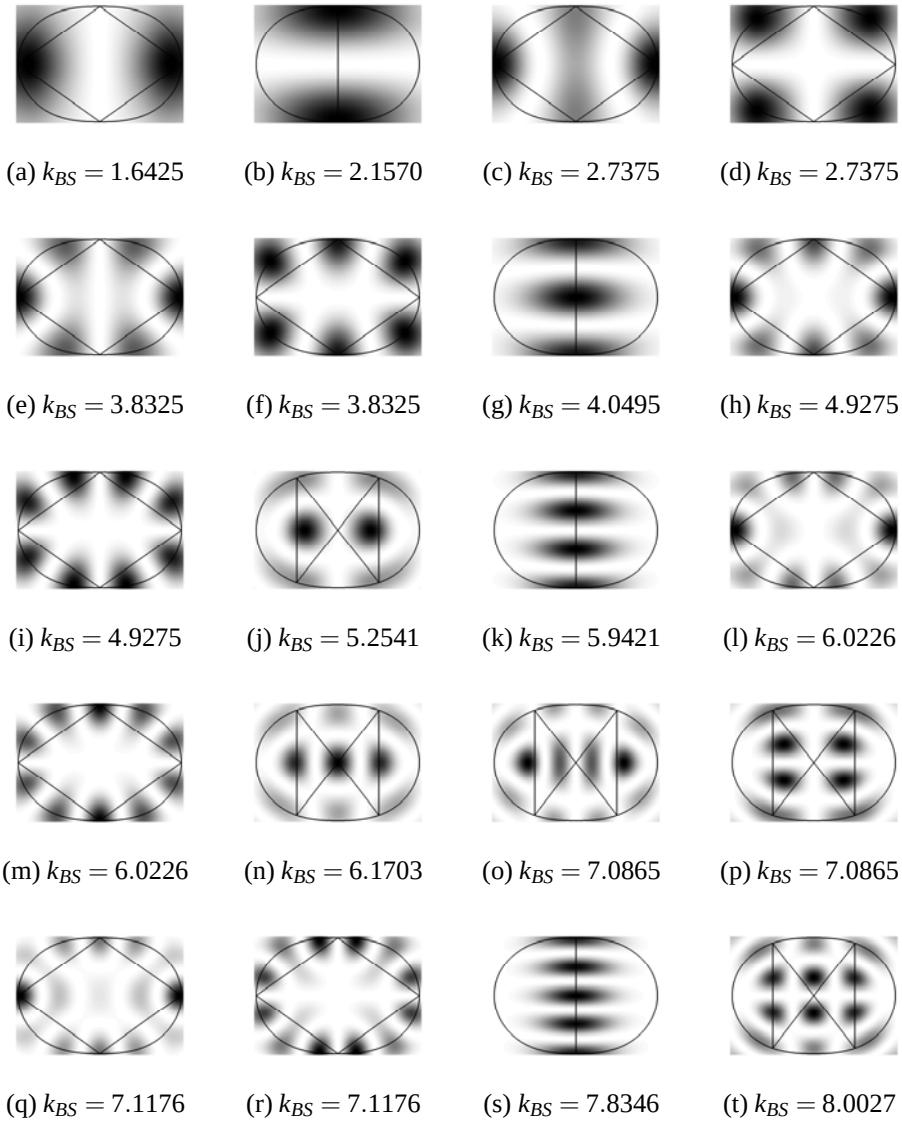

(a) $k_{BS} = 1.6425$ (b) $k_{BS} = 2.1570$ (c) $k_{BS} = 2.7375$ (d) $k_{BS} = 2.7375$

(e) $k_{BS} = 3.8325$ (f) $k_{BS} = 3.8325$ (g) $k_{BS} = 4.0495$ (h) $k_{BS} = 4.9275$

(i) $k_{BS} = 4.9275$ (j) $k_{BS} = 5.2541$ (k) $k_{BS} = 5.9421$ (l) $k_{BS} = 6.0226$

(m) $k_{BS} = 6.0226$ (n) $k_{BS} = 6.1703$ (o) $k_{BS} = 7.0865$ (p) $k_{BS} = 7.0865$

(q) $k_{BS} = 7.1176$ (r) $k_{BS} = 7.1176$ (s) $k_{BS} = 7.8346$ (t) $k_{BS} = 8.0027$

Figure 5.18: First 20 resonances functions in the quadrupole enclosure with Neumann boundary conditions. Bohr-Sommerfeld quantization number is shown below.

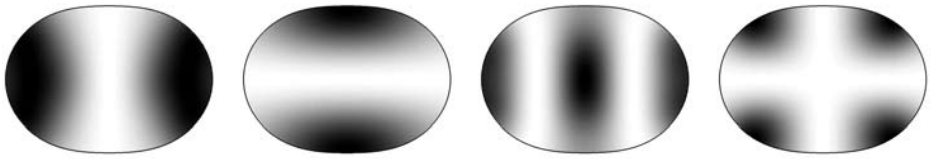

(a) $\kappa = 1.5756$ overlap=0.9954 (b) $\kappa = 2.1401$ overlap=0.9971 (c) $\kappa = 2.5842$ overlap=0.9760 (d) $\kappa = 3.1147$ overlap=0.9952

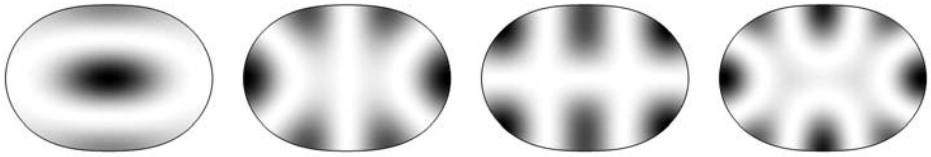

(e) $\kappa = 3.8328$ overlap=0.9920 (f) $\kappa = 4.0376$ overlap=0.9943 (g) $\kappa = 4.0485$ overlap=0.9748 (h) $\kappa = 4.9842$ overlap=0.9871

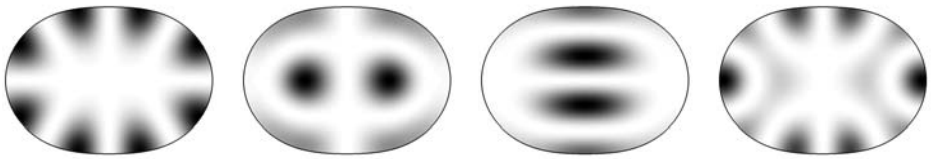

(i) $\kappa = 5.0970$ overlap=0.9873 (j) $\kappa = 5.2128$ overlap=0.9956 (k) $\kappa = 5.9510$ overlap=0.9909 (l) $\kappa = 6.1631$ overlap=0.9916

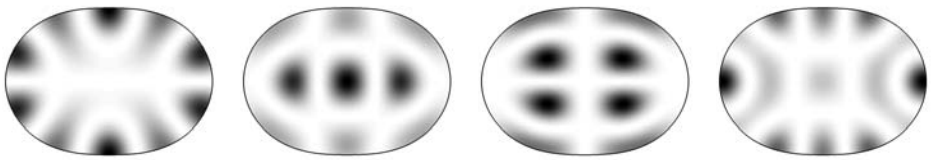

(m) $\kappa = 6.1699$ overlap=0.9747 (n) $\kappa = 6.1845$ overlap=0.9961 (o) $\kappa = 7.0313$ overlap=0.9565 (p) $\kappa = 7.1341$ overlap=0.9801

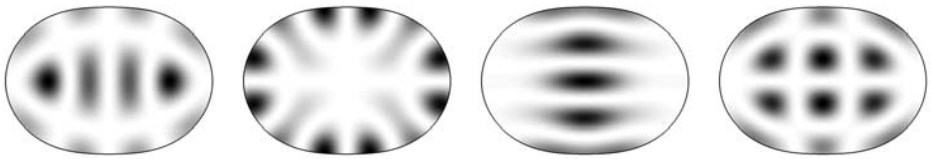

(q) $\kappa = 7.2932$ overlap=0.9562 (r) $\kappa = 7.3149$ overlap=0.9883 (s) $\kappa = 7.8394$ overlap=0.9479 (t) $\kappa = 8.0232$ overlap=0.9727

Figure 5.19: First 20 SPOT mode approximations in the quadrupole enclosure with Neumann boundary conditions. Mode wavenumber shown below.

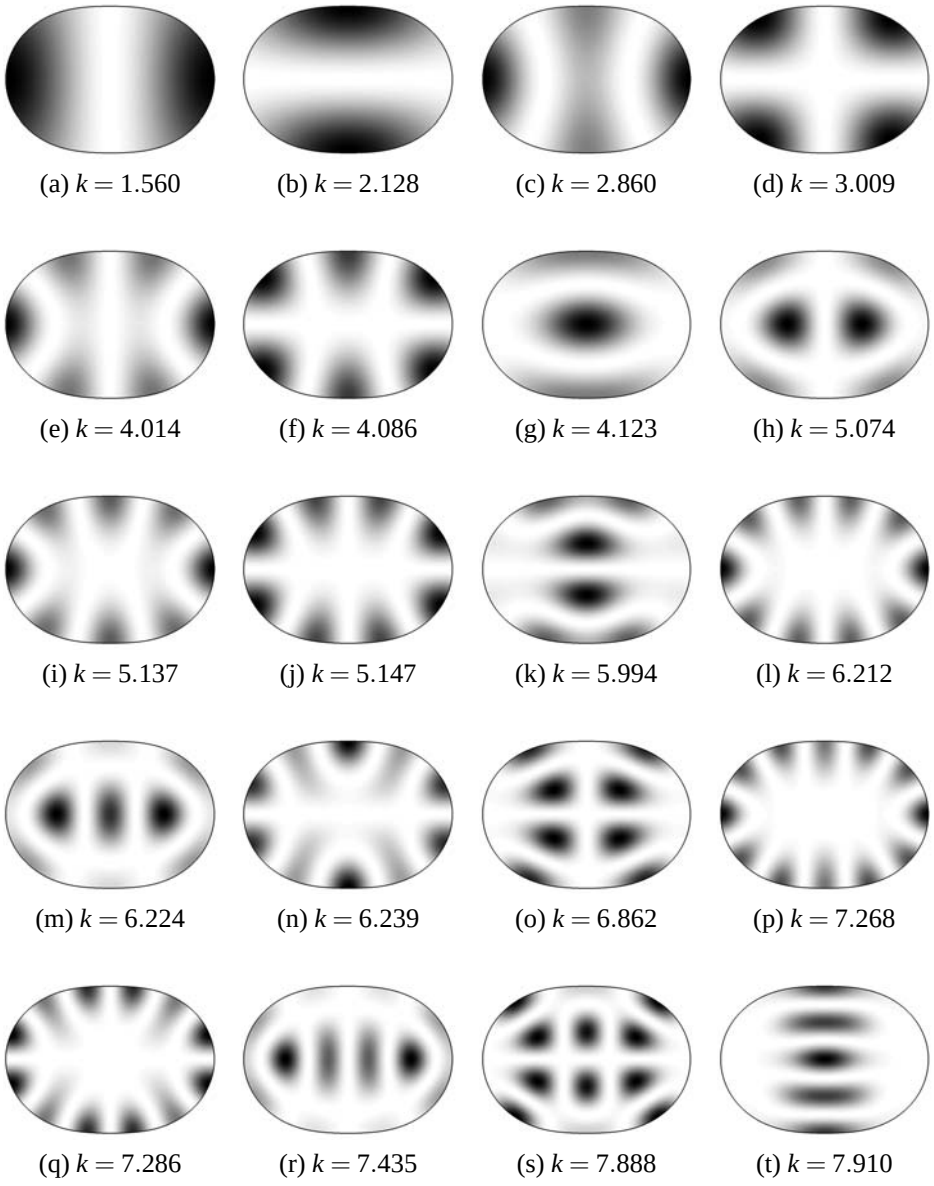

(a) $k = 1.560$ (b) $k = 2.128$ (c) $k = 2.860$ (d) $k = 3.009$

(e) $k = 4.014$ (f) $k = 4.086$ (g) $k = 4.123$ (h) $k = 5.074$

(i) $k = 5.137$ (j) $k = 5.147$ (k) $k = 5.994$ (l) $k = 6.212$

(m) $k = 6.224$ (n) $k = 6.239$ (o) $k = 6.862$ (p) $k = 7.268$

(q) $k = 7.286$ (r) $k = 7.435$ (s) $k = 7.888$ (t) $k = 7.910$

Figure 5.20: First 20 numerically approximated modes shapes of the quadrupole enclosure with Neumann boundary conditions. Mode wavenumber is shown below.

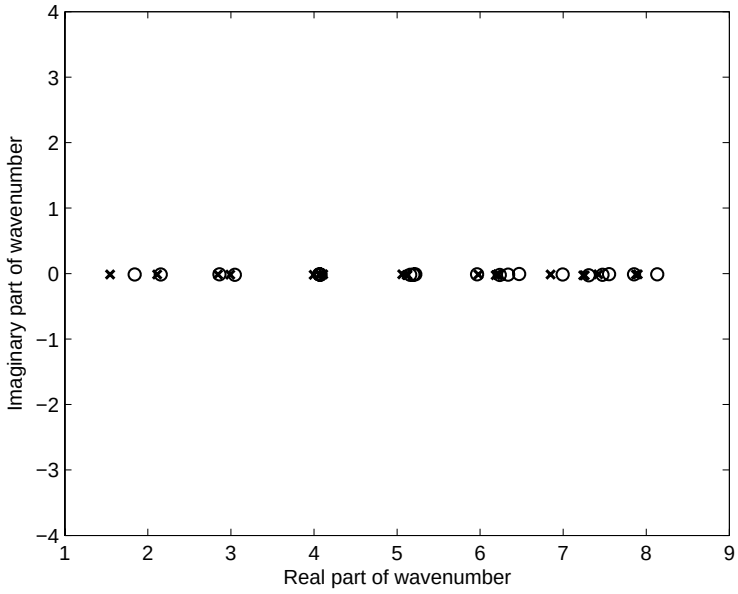

Figure 5.21: FEM mode wavenumbers ($\times$) and semiclassical approximations (o).

5.4.6 Impedance boundary conditions: Case 1

The theory for the impedance boundary condition was given in chapter 4. An example using impedance boundary conditions has not previously been published so in the first case a small value of impedance will be used, $A = 0.01 - 0.01\mathrm{i}$. This can be compared to the Neumann boundary condition case. The periodic orbits are completely identical to the quadrupole with Neumann boundary conditions.

Figure 5.21 shows the real and imaginary parts of the mode wavenumbers calculated using FEM ('$\times$') and calculated using SPOT ('o'). The SPOT approximations seem to provide accurate approximations to both the real and imaginary parts. Figure 5.22 (top) shows the absolute value of the difference between the SPOT and FEM mode wavenumbers. The absolute error is quite low compared to the spacing between the mode wavenumbers. Figure 5.22 (bottom) shows the overlap of the SPOT and the FEM mode shapes. These results are over 90% as seen in the Neumann boundary condition case.

Figure 5.23 shows the resonance functions used in the construction of the SPOT

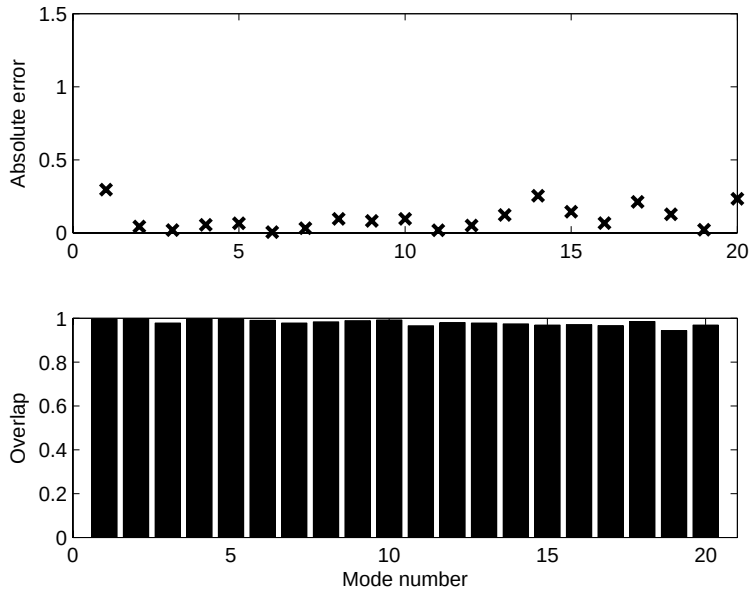

Figure 5.22: SPOT results for quadrupole enclosure with impedance boundary conditions. The top plot shows the absolute error between the SPOT approximation and the FEM mode wavenumber. The bottom plot shows the overlaps.

approximations. Notice that only three periodic orbits have been used here. Figure 5.24 shows the SPOT approximations and figure 5.25 show the FEM mode shapes. Notice that some of the mode shapes have been swapped.

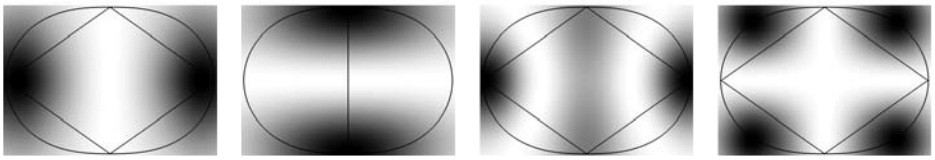

(a) $k_{BS} = 1.6219 - 0.0206i$ (b) $k_{BS} = 2.1450 - 0.0120i$ (c) $k_{BS} = 2.7169 - 0.0206i$ (d) $k_{BS} = 2.7169 - 0.0206i$

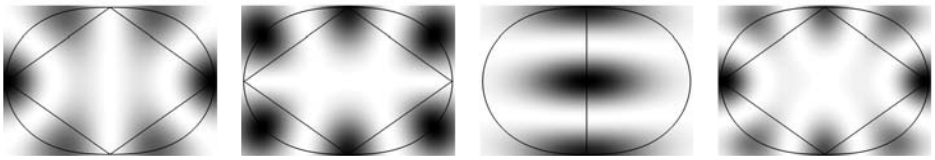

(e) $k_{BS} = 3.8119 - 0.0206i$ (f) $k_{BS} = 3.8119 - 0.0206i$ (g) $k_{BS} = 4.0375 - 0.0120i$ (h) $k_{BS} = 4.9069 - 0.0206i$

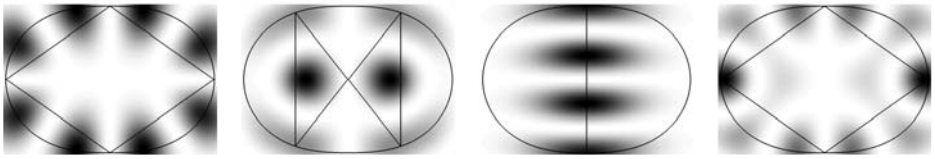

(i) $k_{BS} = 4.9069 - 0.0206i$ (j) $k_{BS} = 5.2419 - 0.0122i$ (k) $k_{BS} = 5.9300 - 0.0120i$ (l) $k_{BS} = 6.0020 - 0.0206i$

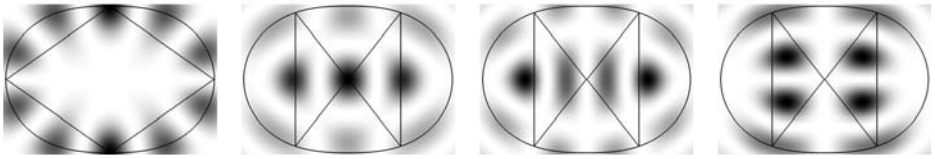

(m) $k_{BS} = 6.0020 - 0.0206i$ (n) $k_{BS} = 6.1581 - 0.0122i$ (o) $k_{BS} = 7.0743 - 0.0122i$ (p) $k_{BS} = 7.0743 - 0.0122i$

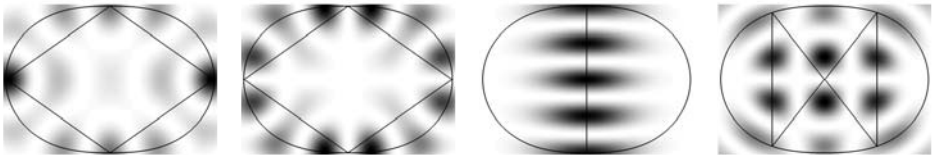

(q) $k_{BS} = 7.0970 - 0.0206i$ (r) $k_{BS} = 7.0970 - 0.0206i$ (s) $k_{BS} = 7.8225 - 0.0120i$ (t) $k_{BS} = 7.9905 - 0.0122i$

Figure 5.23: First 20 resonances functions in the quadrupole enclosure with impedance boundary conditions (case 1). Bohr-Sommerfeld quantization number shown below.

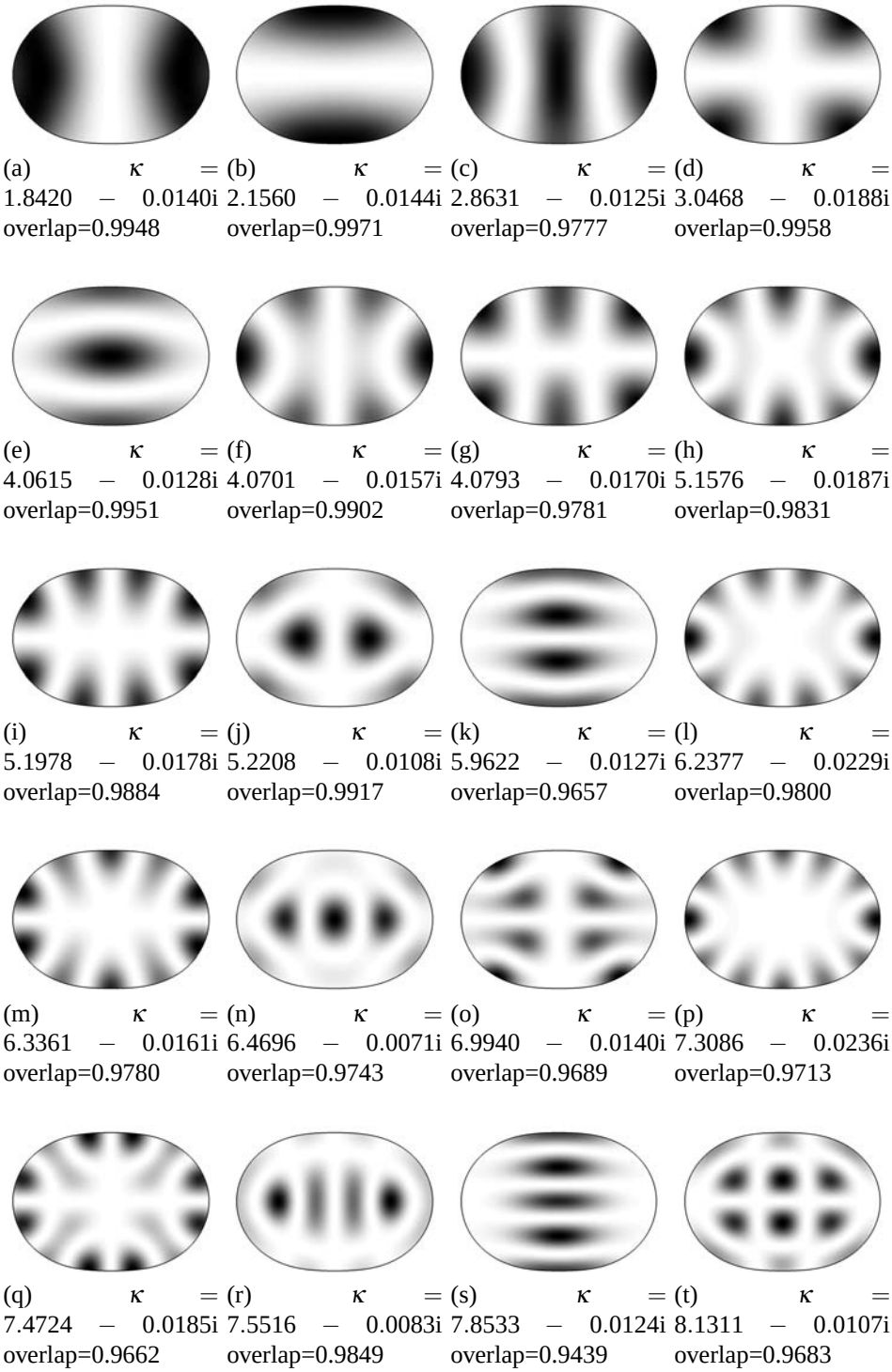

(a) $\kappa = 1.8420 - 0.0140i$ overlap=0.9948
(b) $\kappa = 2.1560 - 0.0144i$ overlap=0.9971
(c) $\kappa = 2.8631 - 0.0125i$ overlap=0.9777
(d) $\kappa = 3.0468 - 0.0188i$ overlap=0.9958
(e) $\kappa = 4.0615 - 0.0128i$ overlap=0.9951
(f) $\kappa = 4.0701 - 0.0157i$ overlap=0.9902
(g) $\kappa = 4.0793 - 0.0170i$ overlap=0.9781
(h) $\kappa = 5.1576 - 0.0187i$ overlap=0.9831
(i) $\kappa = 5.1978 - 0.0178i$ overlap=0.9884
(j) $\kappa = 5.2208 - 0.0108i$ overlap=0.9917
(k) $\kappa = 5.9622 - 0.0127i$ overlap=0.9657
(l) $\kappa = 6.2377 - 0.0229i$ overlap=0.9800
(m) $\kappa = 6.3361 - 0.0161i$ overlap=0.9780
(n) $\kappa = 6.4696 - 0.0071i$ overlap=0.9743
(o) $\kappa = 6.9940 - 0.0140i$ overlap=0.9689
(p) $\kappa = 7.3086 - 0.0236i$ overlap=0.9713
(q) $\kappa = 7.4724 - 0.0185i$ overlap=0.9662
(r) $\kappa = 7.5516 - 0.0083i$ overlap=0.9849
(s) $\kappa = 7.8533 - 0.0124i$ overlap=0.9439
(t) $\kappa = 8.1311 - 0.0107i$ overlap=0.9683

Figure 5.24: First 20 SPOT mode approximations in the quadrupole enclosure with impedance boundary conditions (case 1). Mode wavenumber shown below.

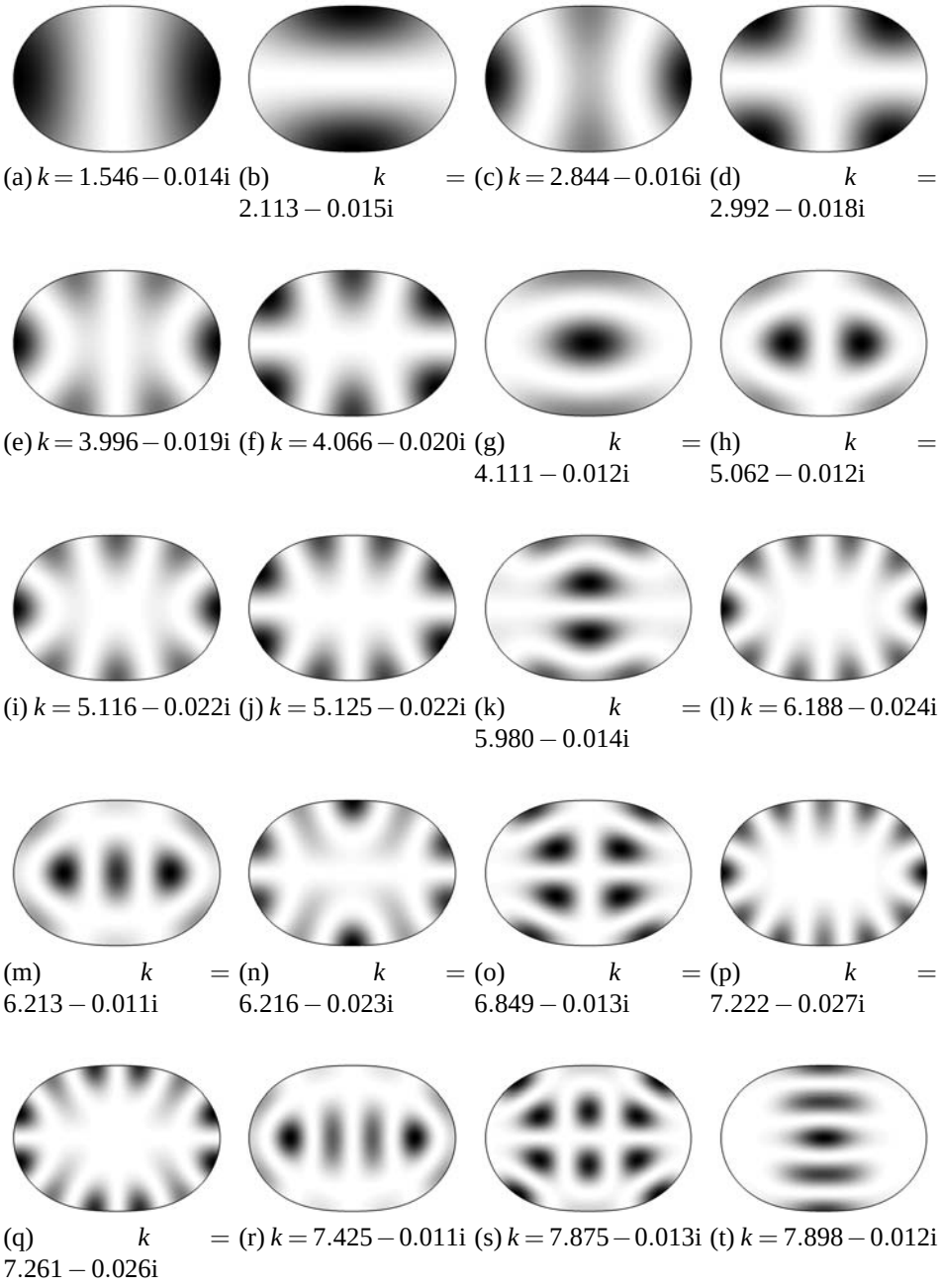

Figure 5.25: First 20 FEM approximated modes of the quadrupole enclosure with impedance boundary conditions (case 1). Mode wavenumber shown below.

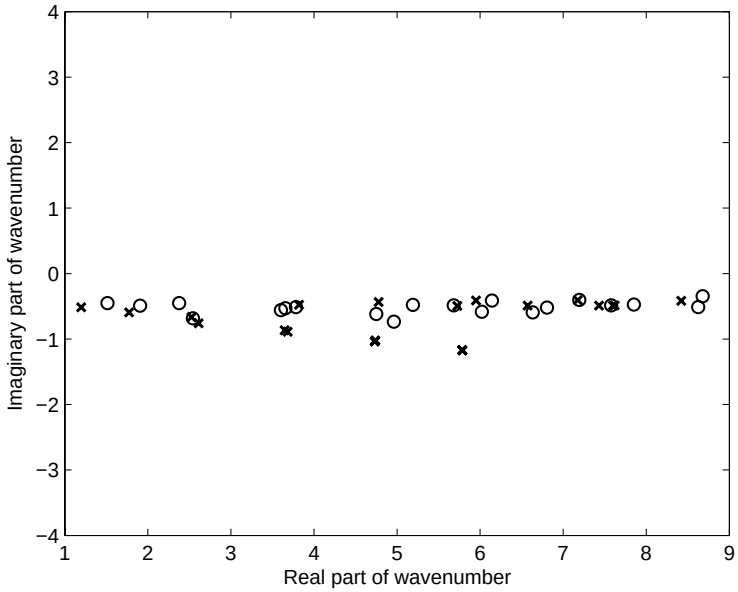

Figure 5.26: FEM mode wavenumbers ($\times$) and semiclassical approximations (o).

5.4.7 Impedance boundary conditions: Case 2

Impedance boundary conditions will be useful in understanding the mode shapes that occur in ducts which have been lined with acoustic damping material, for example. This case has a more realistic level of impedance of $A = 0.4 - 0.2\mathrm{i}$.

Figure 5.26 shows the real and imaginary parts of the mode wavenumbers calculated using FEM ('$\times$') and calculated using SPOT ('o'). The SPOT approximations do not seem to provide very accurate approximations to both the real and imaginary parts. Figure 5.27 (top) shows the absolute value of the difference between the SPOT and FEM mode wavenumbers. The absolute error is in most cases quite low compared to the spacing between the mode wavenumbers. Figure 5.27 (bottom) shows the overlap of the SPOT and the FEM mode shapes. These results are mostly over 80% but not all over 90% as seen in the previous examples. The technique is not so accurate for impedance boundary conditions as it is for Dirichlet or Neumann boundary conditions.

Figure 5.28 shows the resonance functions used in the construction of the SPOT

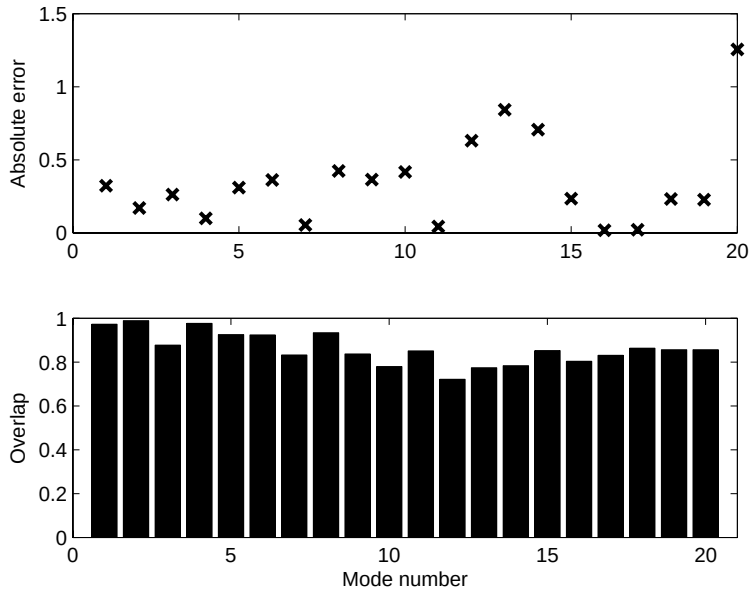

Figure 5.27: SPOT results for quadrupole enclosure with impedance boundary conditions. The top plot shows the absolute error between the SPOT approximation and the FEM mode wavenumber. The bottom plot shows the overlaps.

approximations. Figure 5.29 shows the SPOT approximations and figure 5.30 shows the FEM mode shapes.

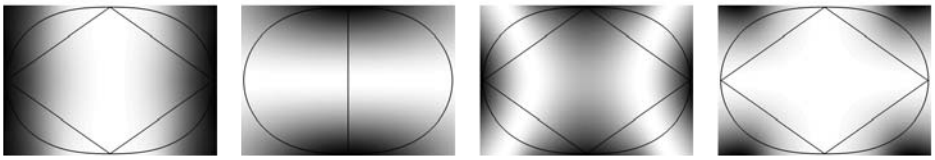

(a) $k_{BS} = 1.0656 - 0.8008i$ (b) $k_{BS} = 1.8777 - 0.4848i$ (c) $k_{BS} = 2.1607 - 0.8008i$ (d) $k_{BS} = 2.1607 - 0.8008i$

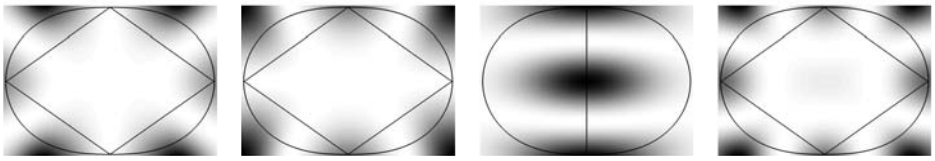

(e) $k_{BS} = 3.2557 - 0.8008i$ (f) $k_{BS} = 3.2557 - 0.8008i$ (g) $k_{BS} = 3.7702 - 0.4848i$ (h) $k_{BS} = 4.3507 - 0.8008i$

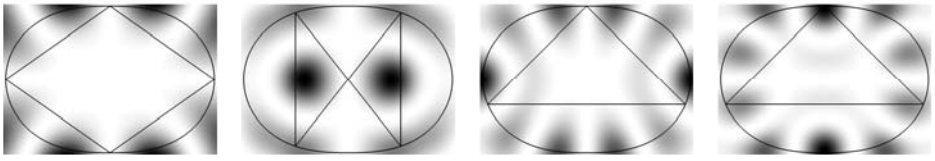

(i) $k_{BS} = 4.3507 - 0.8008i$ (j) $k_{BS} = 4.9682 - 0.4894i$ (k) $k_{BS} = 6.1042 - 0.5198i$ (l) $k_{BS} = 6.1042 - 0.5198i$

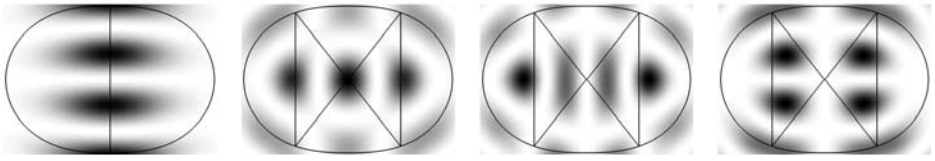

(m) $k_{BS} = 5.6628 - 0.4848i$ (n) $k_{BS} = 5.8844 - 0.4894i$ (o) $k_{BS} = 6.8006 - 0.4894i$ (p) $k_{BS} = 6.8006 - 0.4894i$

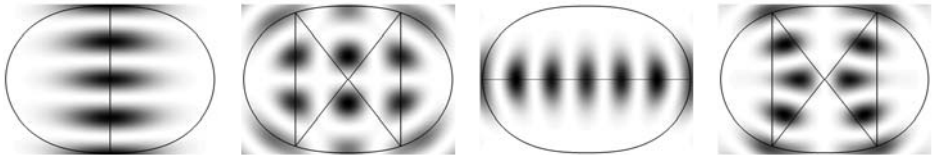

(q) $k_{BS} = 7.5553 - 0.4848i$ (r) $k_{BS} = 7.7168 - 0.4894i$ (s) $k_{BS} = 8.5285 - 0.3439i$ (t) $k_{BS} = 8.6330 - 0.4894i$

Figure 5.28: First 20 resonances functions in the quadrupole enclosure with impedance boundary conditions (case 2). Bohr-Sommerfeld quantization number shown below.

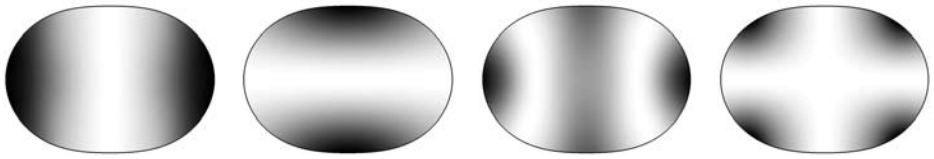

(a) κ = 1.5153 – 0.4527i overlap= 0.9724
(b) κ = 1.9082 – 0.4880i overlap= 0.9887
(c) κ = 2.3780 – 0.4505*i*i overlap= 0.8771
(d) κ = 2.5430 – 0.6847i overlap= 0.9760

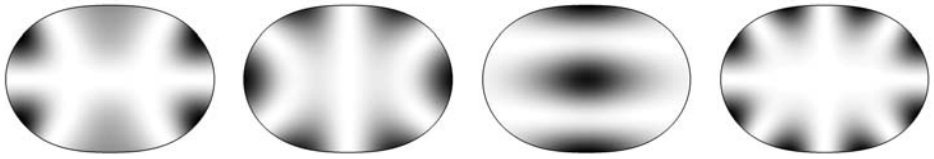

(e) κ = 3.6020 – 0.5592i overlap= 0.9249
(f) κ = 3.6560 – 0.5281i overlap= 0.9235
(g) κ = 3.7807 – 0.5138i overlap= 0.8320
(h) κ = 4.7512 – 0.6162i overlap= 0.9337

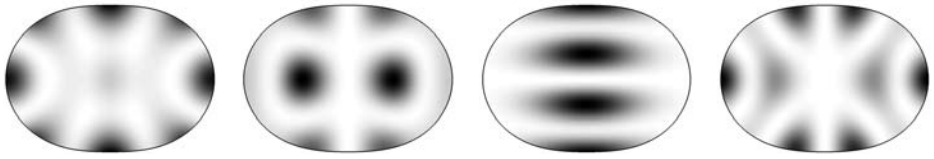

(i) κ = 4.9615 – 0.7329i overlap= 0.8365
(j) κ = 5.1923 – 0.4781i overlap= 0.7797
(k) κ = 5.6829 – 0.4854i overlap= 0.8506
(l) κ = 6.0195 – 0.5817i overlap= 0.7210

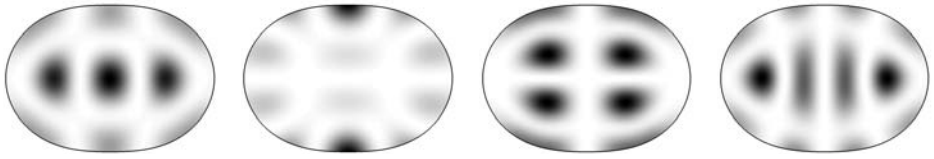

(m) κ = 6.1419 – 0.4110i overlap= 0.7743
(n) κ = 6.6332 – 0.5932i overlap= 0.7830
(o) κ = 6.8057 – 0.5201i overlap= 0.8526
(p) κ = 7.1937 – 0.4013i overlap= 0.8037

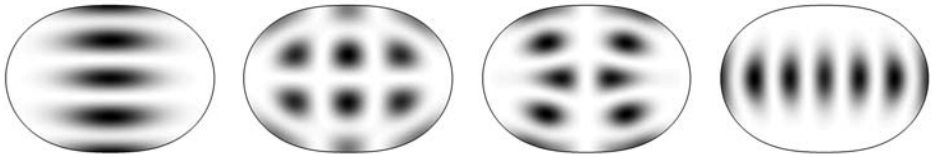

(q) κ = 7.5782 – 0.4856i overlap= 0.8309
(r) κ = 7.8512 – 0.4743i overlap= 0.8633
(s) κ = 8.6273 – 0.5127i overlap= 0.8561
(t) κ = 8.6793 – 0.3453i overlap= 0.8559

Figure 5.29: First 20 SPOT mode approximations of the quadrupole enclosure with impedance boundary conditions (case 2). Mode wavenumber shown below.

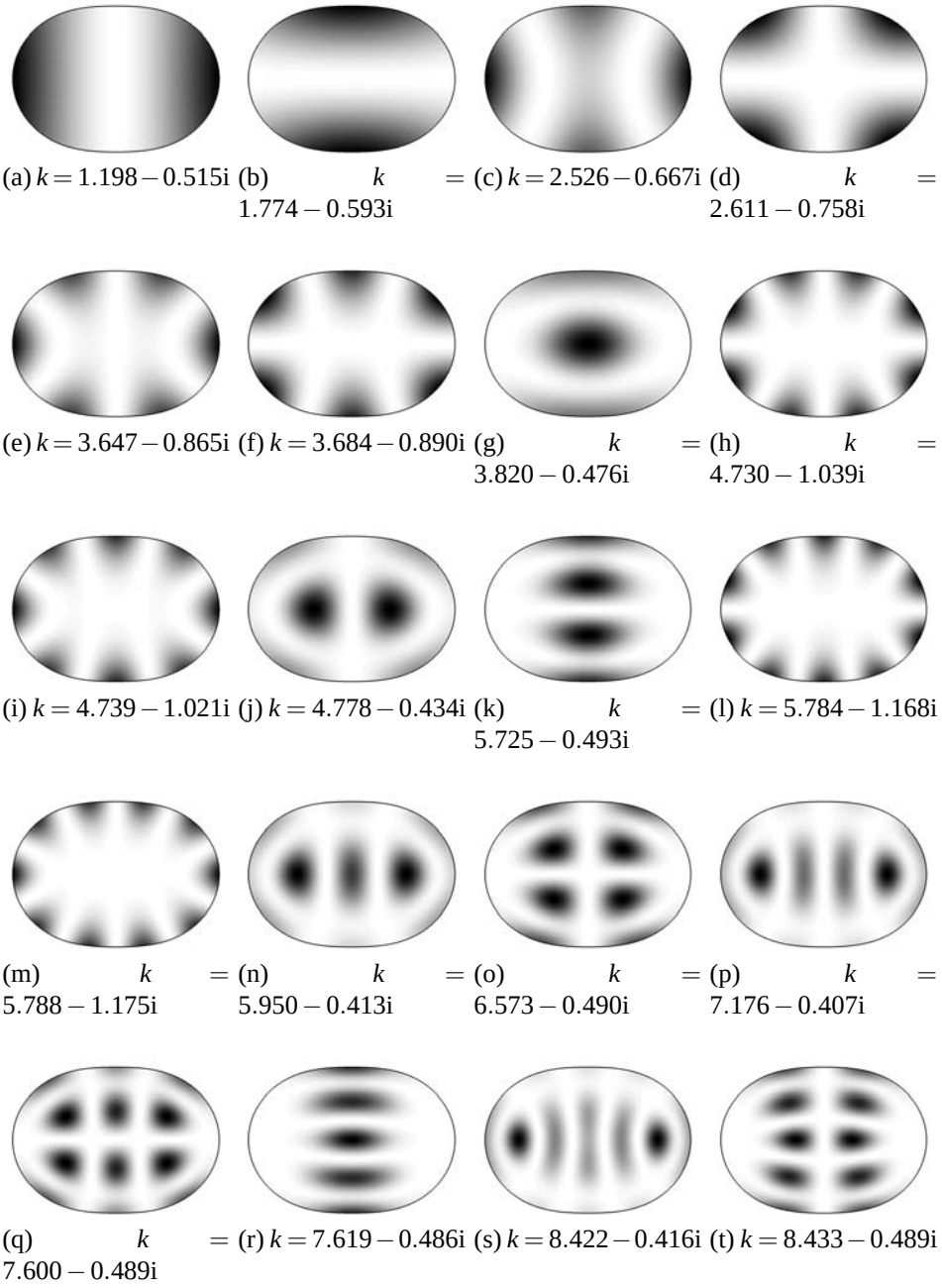

Figure 5.30: First 20 numerically approximated modes of the quadrupole enclosure with impedance boundary condition (case 2). Mode wavenumber shown below.

5.5 Circle enclosure

The circle is an integrable enclosure and as such the mode shapes can be found analytically. The ray dynamics in the circle are integrable so all the periodic orbits in the circle are marginally stable. An example of SPOT used on an integrable domain has not previously been published.

Figure 5.31 summarizes the results for the SPOT approximation in the circle enclosure. The first 20 distinct mode shapes have been found so where degeneracy exists only one of the mode shapes has been selected. However, degeneracy has been taken into account for unfolding the mode count. The mode wavenumbers were well approximated apart from modes 11, 16 and 18. The normalized error does not appear on figure 5.31 so figure 5.32 for these modes shows the normalized error with extended y-axis. The resonance functions associated with the periodic orbit chosen here do not approximate these mode shapes well. There may be a resonance function constructed from a longer periodic orbit that would provide a better approximation. The overlaps are approximately 90% or better for the first 14 distinct mode shapes indicating that these SPOT approximations are well correlated to the analytic mode shapes.

Figure 5.33 shows the resonance functions used in the construction of the SPOT approximations. Notice that only two periodic orbits have been used here. Figure 5.34 shows the SPOT approximations and figure 5.35 show the FEM mode shapes.

The circle is a very simple shape and it might be expected that SPOT would approximate the mode shapes very well. However, the results show that the mode shapes are not particularly well approximated. The mode shapes in the circle mostly have discrete rotational symmetries but not continuous rotational symmetry. The periodic orbits that generate the resonance functions do not necessarily have the same set of rotational symmetries as the mode shapes being approximated. This will

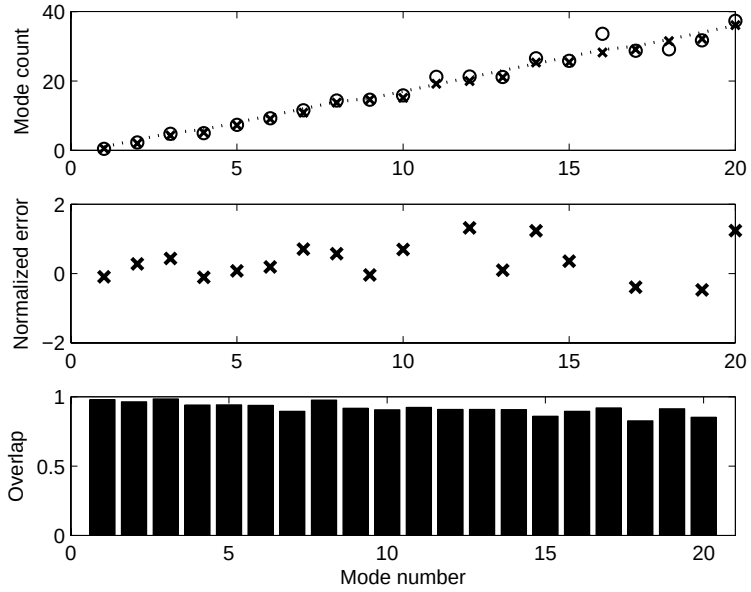

Figure 5.31: SPOT results for circle enclosure with Dirichlet boundary conditions. The top plot shows the unfolded mode count with '×' denoting the FEM mode wavenumbers and 'o' showing the SPOT approximation. The middle plot shows the normalized error and the bottom plot shows the overlaps.

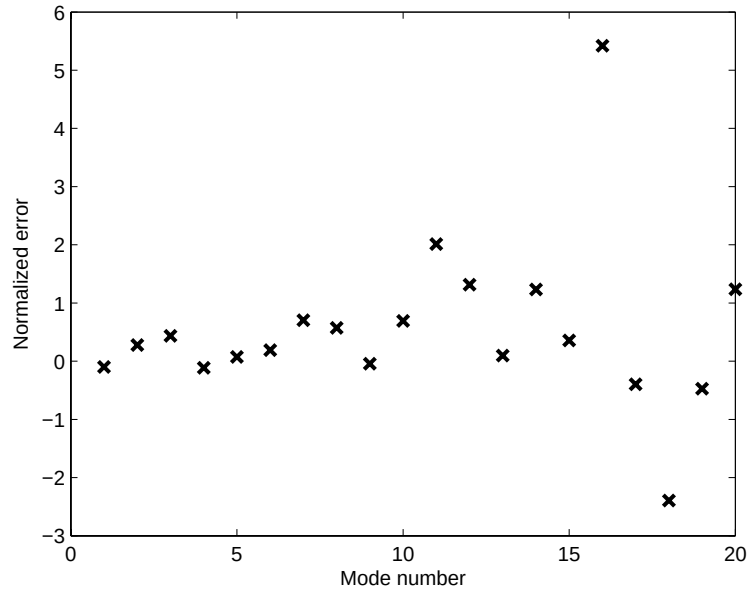

Figure 5.32: SPOT results for circle enclosure with Dirichlet boundary conditions. The normalized error on a larger *y*-axis so that modes 11, 16 and 18 can be seen.

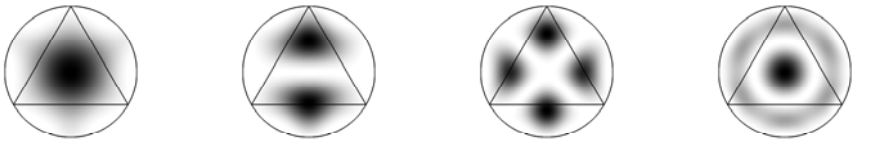

(a) $k_{BS} = 2.7207$ (b) $k_{BS} = 3.9299$ (c) $k_{BS} = 5.1391$ (d) $k_{BS} = 6.3483$

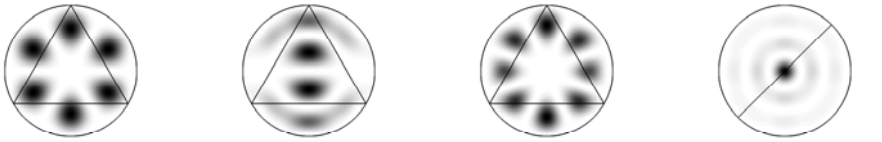

(e) $k_{BS} = 6.3483$ (f) $k_{BS} = 7.5575$ (g) $k_{BS} = 7.5575$ (h) $k_{BS} = 8.6394$

(i) $k_{BS} = 8.7667$ (j) $k_{BS} = 8.7667$ (k) $k_{BS} = 9.9759$ (l) $k_{BS} = 9.9759$

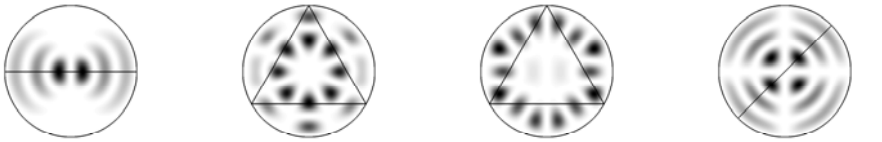

(m) $k_{BS} = 10.2102$ (n) $k_{BS} = 11.1851$ (o) $k_{BS} = 11.1851$ (p) $k_{BS} = 11.7810$

(q) $k_{BS} = 11.7810$ (r) $k_{BS} = 12.3943$ (s) $k_{BS} = 12.3943$ (t) $k_{BS} = 13.3518$

Figure 5.33: First 20 resonance functions in the circle enclosure with Dirichlet boundary conditions. Bohr-Sommerfeld quantization number shown below.

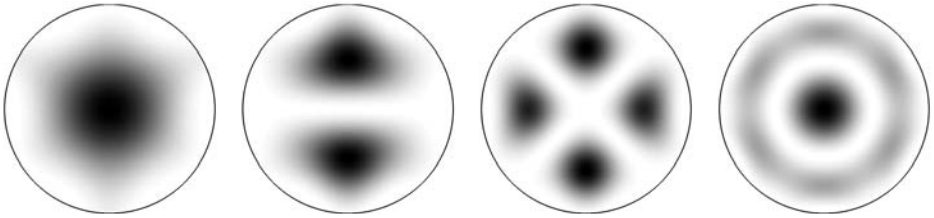

(a) $\kappa = 2.2580$ overlap= 0.9798 (b) $\kappa = 4.0210$ overlap= 0.9642 (c) $\kappa = 5.3405$ overlap= 0.9847 (d) $\kappa = 5.4702$ overlap= 0.9403

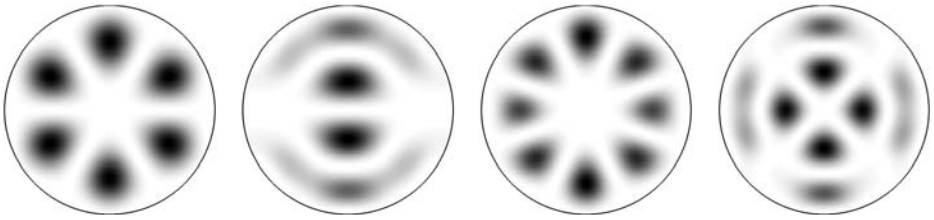

(e) $\kappa = 6.4079$ overlap= 0.9423 (f) $\kappa = 7.0785$ overlap= 0.9382 (g) $\kappa = 7.7985$ overlap= 0.8955 (h) $\kappa = 8.5702$ overlap= 0.9763

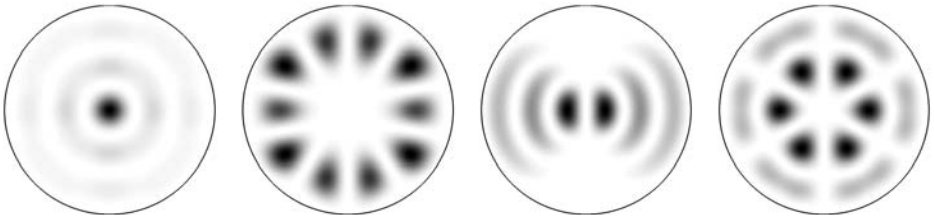

(i) $\kappa = 8.6427$ overlap= 0.9167 (j) $\kappa = 8.9481$ overlap= 0.9065 (k) $\kappa = 10.1945$ overlap= 0.9232 (l) $\kappa = 10.2091$ overlap= 0.9086

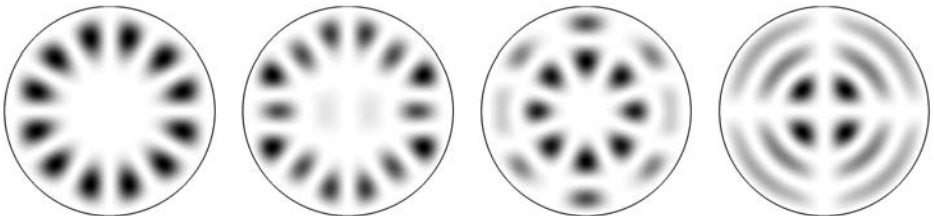

(m) $\kappa = 10.2256$ overlap= 0.9087 (n) $\kappa = 11.1570$ overlap= 0.9078 (o) $\kappa = 11.3069$ overlap= 0.8601 (p) $\kappa = 11.7180$ overlap= 0.8953

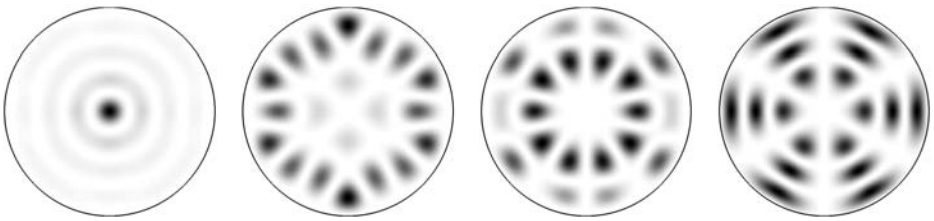

(q) $\kappa = 11.7900$ overlap= 0.9196 (r) $\kappa = 12.2551$ overlap= 0.8269 (s) $\kappa = 12.5956$ overlap= 0.9133 (t) $\kappa = 13.2191$ overlap= 0.8528

Figure 5.34: First 20 SPOT mode approximations in the circle enclosure with Dirichlet boundary conditions. Mode wavenumber shown below.

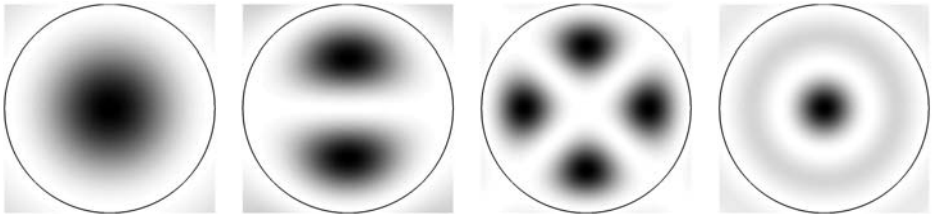

(a) $k = 2.4048$ (b) $k = 3.8317$ (c) $k = 5.1356$ (d) $k = 5.5201$

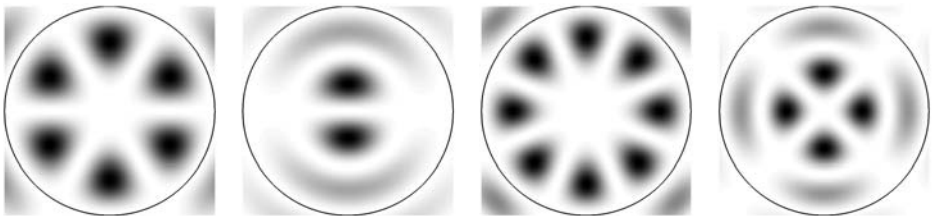

(e) $k = 6.3802$ (f) $k = 7.0156$ (g) $k = 7.5883$ (h) $k = 8.4172$

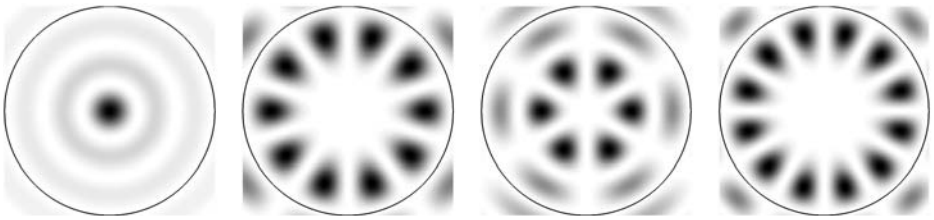

(i) $k = 8.6537$ (j) $k = 8.7715$ (k) $k = 9.7610$ (l) $k = 9.9361$

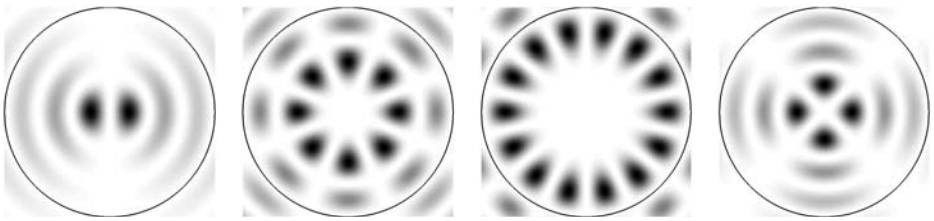

(m) $k = 10.1735$ (n) $k = 11.0647$ (o) $k = 11.0864$ (p) $k = 11.6198$

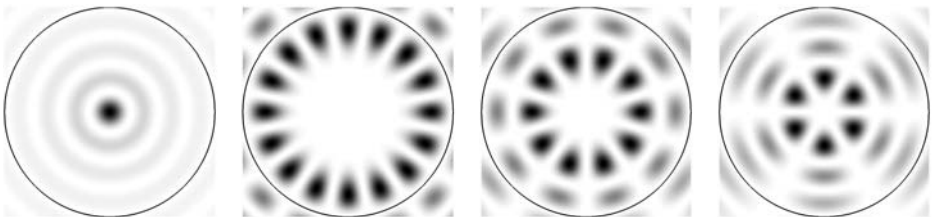

(q) $k = 11.7915$ (r) $k = 12.2251$ (s) $k = 12.3386$ (t) $k = 13.0152$

Figure 5.35: First 20 analytic modes of the circle enclosure with Dirichlet boundary conditions. Mode wavenumber shown below.

mean that the resonance functions will not have the same rotational symmetries as the mode shapes. This will introduce some error into the mode shape approximation comprised of these resonance functions. Alternatively, the integrability of the circle maybe responsible.

5.6 Eccentric annulus enclosure

The eccentric annulus is an enclosure with mixed ray dynamics. It also has a hole within the domain which makes the approximation more difficult. A periodic orbit may pass very close to the hole boundary, but the resonance function constructed using that periodic orbit will take no account of the hole. This means that the boundary conditions on the hole boundary will be violated by that resonance function. This is particularly noticeable at low frequency. The scaling perpendicular to the ray was given in chapter 4 as $y \sim \sqrt{kl}$ so the periodic orbit should be at least that distance from the boundary. The ray dynamics and periodic orbits were considered by Gouesbet *et al* [32] for the parameters used here.

Figure 5.36 summarizes the results for the SPOT approximation in the eccentric annulus enclosure. The mode wavenumbers are well approximated by SPOT. The normalized error is generally less than the average level spacing. The overlaps are quite high but again not as high as in the quarter stadium case. There are 10 modes with overlaps greater than 90% which indicates that the SPOT approximations and the FEM modes are well correlated. A further eight of the modes have an overlap over 80%. The other two modes have an overlap over 70%.

Figure 5.37 shows the resonance functions used in the construction of the SPOT approximations. Notice that only four periodic orbits have been used. Figure 5.38 shows the SPOT approximations and figure 5.39 show the FEM mode shapes.

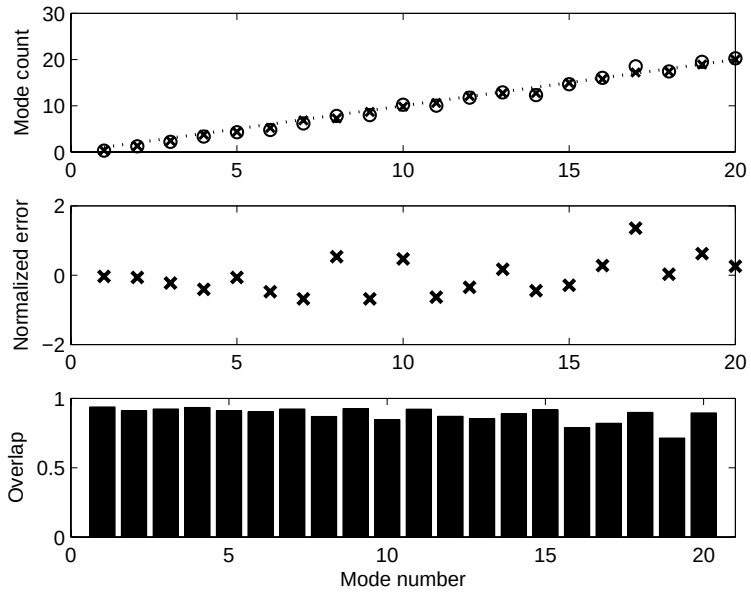

Figure 5.36: SPOT results for eccentric annulus enclosure with Dirichlet boundary conditions. The top plot shows the unfolded mode count with '$\times$' denoting the FEM mode wavenumbers and 'o' showing the SPOT approximation. The middle plot shows the normalized error and the bottom plot shows the overlaps.

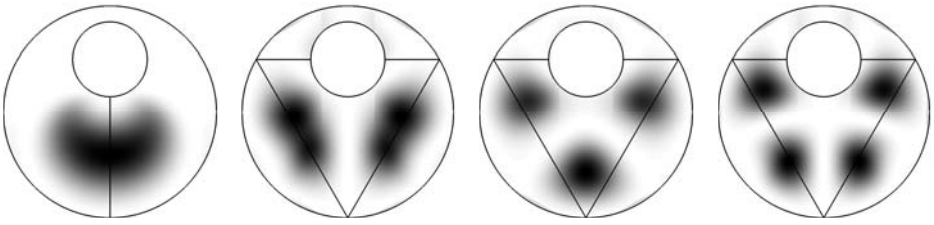

(a) $k_{BS} = 3.4148$ (b) $k_{BS} = 4.1924$ (c) $k_{BS} = 4.8911$ (d) $k_{BS} = 5.5898$

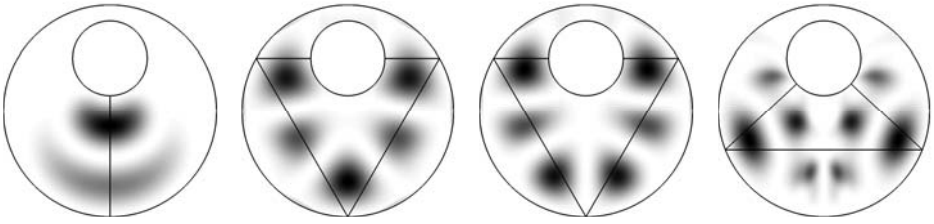

(e) $k_{BS} = 6.1466$ (f) $k_{BS} = 6.2886$ (g) $k_{BS} = 6.9873$ (h) $k_{BS} = 7.6341$

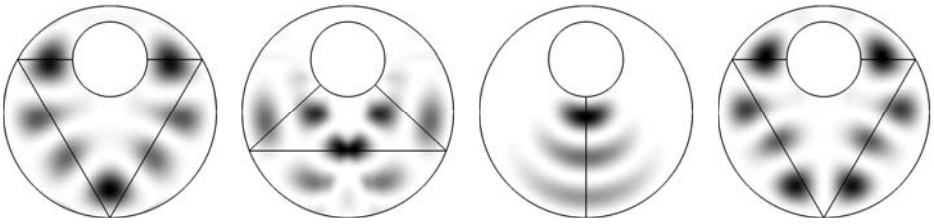

(i) $k_{BS} = 7.6860$ (j) $k_{BS} = 8.4824$ (k) $k_{BS} = 8.8784$ (l) $k_{BS} = 8.3847$

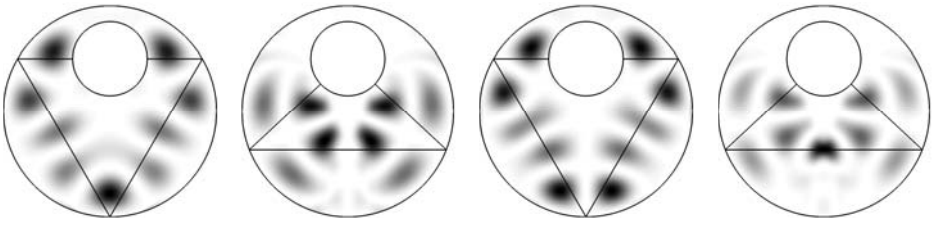

(m) $k_{BS} = 9.0835$ (n) $k_{BS} = 9.3306$ (o) $k_{BS} = 9.7822$ (p) $k_{BS} = 10.1789$

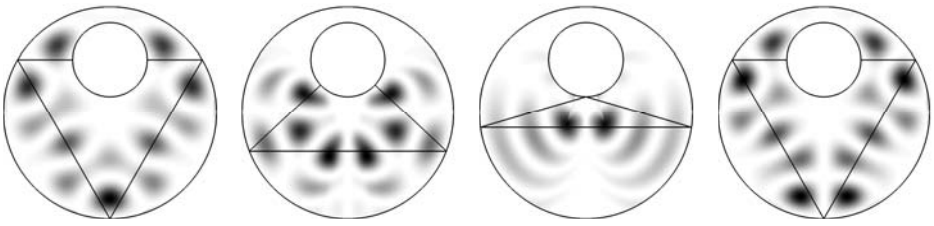

(q) $k_{BS} = 10.4809$ (r) $k_{BS} = 11.0271$ (s) $k_{BS} = 10.8764$ (t) $k_{BS} = 11.1797$

Figure 5.37: First 20 resonance functions of the eccentric annulus with Dirichlet boundary conditions. Bohr-Sommerfeld quantization number shown below.

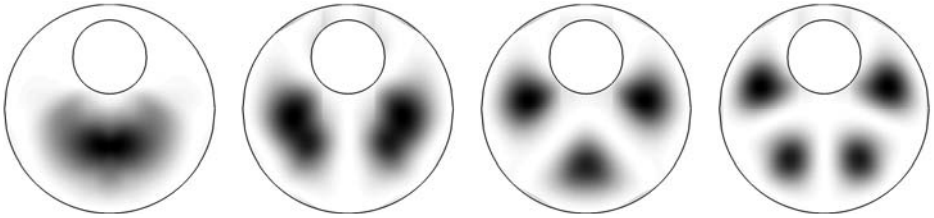

(a) $\kappa = 3.1405$ overlap= 0.9381 (b) $\kappa = 4.1466$ overlap= 0.9112 (c) $\kappa = 4.8769$ overlap= 0.9239 (d) $\kappa = 5.5789$ overlap= 0.9341

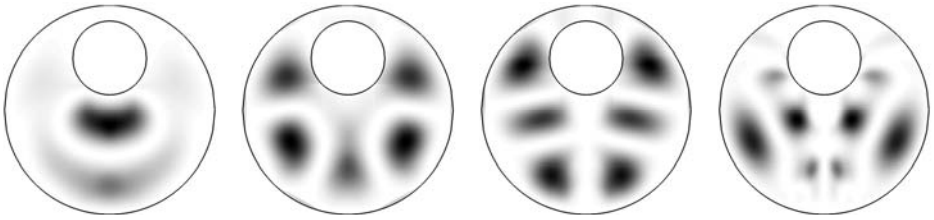

(e) $\kappa = 6.0944$ overlap= 0.9117 (f) $\kappa = 6.3175$ overlap= 0.9023 (g) $\kappa = 6.9458$ overlap= 0.9233 (h) $\kappa = 7.5987$ overlap= 0.8689

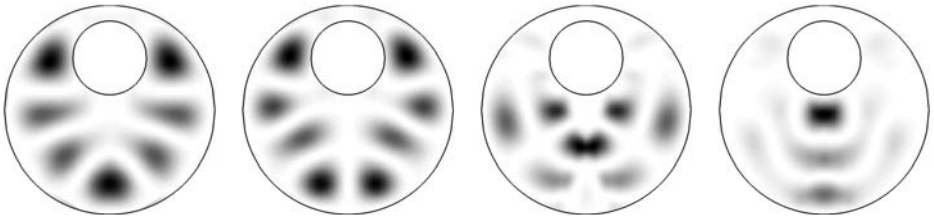

(i) $\kappa = 7.6668$ overlap= 0.9258 (j) $\kappa = 8.3738$ overlap= 0.8453 (k) $\kappa = 8.4618$ overlap= 0.9224 (l) $\kappa = 8.9432$ overlap= 0.8713

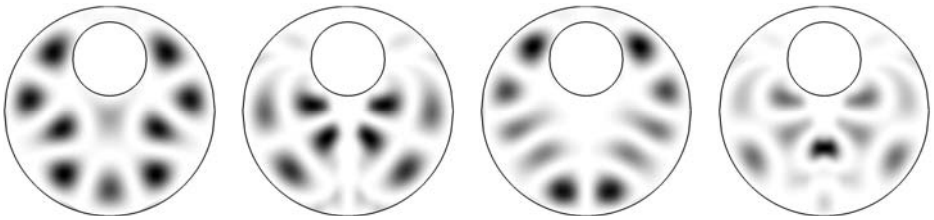

(m) $\kappa = 9.1023$ overlap= 0.8533 (n) $\kappa = 9.2803$ overlap= 0.8888 (o) $\kappa = 9.7903$ overlap= 0.9169 (p) $\kappa = 10.1572$ overlap= 0.7880

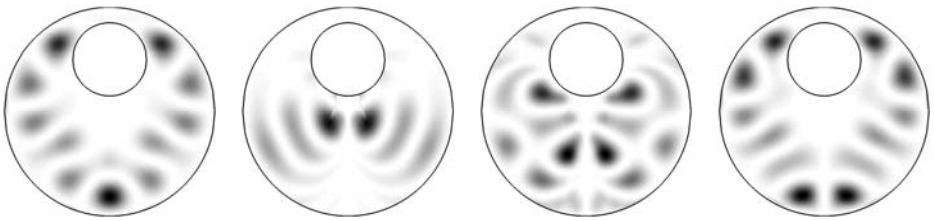

(q) $\kappa = 10.5106$ overlap= 0.8199 (r) $\kappa = 10.8002$ overlap= 0.8992 (s) $\kappa = 11.0355$ overlap= 0.7139 (t) $\kappa = 11.2049$ overlap= 0.8950

Figure 5.38: First 20 SPOT mode approximations of the eccentric annulus. Mode wavenumber shown below.

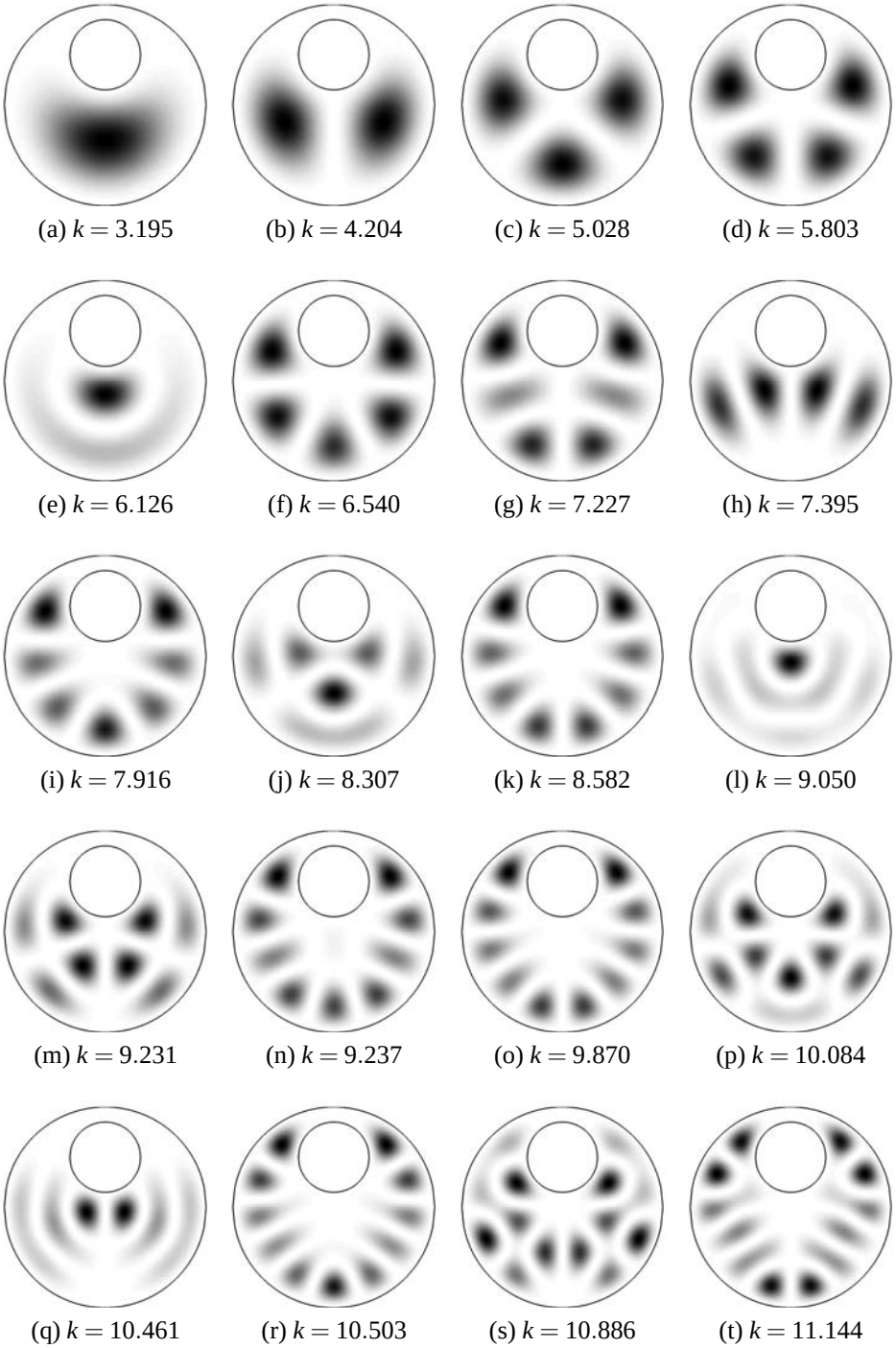

(a) $k = 3.195$ (b) $k = 4.204$ (c) $k = 5.028$ (d) $k = 5.803$

(e) $k = 6.126$ (f) $k = 6.540$ (g) $k = 7.227$ (h) $k = 7.395$

(i) $k = 7.916$ (j) $k = 8.307$ (k) $k = 8.582$ (l) $k = 9.050$

(m) $k = 9.231$ (n) $k = 9.237$ (o) $k = 9.870$ (p) $k = 10.084$

(q) $k = 10.461$ (r) $k = 10.503$ (s) $k = 10.886$ (t) $k = 11.144$

Figure 5.39: First 20 FEM mode shapes of the eccentric annulus. Mode wavenumber shown below.

5.7 Concluding remarks

In this chapter examples of the short periodic orbit theory (SPOT) for mode shape approximation at low wavenumber have been given in four different enclosures with different boundary conditions.

5.7.1 Quarter stadium enclosure

Two examples of mode shape approximation using SPOT were given for the quarter stadium. The first with all Dirichlet boundary conditions was the one given by Vergini and Carlo [27]. The second has a Neumann boundary condition on one side. These cases correspond to the odd-odd and odd-even mode shapes in the full stadium enclosure. The normalized error is less than ± 0.35 which indicates a good approximation of the wavenumbers. The overlap between the SPOT approximations and the FEM modes are of the order of 98% or above in most cases. This shows that the method has produced very good approximations to the modes.

The Mode Resonance Function Hypothesis has been passed for the quarter stadium enclosure for both sets of boundary conditions. This would indicate that there is a connection between mode shapes and periodic orbits in this enclosure as postulated by Heller.

5.7.2 Quadrupole enclosure

Mode shapes were approximated using SPOT for four different sets of boundary conditions. The mode wavenumbers were well approximated in general. The best mode wavenumber approximations were for the Dirichlet boundary conditions, next best were Neumann boundary conditions and the worst were impedance boundary conditions. The normalized error was greater than for the quarter stadium enclosure but still much less than ± 1 for the Dirichlet and Neumann cases. The overlap results showed the same trend. The Dirichlet mode shapes were best approximated then

Neumann and worst were impedance boundary conditions.

The Mode Resonance Function Hypothesis has been supported for the quadrupole enclosure with Dirichlet and Neumann boundary conditions. The hypothesis was also supported for the impedance boundary condition case 1. However it was not supported for the impedance boundary condition case 2. This would indicate that wave effects are more important in this case.

5.7.3 Circle enclosure

The mode shapes in the circle enclosure results were generally well approximated. The fact that the first 20 distinct mode shapes were approximated meant that in fact almost the first 40 mode shapes were found. If the first 20 modes taking into account degeneracy were looked at the SPOT is more successful. It should also be noted that only 2 periodic orbits were used to produce these approximations. Greater accuracy may be achieved if different orbits had been selected.

The Mode Resonance Function Hypothesis has not been passed for the circle enclosure, but it was very close.

5.7.4 Eccentric annulus enclosure

The eccentric annulus results were not as good as those for the quarter stadium but given the limitations of the theory in the presence of a hole the results are remarkably good. The wavenumbers are generally well approximated and the overlaps are high. The rays in an enclosure with a hole would display diffraction and this has not been accounted for here.

The Mode Resonance Function Hypothesis has not been passed here to the level defined, although the agreement is quite high.

5.7.5 Final remarks

SPOT has provided good approximations for the mode shapes in several different enclosures and with different boundary conditions. The SPOT is a high frequency approximation so the agreement achieved at low frequency is even more surprising. In the next chapter higher frequency mode shapes will be investigated.

The results in this chapter show that mode shapes can be approximated just using resonance functions to a reasonably level of accuracy in certain enclosures. However, the results show that there does not seem to be any *a priori* way that is currently known of predicting which shapes the SPOT is likely to be good approximation for.

There are a number of factors that seem to improve performance, for example mode shapes in a convex enclosure are generally better approximated. Chaotic ray dynamics also seem to improve the results with a completely chaotic enclosure having the best approximations. Enclosures with Dirichlet and Neumann boundary conditions are better approximated than those with impedance boundary conditions.

Chapter 6

Towards enclosure design

An understanding of how the shape of an enclosure relates to its modes is of interest in many areas of acoustics and physics as previously discussed. An application could be to reducing the weight of an engine part by cutting a hole in it. An appropriate position for the hole to be cut must be found. There are a number of things to consider. The plate needs to retain the ability to fulfil its structural role, but it will be assumed that this will be the case here.

It may be important that the new plate does not radiate sound in a particular direction or that the operating frequency of the engine is not the same as a resonance of the plate. The mode shapes provide the information required to understand these problems. Numerical methods could be used to find the mode shapes when different parts of the plate are removed.

Unfortunately, the numerical method would have to be repeated many times for an indication of the best part of the plate to be removed. Numerical techniques can be computationally expensive, especially at high frequency and so this approach may not be practical. Indeed the mode shapes may be very sensitive to the location of the part to be removed and so numerical methods may not provide much insight at all. Analytical techniques do not provide much insight either. Small perturbation techniques, such as [58], are difficult to apply and do not work well for large per-

turbations. A method that allows an understanding of the mode shapes based on the geometry of the enclosure is therefore important. Periodic orbits and SPOT may be able to provide this understanding.

A design loop for enclosures is proposed and explained in section 6.1. In section 6.2 a model problem will be given, which will be used to investigate methods to complete each of the steps in the design loop and to assess the feasibility of each step. Section 6.3 introduces methods for decomposing mode shapes in to periodic orbit contributions. The Husimi function is reviewed in section 6.4 and a new method called the ray direction function is suggested in section 6.5. 20 mode shapes are decomposed into their resonance function components in section 6.6. Some comments are made about mode dynamics in section 6.7. Sections 6.8 and 6.9 give brief comments about approximating new mode shapes and the validation of the output of the design loop. Conclusions are given in section 6.10.

6.1 Design loop

The idea of the last chapters has been that mode shapes are made up of resonance functions, which in turn are calculated from periodic orbits. This is the Mode Resonance Function Hypothesis. It has been shown to have some success at low wavenumbers in the previous chapter. This idea could be used to inform the design of enclosures at higher frequencies.

A loop for enclosure design is proposed, see figure 6.1. An enclosure has, in a certain situation, one or more mode shapes that have characteristics that either need to be kept or removed. It can be assumed that this mode shape has been measured experimentally or it may be the result of a numerical method. This mode shape will be broken down into the resonance functions that are predominantly present and the periodic orbits underlying these resonance functions identified. An analysis of how the periodic orbits change when the enclosure changes can then be carried out. The

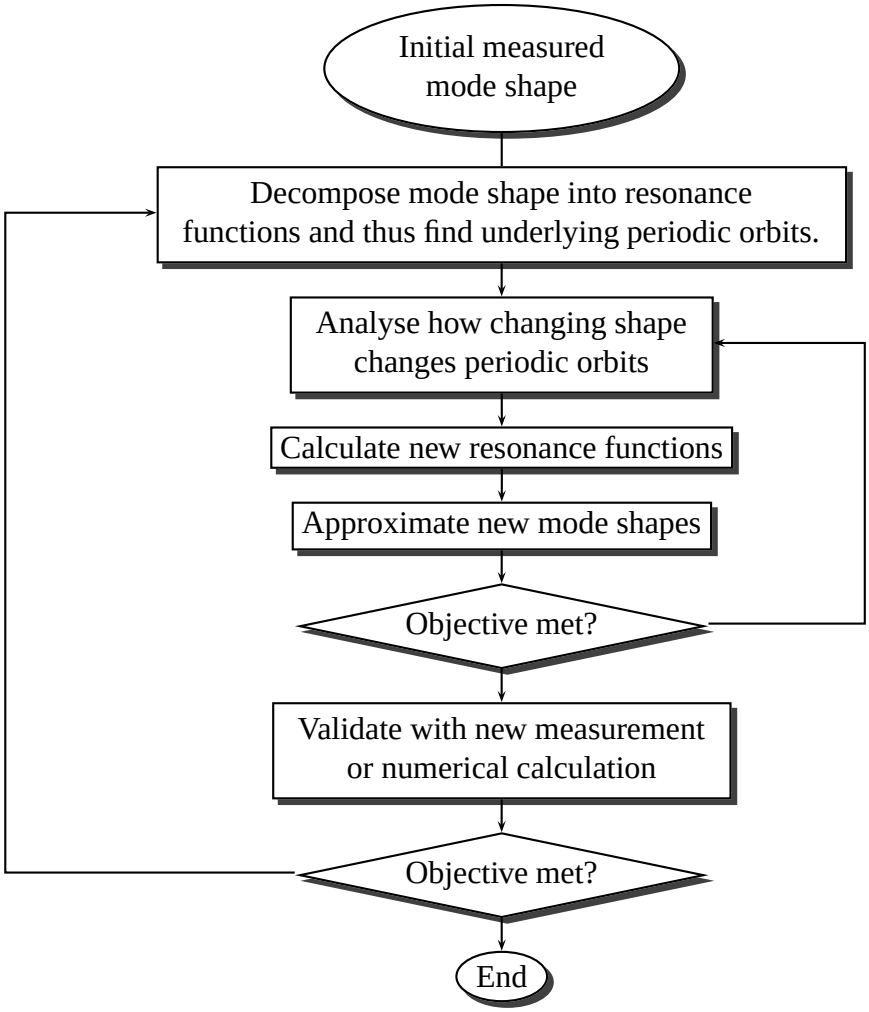

Figure 6.1: Flow diagram for enclosure design.

enclosure can be changed to meet the objectives of the exercise, say the removal of a mode shape which is localized in a particular area. The new mode shapes can then be approximated using the SPOT or the fact that the objective has been met can be validated using the numerical technique or a further experimental measurement. This design method should reduce the numerical runs and more importantly improve understanding in the design process.

6.2 Model problem

There are a large number of variables and other effects to be considered for a metal plate in an engine. A greatly simplified model should be considered in the first instance to establish whether it is possible to use the design loop in principle. The model problem is to understand how the mode shapes determined by the Helmholtz equation

$$(\nabla^2 + k^2)\Psi(\mathbf{x}) = 0, \tag{6.1}$$

with the boundary condition,

$$\Psi(\mathbf{x}) = 0 \quad \text{on} \quad \partial\mathscr{D}, \tag{6.2}$$

change as the boundary $\partial\mathscr{D}$ changes.

The basic enclosure considered will be the eccentric annulus, with unit outer radius $R = 1$ and inner radius $r = 0.35R$, see figure 6.2. The eccentricity ε can be varied to provide the change in shape. This is the enclosure used by Gouesbet *et al* [32]. It was seen in chapter 5 that the mode shapes in the eccentric annulus were not well approximated by SPOT in general. The eccentric annulus will be used here because a large catalogue of periodic orbits has already been found and because it has a shape parameter that can easily be varied.

The finite element method will be used to find a numerical solutions to this model

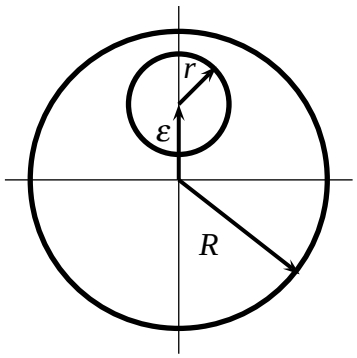

Figure 6.2: Eccentric annulus enclosure.

problem to provide the initial mode shapes. The details of FEM can be found in the appendix A.

6.3 Modes to periodic orbits

The first step in the design loop is to break the mode shape down into resonance function contributions. The periodic orbits in the enclosure are required for this. The periodic orbits can be found by one of the techniques outlined in chapter 2. The periodic orbits are known for this model problem because they are given in Gouesbet *et al* [32] for up to six bounces against the outer boundary.

There are several methods for finding which periodic orbit resonance functions are present in a mode shape. The most basic method is by inspection of the mode shape. If the mode shape is scarred, then the periodic orbit may stand out. However, this is not always the case, some resonance functions do not look much like the periodic orbit that underlies it. Phase space functions, such as the Husimi function, which link the mode shape to the underlying ray dynamics are given in section 6.4. A new method called the ray direction function is developed in section 6.5.

The most direct method of decomposing a mode shape is to directly compare resonance functions with mode shapes. The periodic orbits are used to calculate the

resonance functions for the same wavenumber range as the mode shape and then the resonance function with the largest overlap is found. This approach will be described and attempted in section 6.6.

6.4 Husimi function

The Husimi function is part of a family of functions called phase space distribution functions. Phase space distribution function theory has been reviewed by Lee [59]. Phase space distribution functions connect mode shapes with regions of the Poincaré section. This has the practical value of showing which periodic orbits may be associated with a particular mode.

The phase space distribution functions are four-dimensional for two-dimensional enclosures. At each position in the enclosure (x,y) the ray has a direction vector (k_x,k_y) and so the mode shape has to be mapped onto this four-dimensional space. The mapping is not unique so several different types of phase space distribution have been developed. The two that have been used most in the quantum chaology literature are the Wigner function [60] and the Husimi function [61, 62]. The Wigner function is both positive and negative and oscillates, which makes it less clear. The Husimi function is generally preferred in the literature because it is non-negative and oscillates less [18].

6.4.1 Husimi function definition

The Husimi function is defined for a mode shape $\psi_n(\mathbf{x})$ as [59]

$$F^H(\mathbf{q},\mathbf{p}) = a(k_n,b)\left|\int_\Omega \exp(-b(\mathbf{x}-\mathbf{q})^2 k_n/2)\exp(-\mathrm{i}k_n\mathbf{p}.\mathbf{x})\psi(\mathbf{x})\,\mathrm{d}\mathbf{x}\right|^2, \qquad (6.3)$$

where b is a positive constant and $a(k_n,b)$ is given in Lee [59]. The value of b alters the resolution between the position $\mathbf{q}$ and the momentum $\mathbf{p}$. The wavenumber of the

mode is k_n.

This function produces a four-dimensional surface which corresponds to the four-dimensional phase space of a two-dimensional enclosure. Four-dimensional surfaces are difficult to visualize. In a similar way that the ray dynamics were reduced to the boundary earlier to produce the Poincaré section the Husimi function will be reduced to the boundary.

6.4.2 Poincaré Husimi function

This Poincaré Husimi function corresponds to the Poincaré surface that has been used to study the ray dynamics earlier. The derivation of the Poincaré Husimi function from the Husimi function is given in Bäcker *et al* [63]. Details for other boundary conditions are given in Hentschel *et al* [64]. The derivation will not be given here, instead the Poincaré Husimi function will be defined, Bäcker *et al* [63], as

$$h_n(q,p) = d(k_n)\left|\int_{\partial\Omega} e^{-\mathrm{i}k[p(s-q)+(b/2)(s-q)^2]}[\hat{\mathbf{n}}(\mathbf{x}(s)).\nabla\psi_n(\mathbf{x}(s))]\,\mathrm{d}s\right|^2, \qquad (6.4)$$

where $d(k_n)$ is given in Bäcker *et al* [63] and periodicity around the boundary is assumed. The position on the boundary is q and the momentum is p as before.

The mode shape is $\psi_n(\mathbf{x}(s))$ where s is the length along the boundary. The total length of the boundary is L and m is an integer taking account of the periodicity around the boundary. The normal to the boundary at the point $\mathbf{x}(s)$ is $\hat{\mathbf{n}}(\mathbf{x}(s))$.

Only the relative amplitude of Poincaré Husimi function is sought when periodic orbit scars are required. If the periodicity of the boundary length is also taken into account, the Poincaré Husimi function reduces to

$$h_n(q,p) = \left|\int_{\partial\Omega} \mathrm{e}^{\mathrm{i}kp(s-q)}\mathrm{e}^{-k(s-q)^2}(\hat{\mathbf{n}}(s).\nabla\Psi(s))\,\mathrm{d}s\right|^2 \qquad (6.5)$$

where $\mathbf{x}(s)$ is a point on the boundary $\partial\Omega$ parameterized by arc length s. The outward

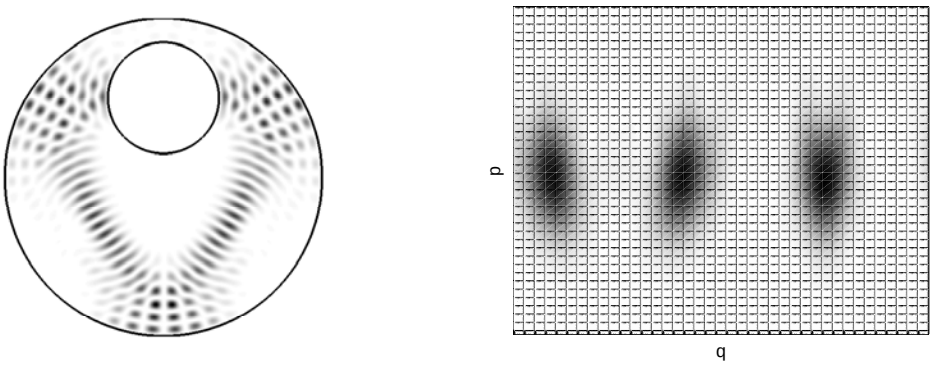

(a) Mode shape scarred by orbit 6(2)1 $kR = 47.493$. (b) Poincaré Husimi function of this mode shape

Figure 6.3: Mode shape and its Poincaré Husimi function

normal unit vector at the point s is denoted by $\hat{\mathbf{n}}(s)$.

Figure 6.3 shows a plot of the Poincaré Husimi function for the mode shape shown next to it. The Poincaré Husimi function is clearly localized around certain areas in phase space. These peaks are localized in the areas of the Poincaré section associated with the periodic orbit called 6(2)1 by Gouesbet *et al* [32].

6.4.3 Limitations of the Poincaré Husimi function

Unfortunately, there are some limitations to the Poincaré Husimi function such as the resolution and when there is more than one periodic orbit resonance present.

Resolution

The first limitation of the Poincaré Husimi function is that there is only limited resolution in (p,q) space. If b is altered to provide more resolution in p then the resolution in q suffer. The lower the wavenumber the more spread out the activity in the Poincaré Husimi function.

A large number of points on the boundary are required to have a sufficiently smooth boundary function which will produce an accurate Poincaré Husimi function. This is a problem especially at high frequency when the initial data has either been acquired from an experiment or from numerical results.

Superposition of resonance functions

There are many mode shapes where there are several periodic orbit resonance functions present. These are superimposed on one another in the Poincaré Husimi function for that mode shape, so it can become difficult to separate out the resonance functions.

6.5 Ray direction function

The ray direction function as it will be called has been developed as an alternative method for finding periodic orbit resonances, which does not suffer from some of the limitations of the Poincaré Husimi function. This was developed from an initial idea suggested by Wright [65].

The Fourier transform in two-dimensions can be written as

$$\Psi_n(k_x,k_y) = \int\int_{\mathscr{D}} \psi_n(x,y)\mathrm{e}^{-\mathrm{i}\mathbf{k}_n.\mathbf{x}}\,\mathrm{d}\mathbf{x}. \tag{6.6}$$

The transform will be weighted so that it is in effect only over a small area of the enclosure. A two-dimensional Gaussian weighting centered on the point of interest will be used. The Fourier transform thus becomes

$$\Psi_n(k_x,k_y;\mathbf{x}_1) = \int\int_{\mathscr{D}} \mathrm{e}^{-k_n(\mathbf{x}-\mathbf{x}_1)^2}\psi_n(x,y)\mathrm{e}^{-\mathrm{i}\mathbf{k}_n.\mathbf{x}}\,\mathrm{d}\mathbf{x}. \tag{6.7}$$

The mode wavenumber can be expressed in component form as

$$\mathbf{k}_n = (k_n\cos(\theta), k_n\sin(\theta)), \tag{6.8}$$

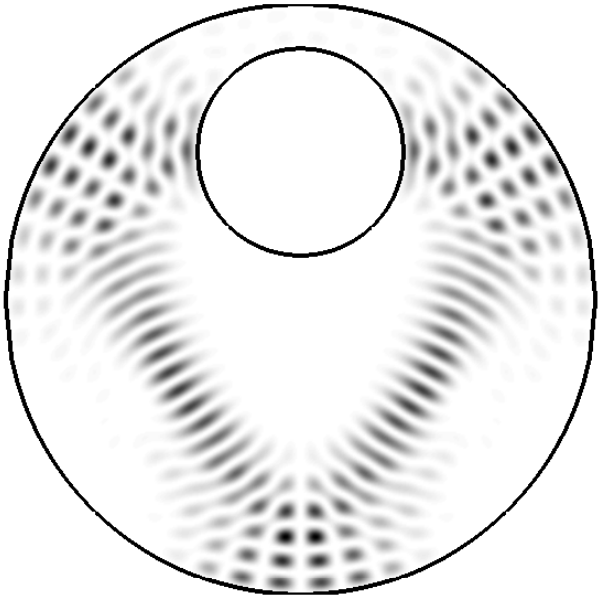

Figure 6.4: Mode shape $k = 47.4931$.

since $|\mathbf{k}_n| = k_n$. The function that will be evaluated is as follows

$$\Psi_n(\theta, x_1, y_1) = \int\int_{\mathscr{D}} \mathrm{e}^{-k_n((x-x_1)^2+(y-y_1)^2)} \psi_n(x,y) \mathrm{e}^{-ik_n((x-x_1)\cos\theta+(y-y_1)\sin\theta)} \,\mathrm{d}x\mathrm{d}y. \tag{6.9}$$

Figure 6.4 shows a high frequency mode shape. Figures 6.5 and 6.7 show the Gaussian weighting function multiplied by the mode shape in figure 6.4 centred at two different positions. This leaves a small patch of the mode shape left. The Fourier transforms around the two points are shown in figures 6.6 and 6.8. The activity is localized around the arc of the circle $k = 47.4931$ as expected. The maximum gives the direction of the rays at that point.

6.5.1 Adaptive ray direction function

It is possible to track the ray directions by using an adaptive process. Starting from a given point the direction with the greatest magnitude can be found. A small step can

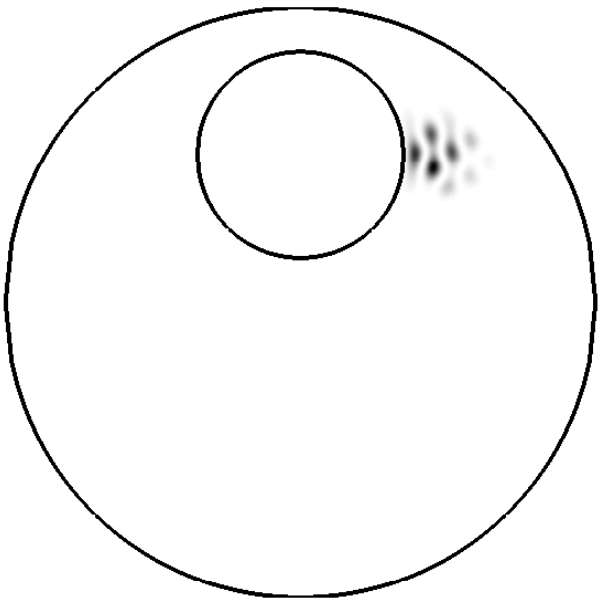

Figure 6.5: Mode shape $k = 47.4931$ multiplied by a Gaussian weighting function.

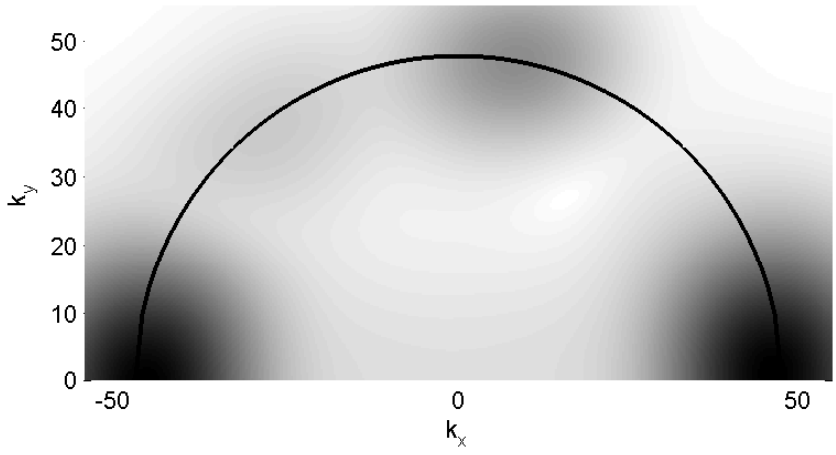

Figure 6.6: Fourier transform of the mode shape with $k = 47.4931$

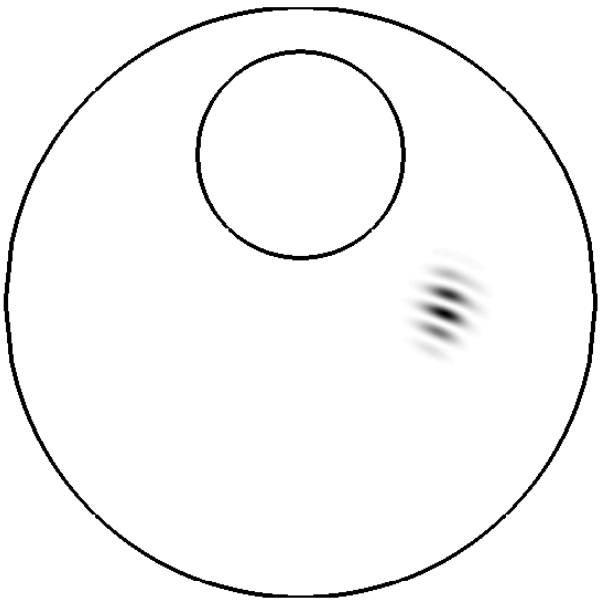

Figure 6.7: Mode shape $k = 47.4931$ multiplied by a Gaussian weighting function.

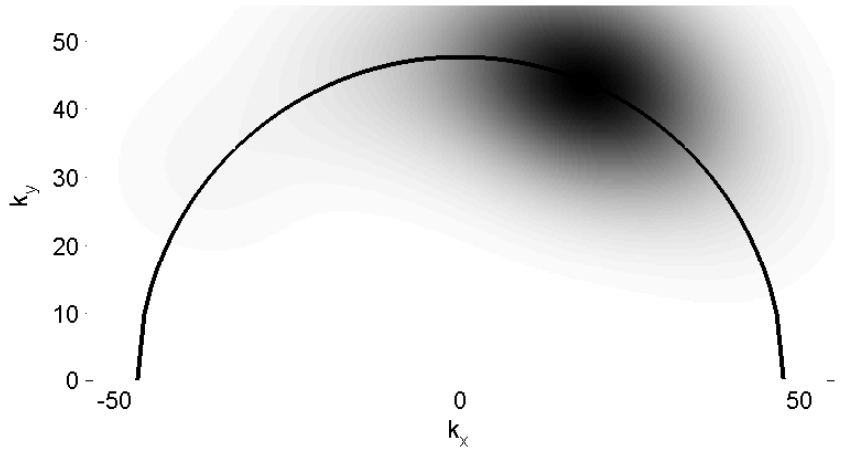

Figure 6.8: Fourier transform of the mode shape with $k = 47.4931$

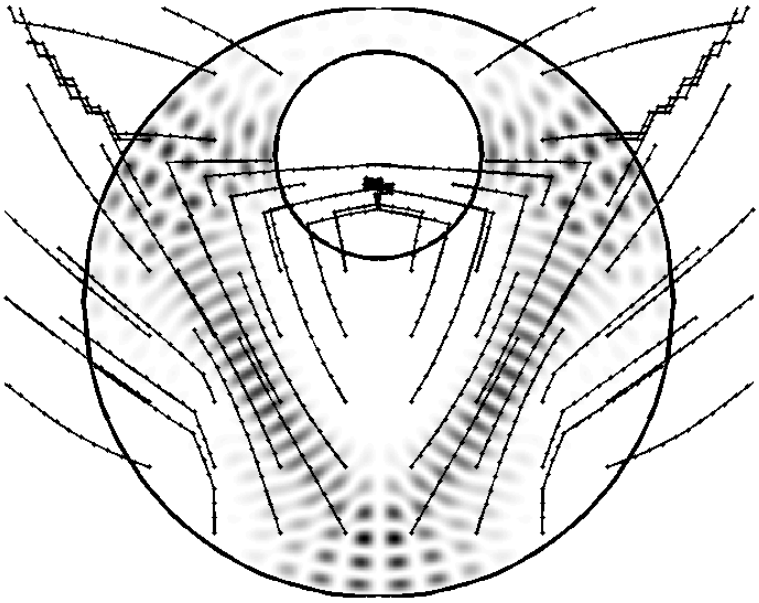

Figure 6.9: Mode shape in the eccentric annulus kR=47.4997. Dots show the points where the ray angle function was calculated. Lines show the path of the adaptive process.

then be taken in this direction and the ray direction found at this new point. In this way the ray paths can be followed.

Figure 6.9 shows the adaptive ray technique used on a mode shape in the eccentric annulus with $kR = 47.4997$. The mode shape is scarred by the Gouesbet orbit 6(2)1. It can be seen that the adaptive paths are curved when they do not follow the periodic orbit. Figure 6.10 shows the adaptive ray technique used on a mode shape in the eccentric annulus with $kR = 47.6054$. This shows a difficulty with the technique. The mode shape here appears to be scarred by a resonance function which displays the first transverse excitation. The ray direction function has not picked this up.

6.5.2 Limitations of the ray direction function

There are two main limitations of the ray direction function. The first is that in can take a considerable time to evaluate the function at all the points of interest. The

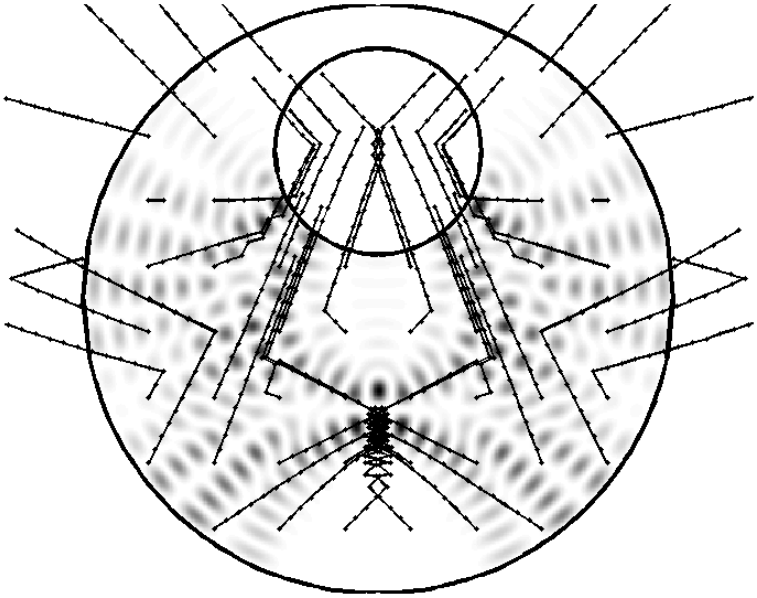

Figure 6.10: Mode shape in the eccentric annulus kR=47.6054. Dots show the points where the ray angle function was calculated. Lines show the path of the adaptive process.

second is that at one particular point there may be several maxima. This information is lost if the adaptive code is used.

6.6 Mode shape decomposition

The Poincaré Husimi function or the ray direction function could be used to find the periodic orbits and thus the resonance functions to decompose the mode shapes. If, however, the periodic orbits are already known for the enclosure a more direct approach may be taken. The resonance functions for all the periodic orbits in the catalogue can be calculated for the wavenumbers of interest. The resonance function with the greatest overlap with the mode shape can then be found and removed. This process can then be repeated any number of times.

This process will also allow the Mode Scar Hypothesis to be tested. All that this hypothesis needs is for one resonance function to be dominant over the rest of the activity of the mode. This would correspond to the overlap of one resonance function with the mode shape being above a certain value. The figure of 50% will be chosen here, since this would mean that more than half of the mode shape had been explained by the resonance function. This figure is arbitrary and could be varied depending on the given application. The Mode Scar Hypothesis can also be restated in a more testable form for this chapter.

Mode Scar Hypothesis:
Mode shapes in a given enclosure contain the scar of one or more short periodic orbits. A scarred mode shape is defined to be one where the overlap of the mode shape is 50% or more with one resonance function.

This process will be tested for twenty eigenvalues between $kR = 46.6$ and 47.6 that have been found for the parameter set used by Gouesbet *et al* [32]. The mode shapes under consideration are those shown in figures 6.11 and 6.12.

The resonance functions are not orthogonal and so the decomposition of a mode shape will not be unique. The Gouesbet catalogue of periodic orbits will be used here since they have already been computed.

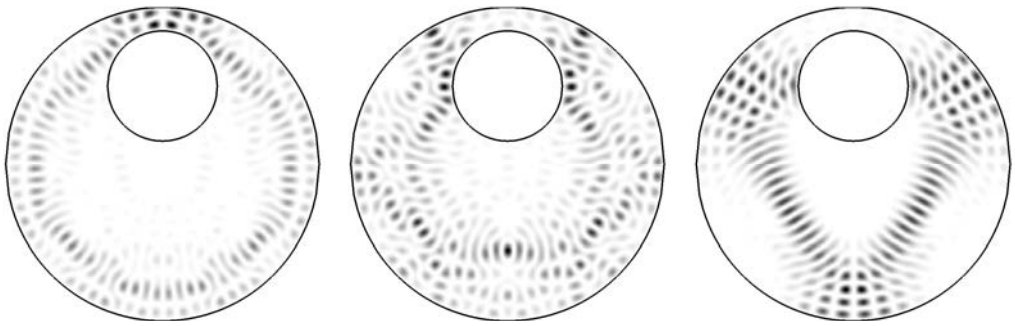

(a) Mode shape 1. (b) Mode shape 2. (c) Mode shape 3.

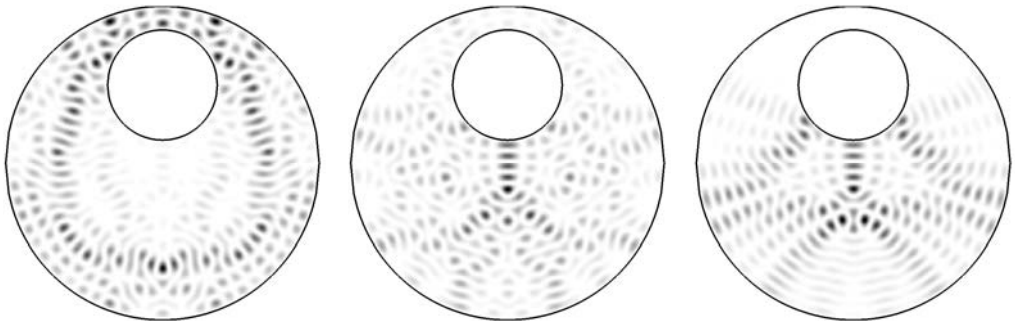

(d) Mode shape 4. (e) Mode shape 5. (f) Mode shape 6.

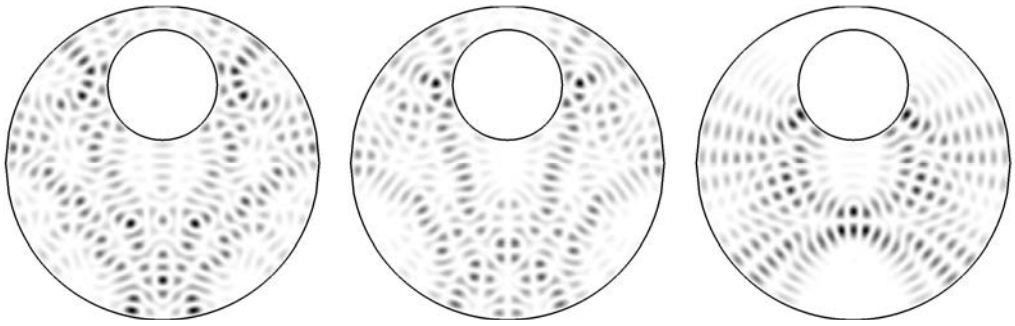

(g) Mode shape 7. (h) Mode shape 8. (i) Mode shape 9.

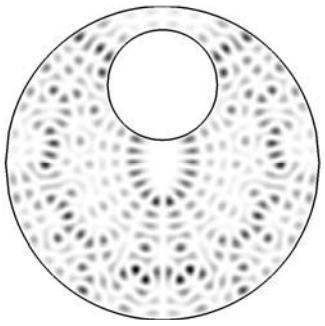

(j) Mode shape 10.

Figure 6.11: Mode shapes under consideration.

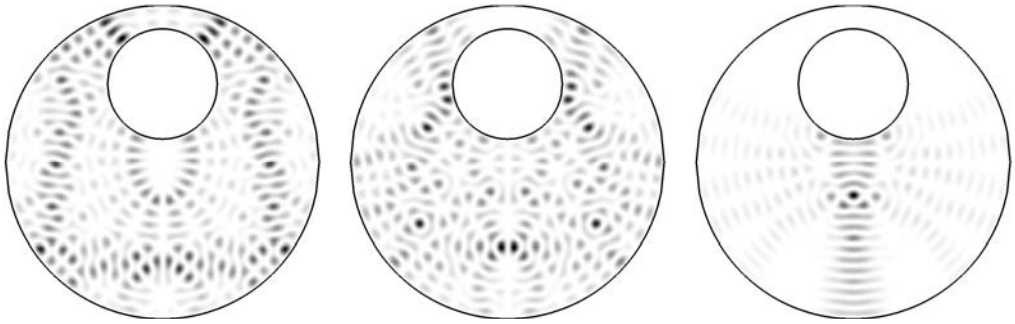

(a) Mode shape 11. (b) Mode shape 12. (c) Mode shape 13.

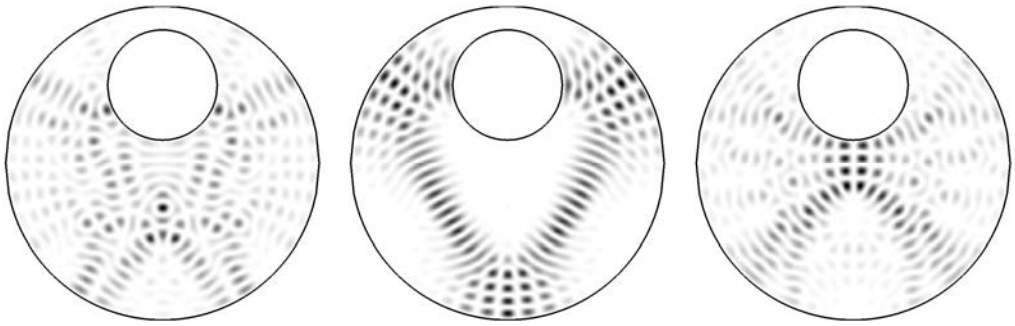

(d) Mode shape 14. (e) Mode shape 15. (f) Mode shape 16.

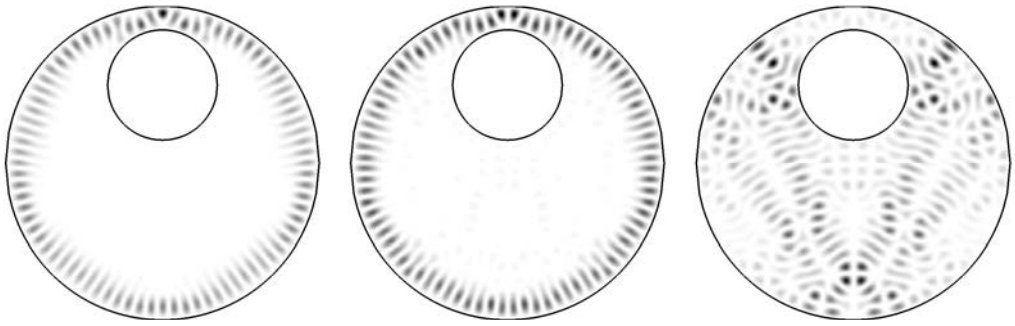

(g) Mode shape 17. (h) Mode shape 18. (i) Mode shape 19.

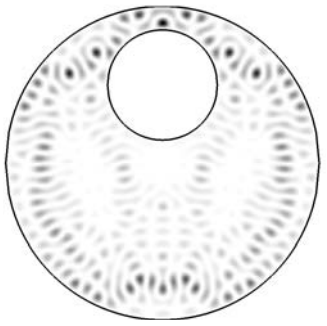

(j) Mode shape 20.

Figure 6.12: Mode shapes under consideration.

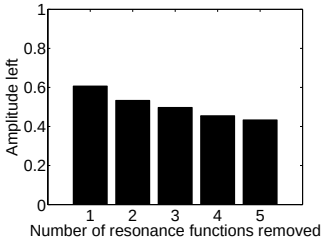

(a) Mode 1 resonance function decomposition.

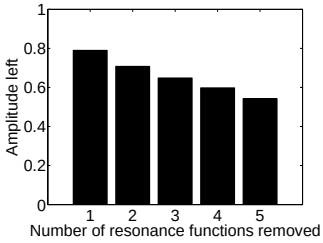

(b) Mode 2 resonance function decomposition.

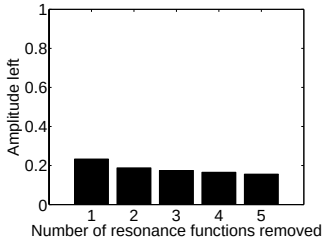

(c) Mode 3 resonance function decomposition.

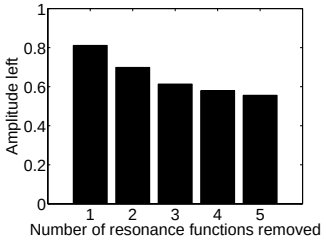

(d) Mode 4 resonance function decomposition.

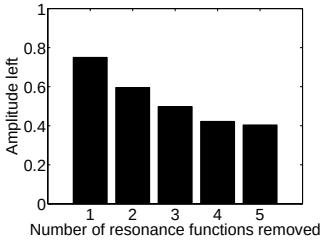

(e) Mode 5 resonance function decomposition.

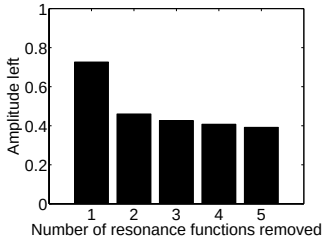

(f) Mode 6 resonance function decomposition.

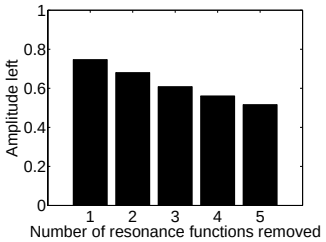

(g) Mode 7 resonance function decomposition.

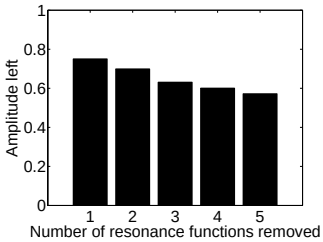

(h) Mode 8 resonance function decomposition.

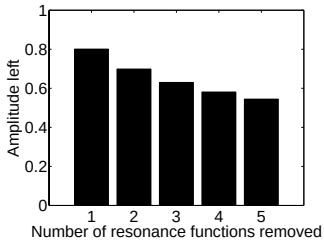

(i) Mode 9 resonance function decomposition.

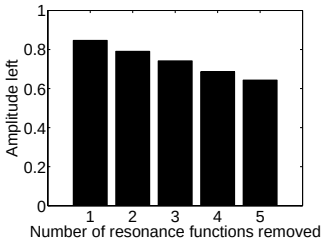

(j) Mode 10 resonance function decomposition.

Figure 6.13: Mode decomposition results.

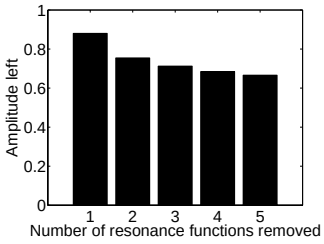

(a) Mode 11 resonance function decomposition.

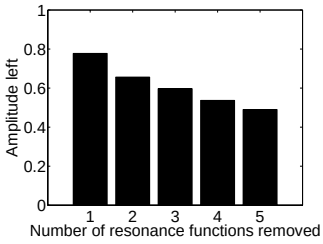

(b) Mode 12 resonance function decomposition.

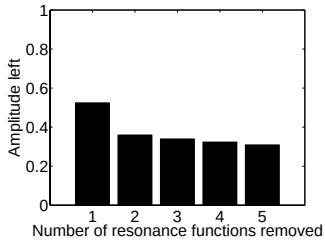

(c) Mode 13 resonance function decomposition.

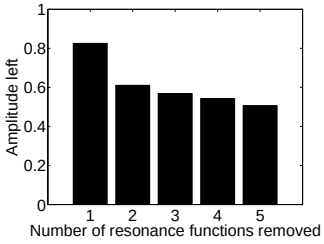

(d) Mode 14 resonance function decomposition.

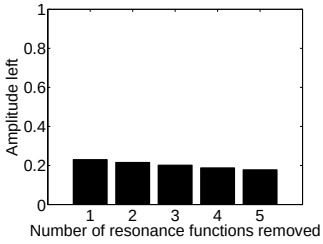

(e) Mode 15 resonance function decomposition.

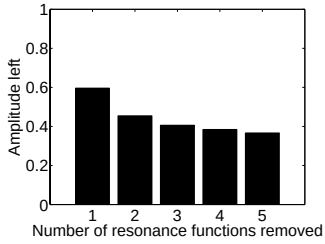

(f) Mode 16 resonance function decomposition.

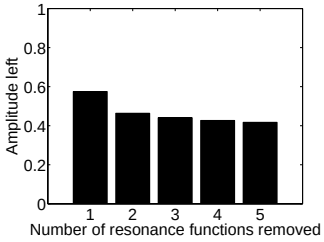

(g) Mode 17 resonance function decomposition.

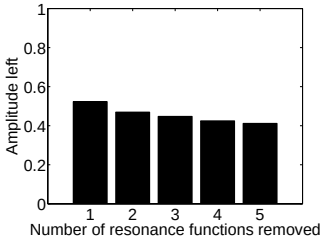

(h) Mode 18 resonance function decomposition.

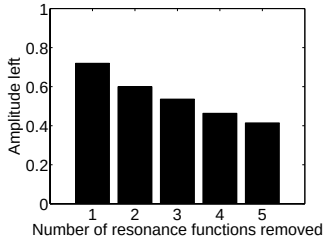

(i) Mode 19 resonance function decomposition.

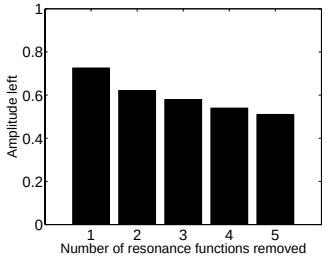

(j) Mode 20 resonance function decomposition.

Figure 6.14: Mode decomposition results.

6.6.1 Mode shape set analysis

Figures 6.13 and 6.14 show the proportion of the amplitude left unexplained after a resonance function has been removed. Some of the mode shapes are almost completely explained by one resonance function while most are not. The mode shapes are one of three types. They are either connected to stable periodic orbits, the integrable part of the ray dynamics or to the unstable periodic orbits.

Integrable orbits

The mode shapes 17 and 18 are connected to the periodic orbits that do not touch the inner boundary. They are related to the mode shapes in the disk enclosure which are integrable. The eccentricity and the radius of the inner disk determine the number of the mode shapes of this type that will exist. If the inner disk boundary touches the outer boundary these orbits will be completely destroyed. The resonance functions associated with the integrable orbits explain most of the activity. Part of the residual here is due to the fact that the resonance function is based on a hexagonal periodic orbit. The residual would be reduced if the resonance function were based on a circle concentric with the outer boundary but of smaller radius.

Marginally stable periodic orbits

The marginally stable periodic orbit 6(2)1 has by far the strongest scars observed here, see mode shapes 3 and 15. This orbit is marginally stable. The mode shape is virtually completely explained by the first resonance function.

Unstable periodic orbits

The majority of the mode shapes are scared by unstable periodic orbits. In particular, the bouncing ball orbit, 1(1)2, scars mode shape 13. The mode shapes which have a strong scar are more fully explained by the resonance function associated with that scar. Some mode shapes contain two scars such as mode shape 6.

The residual for some of the mode shapes is quite large which indicates a failure to explain the mode shape in terms of periodic orbits. There may be several reasons for this. The periodic orbit scarring the mode shape may have more than six bounces against the outer boundary. These periodic orbits may be short but they have not been included in the catalogue. No diffractive periodic orbits are included which may be required. Some residual will exist because the wavenumbers used here may not be sufficiently high to be truly semiclassical.

The residual after five resonance functions have been removed has been used. There will still be contributions from further resonance functions. These contributions will continue to be small though.

6.7 Mode dynamics

The purpose of this chapter is to investigate whether or not periodic orbits can be used to inform the design of an enclosure. Once a periodic orbit has been identified it may need to be removed or kept. Some understanding of how mode shapes change with a shape parameter is required.

The eccentricity of the annulus enclosure will be changed to see how a mode shape changes. SPOT indicates that the mode shapes should be related to the short periodic orbits. Figure 6.15 shows the results of a numerical experiment. The eccentricity of an annulus was changed in steps of 0.001 and at each eccentricity a finite element code determined the mode wavenumbers in a given interval.

The mode wavenumbers in figure 6.15 seem to follow trajectories as the eccentricity changes. These trajectories may be associated with modes scarred by a particular periodic orbit.

The periodic orbit that is associated with a trajectory of mode wavenumbers can be determined by sampling several of the modes along that trajectory. Once the periodic orbit associated with a particular mode has been determined then geometry

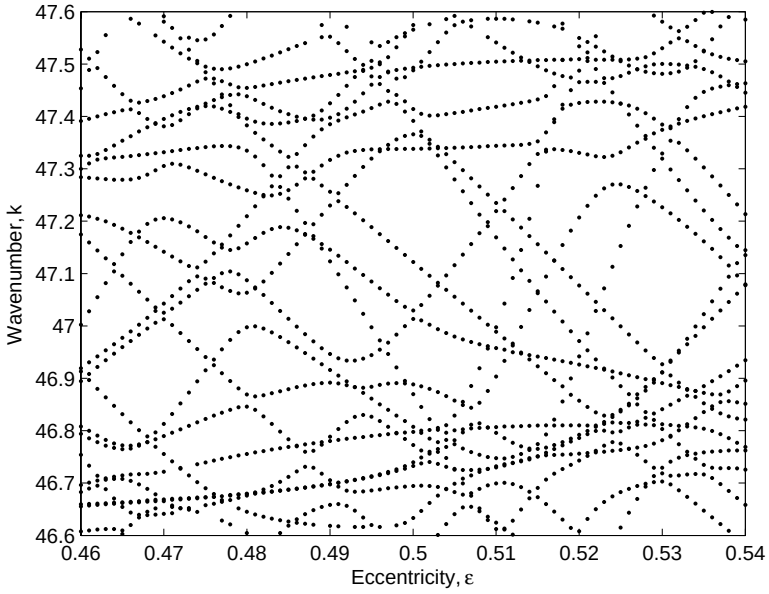

Figure 6.15: 20 mode wavenumbers found as eccentricity increases by 0.001 each step.

will determine how that periodic orbit changes as the eccentricity changes.

Orbit 6(2)1 will be analyzed as an example. The orbit can be calculated for different values of the eccentricity and it exists for quite a wide range of eccentricity values. It is both stable, marginally stable and unstable at different parameter values.

Figure 6.16 shows how the mode wavenumbers change with eccentricity. It shows nine points in bold which are scarred with this orbit. The mode shape and the Husimi plot at each of these points is shown in figure 6.17. It is clear that as the eccentricity changes the mode shapes along this trajectory are still scarred with the same orbit and the Husimi plots provide evidence to support this. It should be noted that as the eccentricity increases beyond 0.50 the scar becomes less important and other activity increases. This is because the orbit has gone from marginally stable at $\varepsilon = 0.5$ to unstable for $\varepsilon > 0.5$.

Figure 6.16 also shows a solid line, which shows how the wavenumber of the resonance function changes with eccentricity. This is calculated using the Bohr–Sommerfeld quantization. This approximation is close to the wavenumbers of the

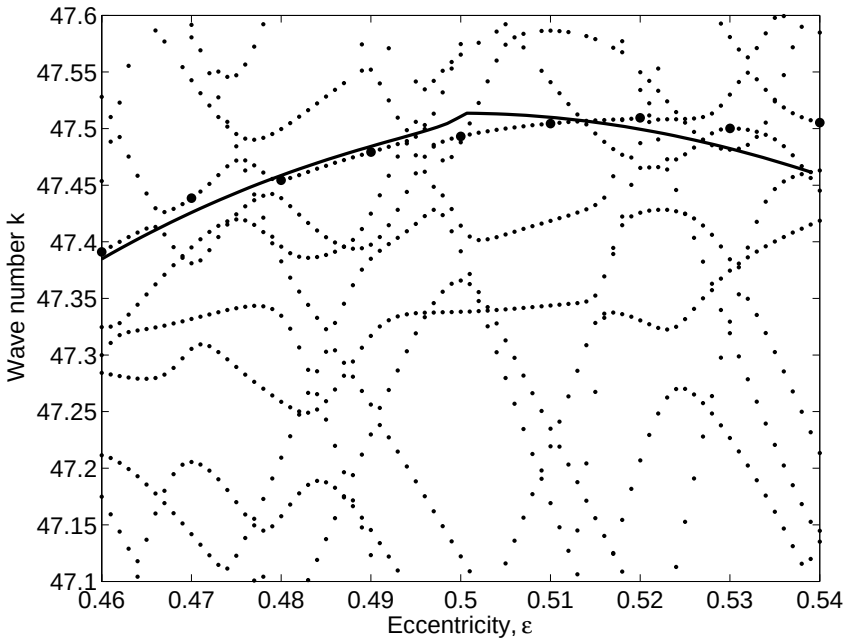

Figure 6.16: Mode wavenumbers found as eccentricity increases by 0.001 each step. The heavy markers denote the points where the mode shapes and Husimi plots in figure 6.17 are taken. This is a blown up version of figure 6.15

actual scarred modes.

6.8 Approximating new mode shapes

Once the new shape of the enclosure has been decided the resonances could be combined using Vergini's formulation and new mode shapes approximated. This may not provide good approximations to the actual final mode shapes. This is because new periodic orbits may have been created, but not necessarily found at that stage of the design loop. The importance of the new periodic orbit may also not be known exactly. This is why it is important that the final objective be validated.

If the problem was at high frequency many periodic orbits would be required to find the SPOT approximation to the mode shape. There may, in fact, be little value in attempting to calculate the SPOT approximation to the mode shape. The understanding of the effect upon the resonance function and thus on the scar may be sufficient.

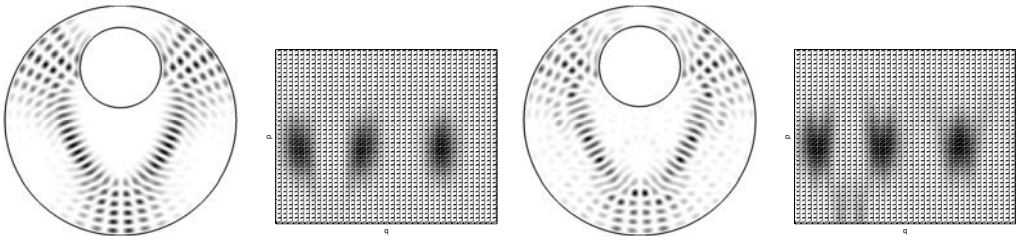

(a) Mode shape $\varepsilon = 0.46$ (b) Husimi function $\varepsilon = 0.46$ (c) Mode shape $\varepsilon = 0.47$ (d) Husimi function $\varepsilon = 0.47$

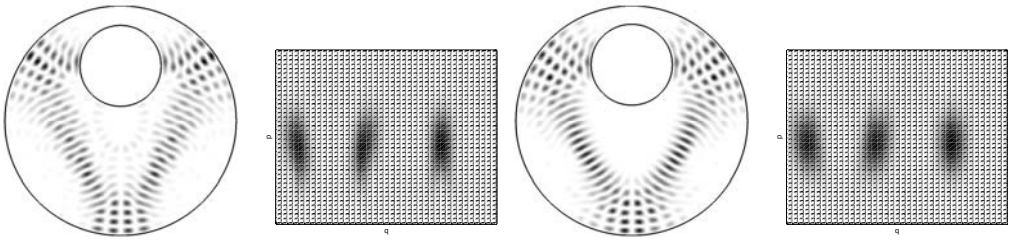

(e) Mode shape $\varepsilon = 0.48$ (f) Husimi function $\varepsilon = 0.48$ (g) Mode shape $\varepsilon = 0.49$ (h) Husimi function $\varepsilon = 0.49$

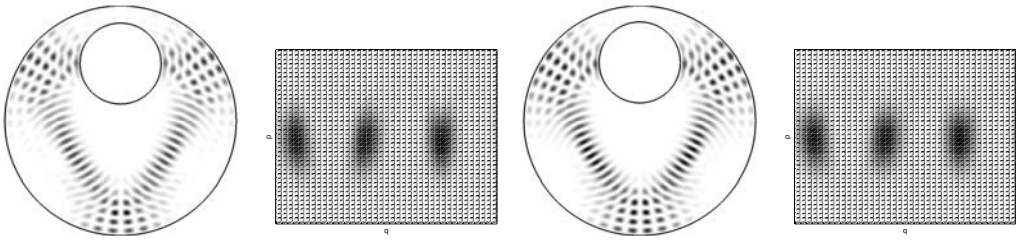

(i) Mode shape $\varepsilon = 0.50$ (j) Husimi function $\varepsilon = 0.50$ (k) Mode shape $\varepsilon = 0.51$ (l) Husimi function $\varepsilon = 0.51$

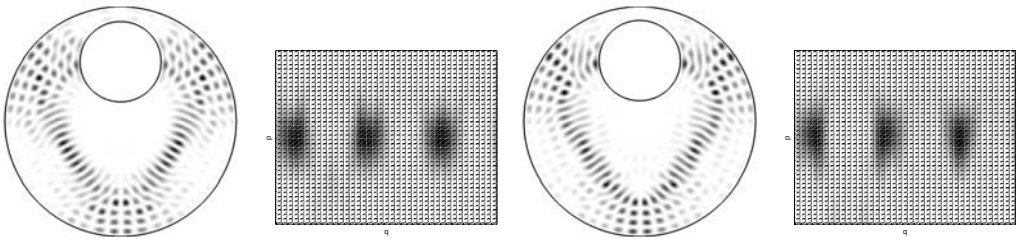

(m) Mode shape $\varepsilon = 0.52$ (n) Husimi function $\varepsilon = 0.52$ (o) Mode shape $\varepsilon = 0.53$ (p) Husimi function $\varepsilon = 0.53$

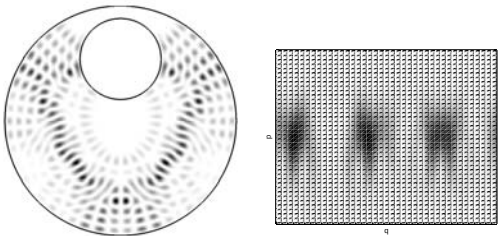

(q) Mode shape $\varepsilon = 0.54$ (r) Husimi function $\varepsilon = 0.54$

Figure 6.17: Mode shape and Husimi function as the eccentricity of the annulus increases. These plots correspond to the bold dots in figure 6.16.

6.9 Validation of output

The final step of the method is to validate that objective has been met. The appropriate mode shapes can be approximated using a numerical package or by a measurement of the real system concerned. The result of this will confirm that the required object of the design loop has been met. If not, the loop can be repeated until the objective is met.

6.10 Conclusions

A design loop for enclosures has been proposed and the steps in the design loop have been examined using a model problem. The Poincaré Husimi function and the Ray Direction function have been proposed as methods to relate mode shapes to periodic orbits. Limitations in these approaches and the fact that a catalogue for the periodic orbits of this eccentric annulus exists means that a more direct approach has been taken to decomposing the mode shapes.

The mode shapes related to marginally stable periodic orbits were very well explained using just one resonance function. The modes related to the integrable part of the ray dynamics were less well explained, but this is due to the lack of continuous symmetry in the resonance function. The other modes shapes which contained unstable periodic orbits had one or two dominant resonance functions, but were less well explained by the short periodic orbits.

Only two modes shapes actually passed the 50% level of overlap with a resonance function so the Mode Scar Hypothesis has not been supported. If the overlap required was lowered to 40% then seven of the 20 modes would have passed. If the overlap required was further reduced to 20% then 17 out of 20 would have passed. This means that the Mode Scar Hypothesis is not supported for this enclosure at these wavenumbers. However, if a larger catalogue of periodic orbits was used then stronger scars may be seen.

SPOT was also used to explain the trajectory of the mode wavenumbers of a mode as the eccentricity of the enclosure was changed.

SPOT may be useful for the design process. The theory is more useful for mode shapes scarred by stable and marginally stable periodic orbits. These orbits are easy to find since they appear in the centre of islands of stability in the Poincaré surface. These periodic orbits have the strongest scars as well. The unstable periodic orbits produce less strong scars and several unstable periodic orbits often appear together meaning their effect is lessened.

Chapter 7

Conclusion

The first chapter introduced the subject and provided some context and motivation for the thesis. The connection between quantum mechanics and acoustics was made. The semiclassical and the high frequency limits were also introduced. The idea of mode shapes scarred by short periodic orbits was also introduced. Finally, an overview of the thesis was given.

Chapter 2 reviewed some important areas of ray mechanics. It gave the foundation of the link between wave mechanics and ray mechanics via the WKBJ approximation. It also showed that wave like properties could be approximated using only ray like quantities. Short periodic orbits and the monodromy matrix were reviewed.

7.1 Annulus trace formula

In chapter 3, a trace formula, which is a sum over periodic orbits, was derived for the concentric annulus enclosure. A more general trace formula for systems with axial symmetry by Creagh and Littlejohn [1] was used for this derivation. This trace formula was used to derive an approximation to the oscillating part of the level density and thus the oscillating part of the mode count for the concentric annulus enclosure. The approximation is valid in the semiclassical limit.

The estimate of the variance of the difference between the true and average mode counts can be used to provide an estimate of the error of the average mode count to the exact mode count for the concentric annulus. The variance of the difference between the true and average mode counts was approximated using the semiclassical trace formula. It was compared to the variance of the difference between the true and average mode counts calculated using the exact eigenvalues and was found to produce a good estimate at high, but finite wavenumbers. The accuracy of the approximation was assessed at small shape ratio and also where periodic orbit families were removed.

Periodic orbits were used to understand the mode count statistics here but this gave no insight into the mode shapes.

7.2 Short periodic orbit theory

A unified presentation of short periodic orbit theory (SPOT) was given in chapter 4. The stability of the periodic orbits is very important in determining the method used for calculating mode shape approximations. The theory for stable periodic orbits was given in Babič and Buldyrev [2] but this was extended to unstable periodic orbits by Vergini [3]. An extension for marginally stable orbits was also given, this has not previously been presented.

The underlying error associated with the approximation was calculated for each type of orbit. This is important for calculating mode shape approximations for unstable periodic orbits. The error for the stable orbits is only $O(1)$ whereas, the error for unstable orbits is $O(k)$, which suggests that the high frequency approximations to modes connected to stable periodic orbits should be much better.

The construction for Neumann and impedance boundary conditions was explicitly calculated. This has not appeared previously in the literature.

Examples of the use of SPOT have been provided. In each case the first 20 mode

shapes have been approximated using only a small number of periodic orbits. The accuracy of the approximations was then assessed against numerical approximations to the mode shapes. The quarter stadium was the first example. The Dirichlet boundary condition case had been calculated by Vergini and Carlo [27] previously. The mode shapes in the quarter stadium with Dirichlet boundary condition on three sides and Neumann boundary condition on the other side were also approximated using SPOT and showed good agreement to the numerically calculated wavenumbers and mode shapes.

The quadrupole enclosure contains stable, unstable and marginally stable periodic orbits, so it has mixed chaoticity. SPOT has not previously been attempted in a shape with mixed chaoticity. The Dirichlet boundary condition results showed good agreement with the wavenumbers and mode shapes of the FEM mode shapes. Only 4 periodic orbits were used to approximate the first 20 mode shapes. The Neumann boundary condition approximations also matched very well to the FEM mode shapes. The impedance boundary condition did not provide such good agreement.

SPOT was attempted in the circle enclosure, which is an integrable domain. The approximation of mode shapes of an integrable domain has not previously been published. The first 20 distinct mode shapes were approximated with good accuracy using only two periodic orbits.

The eccentric annulus also contains stable, unstable and marginally stable periodic orbits. The eccentric annulus has a hole which provides an extra level of difficulty. The first 20 mode shapes were approximated using the only four periodic orbits.

The method works best in convex enclosures with Dirichlet or Neumann boundary conditions and some chaotic ray dynamics. The quarter stadium and quadrupole enclosures both supported the Mode Resonance Function Hypothesis. The circle, which is an integrable domain, did not support the hypothesis but was close to doing so. SPOT did not work so well with impedance boundary conditions. The hypothesis

was not supported by the quadrupole enclosure with impedance boundary conditions. The method did not work well in the eccentric annulus and the hypothesis was not supported here either. This may be due to the lack of diffraction in SPOT.

The method is a semiclassical approximation so some error associated with the approximation will exist.

7.3 Enclosure design

A possible application of SPOT was attempted in chapter 6. A design loop for enclosures was proposed based on SPOT. The steps and calculations required for the design loop were investigated using a model problem, namely the eccentric annulus with Dirichlet boundary conditions.

The first problem is the one of decomposing a mode shape into constituent parts related to short periodic orbits. This is a non-trivial problem. The Poincaré Husimi function and the ray direction function were reviewed. However, a method based on direct comparison of the mode shapes with resonance functions of periodic orbits was used here. The results of this showed that in general modes may be mainly scarred by one or two periodic orbits but that there are contributions from many other orbits. If the mode shape is scarred by a stable periodic orbit however the scar is very much stronger. It is not possible to completely decompose a mode shape down into periodic orbit resonance functions because the resonance functions only relate to a semiclassical approximation.

The Mode Scar Hypothesis in the eccentric annulus was not supported by the results of the decomposition at either the 50%, 40% or 20% levels.

A mode shape was tracked as the shape of the enclosure changed using results from SPOT. This is useful information but new periodic orbits that will affect the mode shapes may be created as the enclosure shape changes. This makes this shape change analysis a complicated procedure. However, the periodic orbits still provide

an understanding of why the mode shapes look as they do.

The final step of the design loop is to validate the proposed changes to the enclosure using the original model or experimental data. This should pick up any new periodic orbits created and their effect on the mode shapes.

7.4 Mode Resonance Function and Mode Scar hypothesis

The results from chapter 5 show that mode shapes can be well approximated by resonance functions of short periodic orbits in certain enclosures. SPOT is a high frequency approximation and so some error is expected. The results support Mode Resonance Function especially when the boundary conditions are Dirichlet or Neumann and the enclosure is convex.

The mode shape decomposition in chapter 6 does seem to provide some evidence that some mode shapes are scarred primarily by one or two resonance functions. This would provide evidence for the for the Mode Scar hypothesis. Overall the hypothesis is not supported in this case though.

7.5 Final Remarks

This thesis has provided theory and examples of how periodic orbits can provide insights into mode wavenumbers and mode shapes. The numerical and analytical techniques usually used to calculate mode shapes and mode wavenumbers do not provide understanding of the link between the geometry of an enclosure and the mode shapes. Periodic orbits in certain cases do provide a link between enclosure geometry and mode shapes.

Chapter 8

Future work

There are two areas where extensions to the work in this thesis could be made. The first would be to waves in thin plates. Bogomolny and Hugues [66] have applied the semiclassical trace formula to thin plates already. It would therefore be natural to extend SPOT to thin plates too.

Secondly, there are many areas of physics where ray paths do not follow straight lines. This generally occurs if the speed of sound changes along the ray path. An example would be sound in the oceans or if the temperature changes in air. SPOT could therefore be extended to curved ray paths.

8.1 Flexural waves in thin plates

The resonance functions for flexural waves in thin plates may be calculated. The governing equation for the thin plate is not the Helmholtz equation but the biharmonic equation.

8.1.1 Governing equations

The theory of flexural waves in thin plates is well known, Graff [67]. The flexural waves are solutions of the biharmonic equation

$$D\nabla^4 w(x,y,t) + \rho h \frac{\partial^2 w(x,y,t)}{\partial t^2} = q(x,y,t). \tag{8.1}$$

The derivation of this equation is given in Graff [67]. In equation (8.1) w is the mode shape function, ρ is the density of the material of the plate, h is the thickness of the plate and q is the force applied per unit area to the plate. The bending stiffness of the plate is given by

$$D = \frac{Eh^3}{12(1-\nu^2)}, \tag{8.2}$$

where E is the Young's modulus and ν is the Poisson ratio of the plate material.

The time dependance of this equation can be removed by separating variables as given in Bogomolny and Hugues [66]. It will be assumed that no force is applied to the plate so that $q = 0$. It is assumed that $w(x,y,t) = W(x,y)T(t)$ which yields the equation

$$\nabla^2 W(x,y) - k^4 W(x,y) = 0, \tag{8.3}$$

where $k^4 = (12\rho(1-\nu)/(Eh^2))\omega^2$. This equation can be factorized to become

$$(\nabla - k^2)(\nabla + k^2)W(x,y) = 0. \tag{8.4}$$

This form of the equation further shows that solutions to this equation can be written as $W(x,y) = W_1(x,y) + W_2(x,y)$ where

$$(\nabla + k^2)W_1(x,y) = 0, \tag{8.5}$$

$$(\nabla - k^2)W_2(x,y) = 0. \tag{8.6}$$

The equation for W_1 is just the Helmholtz equation while the equation for W_2 has ex-

ponentially decaying solutions. The SPOT construction can be performed on W_1, but a semiclassical approximation to W_2 may be required too. The boundary conditions must be understood for the SPOT approximation.

8.1.2 Boundary conditions

There are three different common sets of boundary conditions for flexural waves in the plate as given in Graff [67] and Bogomolny and Hugues [66]. The plate edge can be clamped, simply supported or left free to vibrate. The governing equation is fourth-order so two boundary conditions are required. The boundary conditions will be given in coordinates tangential and normal to the boundary of the domain at the bounce point. The reflection coefficient at the bounce point will be required for each of the following boundary conditions. This can be calculated directly by using the construction.

Clamped edge

The clamped edge boundary conditions are

$$W = 0, \tag{8.7}$$

$$\frac{\partial W}{\partial n} = 0. \tag{8.8}$$

Supported edge

The supported edge boundary conditions are

$$W = 0, \tag{8.9}$$

$$\frac{\partial^2 W}{\partial n^2} + \nu \frac{\partial^2 W}{\partial l^2} - \nu K \frac{\partial W}{\partial n} = 0. \tag{8.10}$$

Free edge

The free edge boundary conditions are

$$\frac{\partial^3 W}{\partial n^3} + (2-\nu)\left(\frac{\partial^3 W}{\partial l^2 \partial n} + \frac{\mathrm{d}K}{\mathrm{d}l}\right) + 3K\frac{\partial^2 W}{\partial l^2} - (1+\nu)K^2\frac{\partial W}{\partial n} = 0, \quad (8.11)$$

$$\frac{\partial^2 W}{\partial n^2} + \nu\frac{\partial^2 W}{\partial l^2} - \nu K\frac{\partial W}{\partial n} = 0. \quad (8.12)$$

It can be clearly seen that these expressions are complicated. If the SPOT resonance function is just completed for W_1 as it is tempting to do then one boundary condition will effectively become redundant. This is because the equation for W_1 is only a second-order equation and as such would only require one boundary condition. In effect this would reduce the thin plate problem to the Helmholtz equation with a boundary condition.

There may well be problems with the construction in the thin plate because of the extra approximations made. It is difficult to fully quantify the effect on the accuracy of the mode shape approximations.

8.2 Curved ray paths

There are many circumstances where ray paths in an enclosure are curved, for example in a duct with a temperature gradient across the cross-section. A number of modifications would have to be made to SPOT as presented here. The periodic orbits would have to be found but this process may be harder. It would certainly be harder to find orbits by inspection for example. The monodromy matrices for the periodic orbits would have to be calculated. Some work has been done on billiards with non-Euclidean geometry for example [4, 13, 68] which may be of use for this problem.

The construction for curved ray paths would be a non-trivial exercise but may be useful for a number of real-world applications.

Appendix A

Finite element method

The finite element method (FEM) has been used to provide numerical approximations for mode shapes where no analytical expression exists. The method is very well known, for example [69]. A brief overview of the method will be given. An investigation of the convergence at the wavenumbers used will be completed.

A.1 Method set up

A.1.1 Mesh

The domain under consideration is first meshed or discretized. In two dimensions this amounts to cutting the domain into triangles. There are rules for how this process should be completed, for example the vertex of a triangle can only meet another triangle at its vertex. An example of a mesh in a disk domain is shown in figure A.1.

The general rule is that there should be at least 10 elements per wavelength. The number of elements required to find the modes in this thesis will be investigated in section A.2.

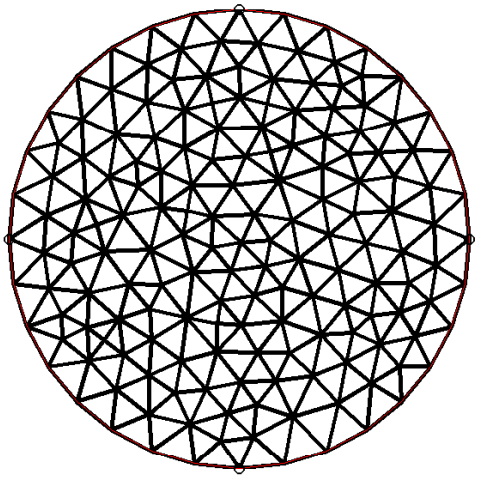

Figure A.1: A meshed disk with radius 1. The maximum element side length is 0.2.

A.1.2 Finite elements

The approximation over each element can be linear but in this thesis quadratic elements have been chosen. These provide greater accuracy but require more degrees of freedom.

The equations are discretized using basis functions on the mesh. This results in a matrix equation which is solved to produce the final numerical approximation.

A.2 Convergence

A.2.1 Low frequency convergence

The finite element method is used in this thesis to find eigenmodes at various wavenumbers. In chapter 5 the highest wavenumber is around $kR = 12$. The maximum element size required for the finite element method to be accurate needs to be found. This will be investigated by using FEM to find the mode wavenumber in a shape where an analytic expression exists for the mode wavenumber.

The mode with wavenumber 11.0647 in a disk enclosure will be used. The mode

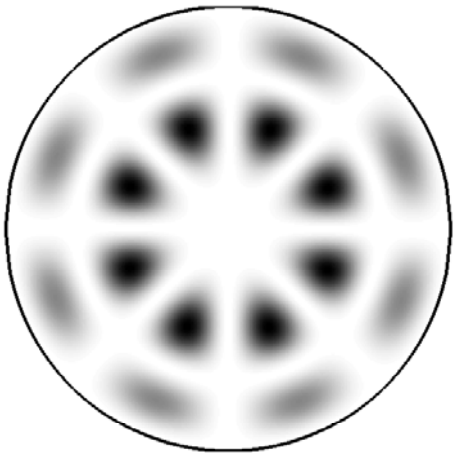

Figure A.2: Mode shape in the disk with wavenumber 11.0647.

that is being computed is plotted in figure A.2. This mode has been numerically approximated with FEM with several different mesh sizes. The results have been plotted in figure A.3. As the maximum element size falls the mode wavenumber approaches the analytic value.

The time taken to compute the mode increases as the element size drops.

A.2.2 High frequency convergence

In chapter 6 the wavenumber under consideration is around 48. This requires a finer mesh to get the required accuracy. A mode in the disk enclosure with wavenumber 47.0487 will be used for the high frequency convergence test. The maximum element size must start at a much lower level otherwise the mode shape will not be found. The mode shape under consideration is plotted in figure A.5.

A much finer mesh is required before the finite element mode converges to the analytic value of the mode wavenumber. Figure A.6 shows the convergence as the maximum element size falls.

The convergence can also be seen as the number of degrees of freedom increases, see figure A.7.

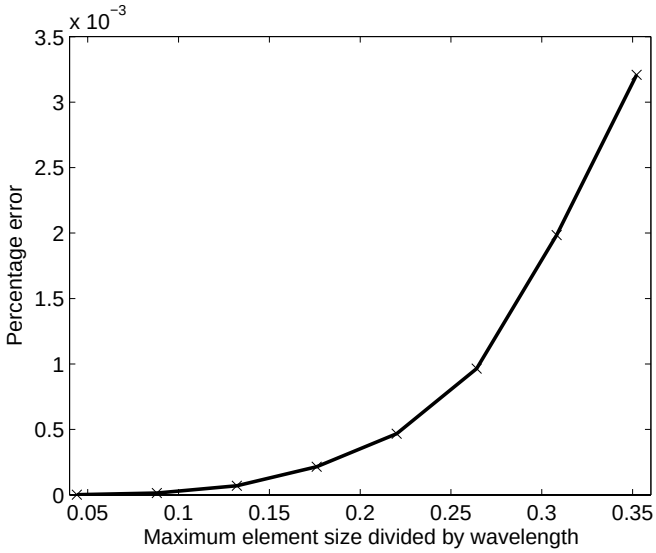

Figure A.3: Convergence of the finite element method to the analytic value of the mode wavenumber. '×' show data points. '...' is the analytic mode wavenumber.

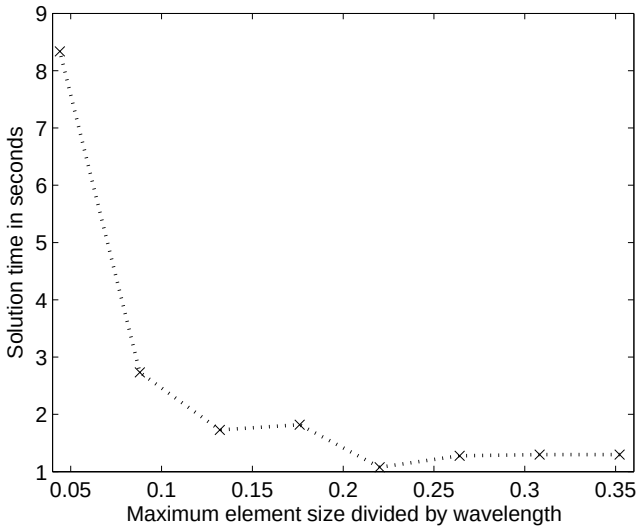

Figure A.4: Time taken in seconds to find the mode.

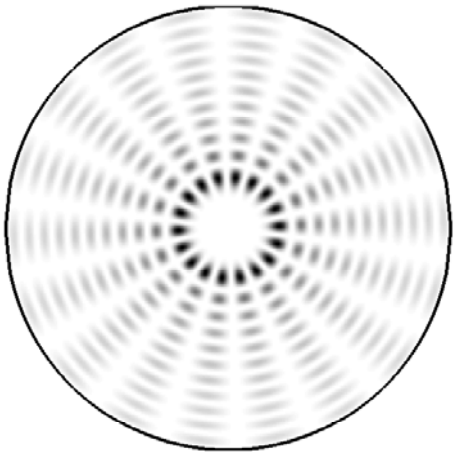

Figure A.5: High frequency mode shape, $kR = 47.0487$.

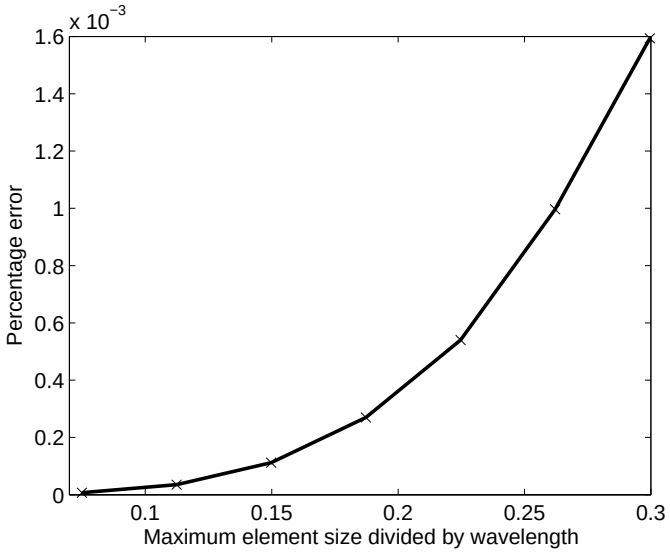

Figure A.6: Convergence of the finite element method to the analytic value of the mode wavenumber. '$\times$' show data points. '...' is the analytic mode wavenumber.

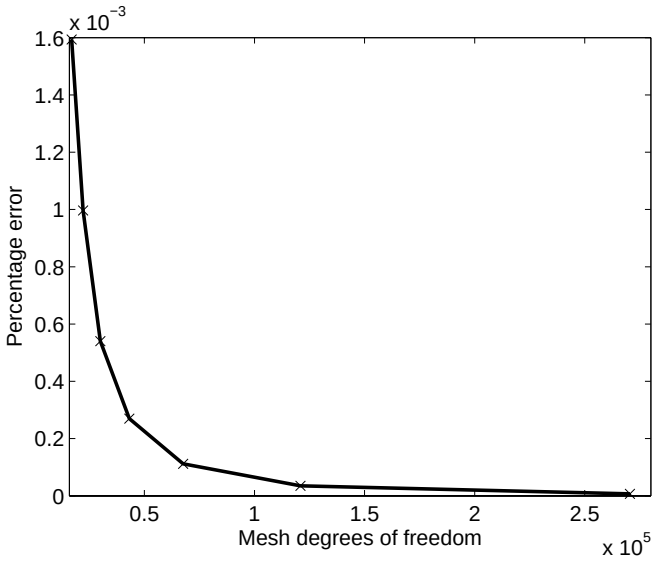

Figure A.7: Convergence of the finite element method to the analytic value of the mode wavenumber. '×' show data points. '...' is the analytic mode wavenumber.

A.3 Conclusion

The maximum element size used for low frequency work should be less than 0.03 and 0.015 or less for high frequency work.

Bibliography

[1] S. C. Creagh and R. G. Littlejohn. Semiclassical trace formulas in the presence of continuous symmetries. *Physical Review A*, 44(2):836, July 1991.

[2] V. M. Babič and V. S. Buldyrev. *Short-Wavelength Diffraction Theory*. Springer Berlin, 1991.

[3] E. G. Vergini. Semiclassical theory of short periodic orbits in quantum chaos. *Journal of Physics A: Mathematics and General*, 33:4709–4716, 2000.

[4] M. C. Gutzwiller. *Chaos in Classical and Quantum Mechanics*. Springer-Verlag, 1990.

[5] P. Glendinning. *Stability, instability and chaos: an introduction to the theory of nonlinear differential equations*. Cambridge texts in applied mathematics. Cambridge University Press, 1994.

[6] A. L. Abul-Magd, B. Dietz, T Friedrich, and A Richter. Spectral fluctuations of billiards with mixed dynamics: From time series to superstatistics. *Physical Review E*, 77:046202, 2008.

[7] B. Dietz, B. Mossner, T. Papenbrock, U. Reif, and A. Richter. Bouncing ball orbits and symmetry breaking effects in a three-dimensional chaotic billiard. *Physical Review E*, 77:046221, 2008.

[8] J. Kuipers and M Sieber. Semiclassical relation between open trajectories and periodic orbits for the wigner time delay. *Physical Review E*, 77:046219, 2008.

[9] D. Wisniacki and G. G. Carlo. Scarring in open quantum systems. *Physical Review E*, 77:045201(R), 2008.

[10] E. G. Vergini and M. Saraceno. Calculation by scaling of highly excited states of billiards. *Physical Review E*, 52(3):2204, September 1995.

[11] A. Barnett. *Dissipation In Deforming Chaotic Billiards*. PhD thesis, Harvard University, 2000.

[12] M. V. Berry. The bakerian lecture: Quantum chaology. *Proc. R. Soc. Lond. A*, 413:183–198, 1987.

[13] H-J. Stockmann. *Quantum Chaos: An Introduction*. Cambridge University Press, 1999.

[14] J Ockendon, S Howison, A Lacy, and A Movchan. *Applied Partial Differential equations*. OUP, 1999.

[15] J. B. Keller. Semiclassical mechanics. *SIAM Review*, 27(4):485–504, December 1985.

[16] J. B. Keller and S. I. Rubinow. Asymptotic solution of eigenvalue problems. *Ann. Phys.-New York*, 9:24–75, 1960.

[17] H. P. Baltes and E. R. Hilf. *Spectra of finite systems*. B-I Wissenschaftsverlag, Mannheim, 1976.

[18] M. Brack and R. K. Bhaduri. *Semiclassical Physics*. Addison Wesley, 1997.

[19] R. Balian and C. Bloch. Distribution of eigenfrequencies for the wave wquation in a finite domain iii. eigenfrequency density oscillations. *Annals of Physics*, 69:76–160, 1972.

[20] M. V. Berry and M. Tabor. Closed orbits and the regular bound spectrum. *Proc. R. Soc. Lond. A*, 349:101–123, 1976.

[21] A. I. Shnirelman. *KAM theory and semiclassical approximations to eigenfunctions*, chapter On the asymptotic properties of eigenfunctions in the regions of chaotic motion (Addendum). Springer-Verlag, 1993.

[22] M. V. Berry. Regular and irregular semiclassical wavefunctions. *Journal of Physics A: Mathematics and General*, 10(12):2083–2091, 1977.

[23] M. V. Berry. *Chaotic behaviour of deterministic systems*, chapter Course 3: Semiclassical mechanics of regular and irregular motion, pages 172–271. Les Houches XXXVI 1981. North-Holland, 1983.

[24] E. J. Heller. *Les Houches LII, 1989: Chaos and Quantum Physics*, chapter Course 9, pages 547–663. Elsevier Science Publishers BV, 1991.

[25] S W McDonald and A N Kaufman. To be found. *Physics Review Letters*, 42: 1189, 1979.

[26] E. J. Heller. Bound-state eigenfunctions of classically chaotic hamiltonian systems: Scars of periodic orbits. *Physical Review Letters*, 53(16):1515, October 1984.

[27] E. G. Vergini and G. G. Carlo. Semiclassical quantization with short periodic orbits. *Journal of Physics A: Mathematics and General*, 33:4717–4724, 2000.

[28] V. M. Babich. Eigenfunctions concentrated near a closed geodesic. Seminars in mathematics- V A Steklov Institute Leningrad Volume 9, 1968. Translated by Consultants Bureau New York 1970.

[29] V. M. Babich and V. F. Lazutkin. Eigenfunctions concentrated near a closed geodesic. *Topics in Mathematical Physics*, 2:9–18, 1968. Translated by Consultants Bureau New York 1968.

[30] H. E. Tureci, H. G. L. Schwefel, A. Douglas Stone, and E. E. Narimanov. Gaussian-optical approach to stable periodic orbit resonances of partially chaotic dielectric micro-cavities. *Optics Express*, 10(16):752–776, 2002.

[31] K. Richter. *Semiclassical theory of Mesoscopic Quantum Systems*. Springer, Berlin., 2000.

[32] G. Gouesbet, S. Meunier-Guttin-Cluzel, and G. Grehan. Periodic orbits in hamiltonian chaos of the annular billiard. *Physical Review E*, 65:016212, 2001.

[33] K. T. Hansen. Alternative method to find orbits in chaotic systems. *Physical Review E*, 52(3):2388–2391, September 1995.

[34] M. C. M. Wright and C. J. Ham. Periodic orbit theory in acoustics: spectral fluctuations in circlar and annular wave guides. *Journal of the Acoustical Society of America*, 121(4), 2007.

[35] S. J. Chapman. On the approximation of the eigenvalues of an annulus using complex rays. *Eur. J. Appl. Math.*, 10:225–236, 1999.

[36] K. Richter, D. Ullmo, and R. A. Jalabert. Orbital magnetism in the ballistic regime: Geometric effects. *Phys. Rep.*, 276:1–83, 1996.

[37] F. D. Mazzitelli, M. J. Sanchez, N. N. Scoccola, and J. von Stecher. Casimir interaction between two concentric cylinders: Exact versus semiclassical results. *Phys. Rev. A*, 67:013807, 2003.

[38] M. V. Berry and M. Tabor. Calculating the bound spectrum by path summation in action-angle variables. *J. Phys. A-Math. Gen.*, 10:371–379, 1977.

[39] N. C. Snaith and D. A. Goodings. Semiclassical approximations to diffractive effects in the annulus billiard. *Phys. Rev. E*, 55(5):5212, May 1997.

[40] E. B. Bogomolny. Semiclassical quantization of multidimensional systems. *Nonlinearity*, 5:805, 1992.

[41] H. P. W. Gottlieb. On pinned and collared membranes. *Journal of Sound and Vibration*, 225(5):1000–1004, 1999.

[42] R. W. Robinett. Energy eigenvalues and periodic orbits for the circular disk or annular infinite well. *Surface Review and Letters*, 5(2):519–526, 1998.

[43] R. W. Robinett. Periodic orbit theory analysis of the circular disk or annular billiard: Nonclassical effects and the distribution of energy eigenvalues. *Am. J. Phys.*, 67(1):67, January 1999.

[44] P. Seba. Wave chaos in singular quantum billiard. *Physical Review Letters*, 64 (16):1855–1858, April 1990.

[45] P. Rosenqvist, N.D. Whelan, and A. Wirzba. Small disks and semiclassical resonances. *Journal of Physics A: Mathematics and General*, 29:5441–5453, 1996.

[46] E. G. Vergini and G. G. Carlo. Semiclassical construction of resonances with hyperbolic structure: the scar function. *Journal of Physics A: Mathematics and General*, 34:4525, 2001.

[47] G. G. Carlo, E. G. Vergini, and P. Lustemberg. Scar functions in the bunimovich stadium billiard. *Journal of Physics A: Mathematics and General*, 35:7965–7982, 2002.

[48] P C W Davies and D S Betts. *Quantum Mechanics*. Nelson Thornes Ltd, 2nd edition edition, 2002. ISBN 0 7487 4446 0.

[49] K Hannabuss. *An introduction to quantum theory*. Oxford University Press, 1997.

[50] E. G. Vergini and D. Schneider. Asymptotic behaviour of matrix elements between scar functions. *Journal of Physics A: Mathematics and General*, 38: 587, 2005.

[51] E. G. Vergini. Semiclassical limit of chaotic eigenfunctions. *Journal of Physics A: Mathematics and General*, 37:6507–6519, 2004.

[52] D. A. Wisniacki, F. Borondo, E. G. Vergini, and R. M. Benito. Beyond the first recurrence in scar phenomena. *Physical Review E*, 62(6), 2000.

[53] E G Vergini. Unpublished correspondance.

[54] A D Pierce. *Acoustics: An introduction to its physical principles and applications*. Acoustical Society of America, 1991.

[55] L. Bunimovich. On ergodic prpoperties of nowhere dispersing billiards. *Communications in mathematical physics*, 65(3):295–312, 1979.

[56] D J Ewins. *Modal Testing: Theory, practice and application*. Research Studies Press Ltd, 2nd edition edition, 2000. ISBN 0 86380 218 4.

[57] G. Tanner. How chaotic is the stadium billiard? a semiclassical analysis. *Journal of Physics A: Mathematical and General*, 30(8):2863–2888, 1997.

[58] H Feshbach P M Morse. *Methods of Theoretical Physics*, volume 2. McGraw-Hill Book Company, 1953. Chapter 9.

[59] H-W Lee. Theory and application of the quantum phase-space distribution functions. *Physics Reports*, 259:147–211, 1995.

[60] E Wigner. On the quantum correction for thermodynamic equilibrium. *Physics Review*, 40:749, 1932.

[61] K Husimi. Some formal properties of the density matrix. *Proceedings of the Physico-Mathematical Society of Japan*, 22:264, 1940.

[62] L E Reichl. *The transition to chaos: Conservative classical systems and quantum manifestations*. Springer, 2nd edition edition, 2004.

[63] R Schubert A. Backer, S Furstberger. Poincare husimi representation of eigenstates in quantum billiards. *Physical Review E*, 70(3), 2004.

[64] R Schubert M Hentschel, H Schomerus. Husimi functions at dielectric interfaces: Inside-outside duality for optical systems and beyond. *Europhysics Letters*, 62(5):636–642, 2003.

[65] M C M Wright. Unpublished correspondance.

[66] E Bogomolny and E Hugues. Semiclassical theory of vibrations of plates. *Physical Review E*, 57(5):5404–5424, 1998.

[67] K F Graff. *Wave motion in elastic solids*. Dover Publications, New York, 1991.

[68] N. L. Balazs and A. Voros. Chaos in the pseudosphere. *Physics Reports*, 143: 109–240, November 1986.

[69] M Petyt. *Introduction to finite element vibration analysis*. Cambridge University Press, 1990.